Low gain avalanche diodes for timing applications

TECHNISCHE
UNIVERSITÄT
DARMSTADT

Fachbereich Physik

Institut für Kernphysik

AG Galatyuk (ViP-QM)

Low gain avalanche diodes for timing applications

Accepted doctoral thesis by Vadym Kedych, M.Sc.

Date of submission: 13.05.2024
Date of thesis defense: 08.07.2024

Darmstadt - D 17

Erklärungen laut Promotionsordnung

§ 8 Abs. 1 lit. d PromO

Ich versichere hiermit, dass zu einem vorherigen Zeitpunkt noch keine Promotion versucht wurde. In diesem Fall sind nähere Angaben über Zeitpunkt, Hochschule, Dissertationsthema und Ergebnis dieses Versuchs mitzuteilen.

§ 9 Abs. 1 PromO

Ich versichere hiermit, dass die vorliegende Dissertation – abgesehen von den in ihr ausdrücklich genannten Hilfen – selbstständig verfasst wurde und dass die „Grundsätze zur Sicherung guter wissenschaftlicher Praxis an der Technischen Universität Darmstadt" und die „Leitlinien zum Umgang mit digitalen Forschungsdaten an der TU Darmstadt" in den jeweils aktuellen Versionen bei der Verfassung der Dissertation beachtet wurden.

§ 9 Abs. 2 PromO

Die Arbeit hat bisher noch nicht zu Prüfungszwecken gedient.

Darmstadt, 13.05.2024

_____

V. Kedych

Contents

Abstract

This work aims to develop a non-destructive beam time structure monitoring system for the superconducting Darmstadt linear accelerator (S-DALINAC). The S-DALINAC is a $3\,$GHz superconducting electron accelerator capable of operations in the energy recovery (ERL) mode. The ERL operation mode allows the recovery of the beam energy and uses it for an acceleration of consecutive bunches. It is reached by recirculating the beam to the main LINAC with a $180°$ phase shift with respect to the phase of the electric field in the accelerator cavities. During the operation in the ERL mode, one beamline recirculates two beams simultaneously, leading to the $6\,$GHz repetition rate inside this beamline. To monitor both beams, a detector system capable of resolving this time structure of $6\,$GHz has to be built.

For this purpose, a test setup based on the Low Gain Avalanche Diodes (LGADs), silicon sensors designed for high-precision simultaneous position and time measurement, was developed. Several groups have demonstrated a time resolution below $50\,$ps for LGADs, which indicates that this technology is a suitable candidate for the beam time structure monitoring at the S-DALINAC. The read-out system was based on leading-edge discriminators and Field-Programmable Gate Array (FPGA) based Time-to-Digital converters (TDCs) developed at GSI in Darmstadt, Germany. These allow for the estimation of arrival time and signal width via the time-over-threshold method.

To demonstrate the feasibility of an LGAD-based beam time structure monitoring system, a simplified setup based on a single $1\,$cm$\times0.5\,$cm LGAD sensor with a limited number of active channels was prepared and tested at the experimental hall at the S-DALINAC. Due to the placement of the setup, the delivered beam had a $3\,$GHz time structure. During this proof-of-principle demonstration, the S-DALINAC $3\,$GHz beam time structure was successfully resolved for the first time.

An upgraded setup, which employed two $1\,$cm$\times1\,$cm LGAD sensors, was prepared to investigate the feasibility and performance of an LGAD-based beam time structure monitoring system. In contrast to the first proof-of-principle experiment, the entire system was read out using an upgraded version of the read-out system. Also, with this upgraded setup, the $3\,$GHz time structure was successfully resolved, and an intrinsic time resolution of $79\,$ps was demonstrated.

Since the setup installation for the proof-of-concept study had to be done outside of the accelerator hall, only the beam with the $3\,$GHz time structure could be measured. A design concept study using Geant4 simulations was performed as a next step to investigate the feasibility of an LGAD-based beam time structure monitoring system for the ERL mode. To evaluate the LGAD's performance in such conditions, a simulation with the simplified geometry of the potential measurement station was prepared. This simulation demonstrated the feasibility of an LGAD-based system for monitoring the $6\,$GHz beam time structure. Additionally, the best detector position inside the accelerator hall could be identified. In the upcoming runs at the S-DALINAC, it will be possible to verify the results of simulations and the concept.

Lastly, the feasibility of the machine learning (ML) approach for the LGADs data analysis was demonstrated. It was shown that the ML approach reduces the amount of data required for the LGAD correction without distorting the time resolution. Additionally, this approach can be used to implement an online LGAD correction procedure.

Zusammenfassung

Diese Arbeit zielt darauf ab, ein zerstörungsfreies Strahl-Zeitstruktur Überwachungssystem für den supraleitenden Linearbeschleuniger Darmstadt S-DALINAC zu entwickeln. Der S-DALINAC ist ein $3\,\mathrm{GHz}$ supraleitender Elektronenbeschleuniger, der als energierückgewinnender Linearbeschleuniger (Energy recovery LINAC, ERL) betrieben werden kann. Der ERL-Betriebsmodus ermöglicht die Rückgewinnung der Strahlenergie und deren Nutzung zur Beschleunigung folgender Teilchenpakete. Dies wird erreicht, indem der Strahl mit einer Phasenverschiebung von $180°$, bezüglich der Phase des elektrischen Feldes in den Beschleunigerhohlräumen, zum Hauptbeschleuniger zurückgeführt wird. Während des Betriebs im ERL-Modus zirkulieren zwei Strahlen gleichzeitig in einer Strahllinie, was zu einer Teilchenpaket-Rate von $6\,\mathrm{GHz}$ innerhalb dieser Strahllinie führt. Um beide Strahlen zu überwachen, muss ein Detektorsystem aufgebaut werden, das diese Zeitstruktur von $6\,\mathrm{GHz}$ auflösen kann.

Zu diesem Zweck wurde ein Testaufbau auf Grundlage von Low Gain Avalanche Diodes (LGADs) entwickelt. LGADs sind für die gleichzeitige und hochpräzise Messung von Position und Zeit optimierte Siliziumsensoren. Mehrere Gruppen haben für LGADs eine Zeitauflösung von unter $50\,\mathrm{ps}$ nachgewiesen, was darauf hindeutet, dass diese Technologie ein geeigneter Kandidat für die Überwachung der Strahl-Zeitstruktur am S-DALINAC ist. Das Auslesesystem basiert auf Leading-Edge-Diskriminatoren und Field-Programmable Gate Array (FPGA)-basierten Time-to-Digital converters (TDCs), die an der GSI in Darmstadt entwickelt wurden. Diese ermöglichen die Messung der Ankunftszeit und der Signalbreite mittels der Time-over-Threshold-Methode.

Um die Machbarkeit eines LGAD-basierten Systems zur Strahlzeitstrukturüberwachung zu demonstrieren, wurde ein vereinfachter Aufbau auf der Grundlage eines einzelnen LGAD-Sensors ($1\,\mathrm{cm}\times0.5\,\mathrm{cm}$) mit einer begrenzten Anzahl aktiver Kanäle vorbereitet und in der Versuchshalle des S-DALINAC getestet. Aufgrund der Anordnung des Aufbaus hatte der gelieferte Strahl eine Zeitstruktur von $3\,\mathrm{GHz}$. Bei dieser Proof-of-Principle-Demonstration wurde die $3\,\mathrm{GHz}$ Zeitstruktur des S-DALINAC-Strahls zum ersten Mal erfolgreich aufgelöst.

Um die Machbarkeit und Leistung eines LGAD-basierten Strahl-Zeitstruktur-Überwachungssystems zu untersuchen, wurde ein erweiterter Aufbau mit zwei $1\,\mathrm{cm}\times1\,\mathrm{cm}$ großen LGAD-Sensoren vorbereitet. Im Gegensatz zum ersten Proof-of-Principle-Experiment wurde das gesamte System mit einer verbesserten Ausleseelektronik ausgestattet. Außerdem wurde mit diesem verbesserten Aufbau die $3\,\mathrm{GHz}$ Zeitstruktur erfolgreich aufgelöst und eine intrinsische Zeitauflösung von $79\,\mathrm{ps}$ demonstriert.

Da die Installation des Aufbaus für die Proof-of-Concept-Studie außerhalb der Beschleunigerhalle erfolgen musste, konnte nur der Strahl mit der $6\,\mathrm{GHz}$ Zeitstruktur gemessen werden. In einem nächsten Schritt wurde eine Konzeptstudie mit Hilfe von Geant4-Simulationen durchgeführt, um die Machbarkeit eines LGAD-basierten Strahl-Zeitstruktur-Überwachungssystems für den ERL-Modus zu untersuchen. Um die Einsetzbarkeit von LGADs unter solchen Bedingungen zu bewerten, wurde eine Simulation mit der vereinfachten Geometrie der potenziellen Messstation erstellt. Diese Simulation zeigte die Machbarkeit eines LGAD-basierten Systems zur Überwachung der $6\,\mathrm{GHz}$ Strahl-Zeitstruktur. Außerdem konnte die beste Detektorposition innerhalb der Beschleunigerhalle ermittelt werden. In den kommenden Experimenten am S-DALINAC können die Ergebnisse der Simulationen und das Konzept verifiziert werden.

Schließlich wurde die Machbarkeit des maschinellen Lernens (ML) für die Datenanalyse der LGADs demonstriert. Es wurde gezeigt, dass der ML-Ansatz die für die LGAD-Korrektur erforderliche Datenmenge verringert,

ohne die zeitliche Auflösung zu beeinträchtigen. Darüber hinaus kann dieser Ansatz zur Implementierung eines Online-LGAD-Korrekturverfahrens verwendet werden.

1 Introduction

Particle accelerators play a major role in both science and industry. Over more than 100 years, particle accelerator designs and technologies have been continuously evolving, allowing them to reach higher energies and intensities with each iteration [1]. The early-stage accelerators used a permanent electric field to accelerate particles. Such a type of accelerator was limited by the electric breakdown between the accelerator's electrodes restricting the acceleration of particles to tens of MeV [1]. Subsequently, linear and circular accelerators were developed using changing electromagnetic fields to overcome the breakdown problem. Both of these types of accelerators allow much higher beam energies and currents, i.e. also a higher luminosity. The Large Hadron Collider (LHC), for example, currently has a maximal design proton beam energy of $7\,\text{TeV}$ and allows for a peak luminosity of 10^{34} cm^{-2}s^{-1} [2]. However, future experiments will require even higher beam energies or luminosities. In particular, a planned upgrade for the LHC, the so-called High-Luminosity LHC (HL-LHC), will bring luminosity up to 5×10^{34} cm^{-2}s^{-1} [3]. As a part of the upgrade, a large hadron-electron collider (LHeC) with a $60\,\text{GeV}$ electrons' design energy and a 2.3×10^{34} cm^{-2}s^{-1} luminosity is planned [4]. One of the biggest challenges for reaching the desired parameters is power consumption. For example, the required energy for the future at HL-LHC is about $1\,\text{GW}$ [4].

To overcome this limitation and reduce the required operational power, a so-called *energy recovery* linear accelerator (ERL) idea was introduced. The ERL concept was proposed by M. Tigner back in 1965 [5]. The idea is to recover beam energy after its usage for the intended purpose by injecting the beam into the main LINAC with a $180°$ phase shift. It allows the beam to transfer back energy to the radio frequency (RF) electric field in the accelerating cavities, which can be used to accelerate the next bunch. This re-usage of the beam energy consequently decreases the required RF power. In addition, this operation in ERL mode allows the acceleration of much higher beam currents using a fraction of the power required for traditional LINAC [6], which makes ERL a promising accelerator technology for future experiments.

The superconducting Darmstadt linear accelerator (S-DALINAC) located in Darmstadt, Germany, is one of the few accelerator facilities in the world which can be operated in the ERL mode. During the operation in the ERL mode a repetitive bunch rate of $6\,\text{GHz}$ is reached, which corresponds to $167\,\text{ps}$ between consecutive bunches. A monitoring system capable of resolving such a time structure is needed for monitoring purposes. A possible solution to resolve such time structure could be based on low-gain avalanche diodes (LGADs), which are novel silicon detectors especially designed for high-rate environments. LGADs are capable of simultaneously measuring the position and time of the particle with high precision. For example, in [7], a time resolution below $50\,\text{ps}$ was demonstrated using an LGAD strip sensor with a pitch of $146\,\mu\text{m}$.

The main goal of this thesis was to investigate the feasibility of an LGAD-based beam structure monitoring system for the S-DALINAC.

While this chapter provides an overview of the S-DALINAC and its operation in the ERL mode, Chapter 2 focuses on an introduction to silicon detectors and their working and operation principles. In Chapter 3, an overview of the LGAD technology will be given. This chapter will also introduce the basics of time measurements alongside the detector requirements to meet the designed time resolution. Furthermore, the application of an LGAD as a timing detector will be discussed. In Chapter 4, the feasibility study of the beam time structure monitoring system for the S-DALINAC operated in its non-ERL mode based on a simplified LGAD setup will be presented. Chapter 5 will cover a full-scale LGAD-based system performance at the

S-DALINAC. In Chapter 6, the performance of an LGAD-based beam monitoring system for the ERL mode will be discussed utilizing the Geant4 software for simulations. In Chapter 7, the feasibility of using machine learning algorithms to improve an LGAD data analysis and potential application for online data correction will be discussed.

1.1 Overview of the S-DALINAC facility

The S-DALINAC is a superconducting continuous wave electron linear accelerator (LINAC) located at the Technical University of Darmstadt [8]. Figure 1.1 exhibits the floor plan of the S-DALINAC (on the left) together with the experimental area (on the right). Electrons are produced by a thermionic gun with an energy of $250\,\mathrm{keV}$ [9] or by a spin polarised electron gun [10] with an energy of $125\,\mathrm{keV}$ [11]. The produced electrons are prepared in a chopper and pre-buncher section by time and velocity bunching [12]. After this, electrons match the $3\,\mathrm{GHz}$ operation frequency of the S-DALINAC and are ready to be injected into the main LINAC. In the superconducting injector section, which consists of two 20-cell superconducting radio frequency (SRF) cavities, electrons can be pre-accelerated up to $10\,\mathrm{MeV}$.
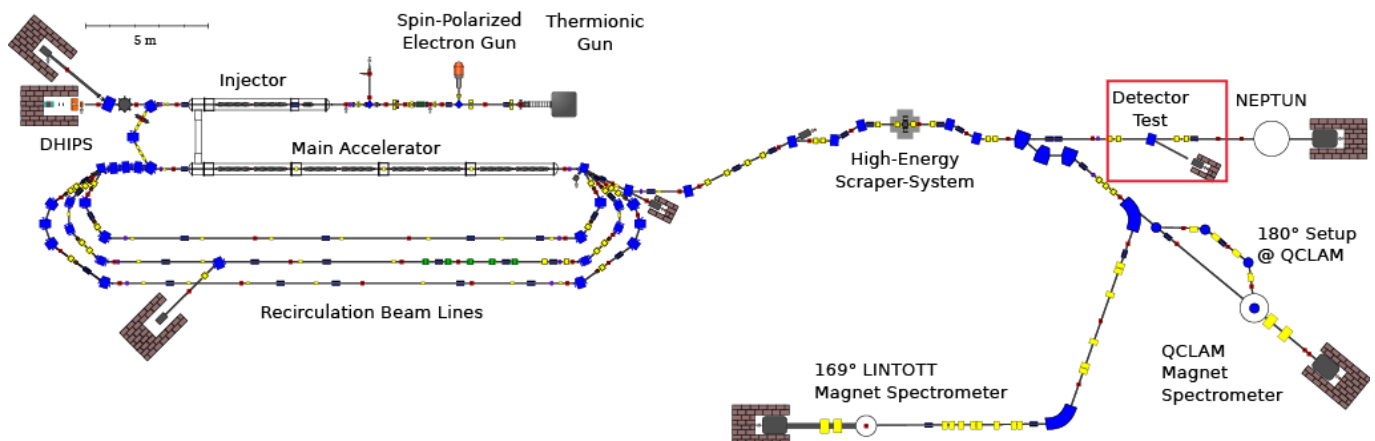
Figure 1.1: Floor plan of the S-DALINAC and an experimental area. The red rectangle demonstrates the detector placement for experiments presented in this work. Taken from [13].

After the pre-acceleration, electrons can be used for the Darmstadt High-Intensity Photon Setup (DHIPS) [14] or guided to the main LINAC for further acceleration. The main LINAC consists of eight 20-cell SRF cavities. Passing the main LINAC, the beam can be extracted to the experimental hall or recirculated inside the main LINAC up to three times using recirculation beamlines shown at the bottom left in Fig. 1.1. On each pass through the main LINAC, the beam energy is increased up to $30\,\mathrm{MeV}$. The maximum beam energy, which can be provided by the S-DALINAC, is $130\,\mathrm{MeV}$. At this energy, the beam current is limited to $20\,\mathrm{\mu A}$. The S-DALINAC beam parameters are summarized in Tab. 1.1.

After extraction of the beam to the experimental hall, it can be guided to several experimental areas: the NEPTUN [15] and the LINTOTT [16] or QCLAM [17] spectrometers. Additionally, a dedicated detector test area marked with a red rectangle in Fig. 1.1 was developed close to NEPTUN for detector tests with an electron beam [18]. The test area was used for experiments presented in this thesis.

Parameter	Value
Maximal beam energy	130 MeV
Maximal beam current	20 μA
Beam emittance	<1 mm mrad
Bunch length	5 ps
Bunch charge	up to 7 fC

Table 1.1: The S-DALINAC beam parameters. Values taken from [8].

1.2 S-DALINAC as an energy recovery LINAC

Initially, the S-DALINAC was built with two recirculation lines. During the upgrade in 2015/2016, a third recirculation line was installed [19, 20]. It enables the S-DALINAC operation as an ERL [21], making it one of few operational ERLs in the world [12].

1.2.1 One-turn ERL mode

The successful operation of the S-DALINAC in ERL mode was demonstrated in 2017 [11]. It was only made possible due to the installation of a path length adjustment system [11]. This system allows changing the distance a beam travels inside a beamline up to 10 cm. Setting the appropriate additional travel distance enables the beam re-injection into the main LINAC with a phase shift of $180°$ with respect to the RF phase in the cavities, which, subsequently, allows for the aforementioned ERL operational mode. It causes the beam to decelerate and, consequently, the energy to be transferred back to the RF field in the cavities, which enables the acceleration of the consecutive bunches without external RF power.

The basic concept of the S-DALINAC operation in one-turn ERL mode is shown in Fig. 1.2. Equation 1.1 describes the difference between an external power required for operation in normal and ERL modes and, consequently, the effectiveness of the energy recovery process. The RF-recovery effect can be used to characterize the efficiency of the ERL mode, which can be quantified as follows [11]

$$\xi_{RF} = \frac{P_{RF,acc} - P_{RF,erl}}{P_{RF,acc}},\tag{1.1}$$

where $P_{RF,acc}$ is the beam power when the beam is loaded externally at its maximum energy and $P_{RF,erl}$ is the power when the beam is loaded after its energy recovery. The maximal energy recovery effect is achieved when no external power is required in the ERL mode. The RF-recovery effect of (90.1 ± 0.3)% was demonstrated for one-turn ERL operation of the S-DALINAC [11].

1.2.2 Two-turn ERL mode

In August 2021, the successful S-DALINAC operation in multi-turn ERL mode was demonstrated [12]. During this operation, it was demonstrated that the energy recovery efficiency depends on the beam current and drops from about 85% for 0.2 μA below 60% for 7 μA [12].

The scheme of the S-DALINAC operation in two-turn ERL mode is shown in Fig. 1.3. In contrast to the one-turn ERL mode, two recirculation beamlines are used during the operation in the two-turn mode. One is used for recirculating the beam to the main LINAC with a $180°$ phase shift, while the other is used for the beam transport without a phase shift. Since the beamline that does not change the beam phase is used for the simultaneous transport of both once-accelerated and once-decelerated beams, a repetitive bunch rate of
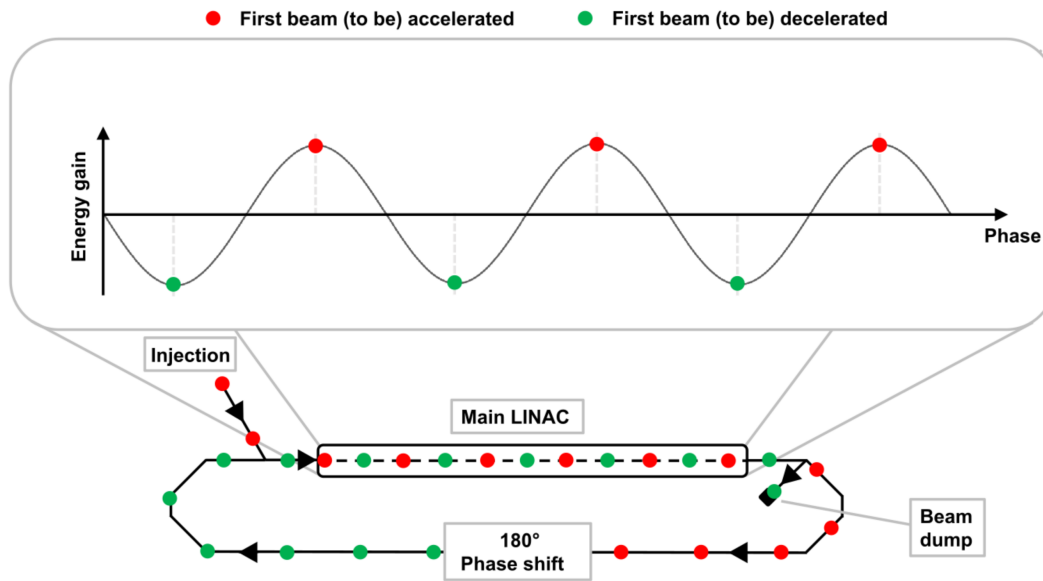
Figure 1.2: The scheme of the S-DALINAC operation in one-turn ERL mode. The red dots represent the bunches that are injected into the main LINAC for acceleration and the green dots for deceleration. Taken from [22].

$6\,\mathrm{GHz}$ is obtained. However, this shared beam transport introduces additional challenges for the operation in two-turn ERL mode as beam parameters should be optimized for both beams simultaneously [23]. For this reason, a dedicated beam monitoring system is required. Currently, several monitoring systems for the position determination of both beams simultaneously are in development [24].

1.3 Motivation of this work

As mentioned above, several monitoring systems are being developed for simultaneous position measurements of both beams inside the shared beamline [24]. However, all of these systems are designed only for the beam position measurement and are incapable of the beam phase measurement. Consequently, those systems cannot distinguish between the accelerated and decelerated beams, and calibration with only one of those beams is needed before measuring both beams. However, recent advances in timing detectors, which can measure the particle time-of-arrival with high timing precision, could provide a formidable solution as they allow bunch-to-bunch measurements via precise time measurement.

The work described in this thesis aims to develop a precise time measurement detector based on a novel silicon detector technology called LGAD. Pairing this detector with one of the position measurement systems will allow simultaneous bunch-to-bunch measurements and beam position measurements in the multi-turn ERL mode of the S-DALINAC with a $6\,\mathrm{GHz}$ time structure. To achieve this, first, the proof-of-principle demonstration experiment with a simplified system was performed. After that, a full system performance in the non-ERL S-DALINAC operation mode was evaluated. Lastly, a Geant4 simulation of the LGAD-based setup in the S-DALINAC ERL operation mode was done to estimate the system performance.

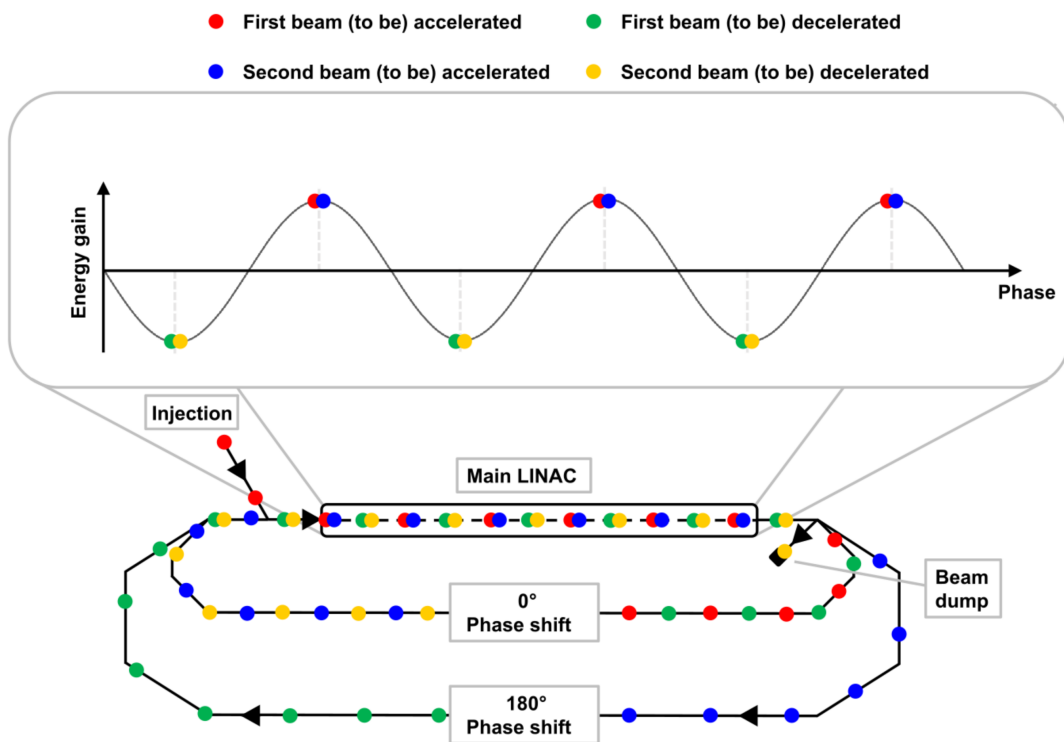Figure 1.3: The scheme of the S-DALINAC operation in two-turn ERL mode. The red dots represent the bunches injected into the main LINAC for the first acceleration cycle, the green dots for the first deceleration, the blue dots for the second acceleration, and the yellow dots for the second deceleration. The shared upper recirculation beamline where accelerated and decelerated beams travel simultaneously. Taken from [22].

2 Basics of silicon detectors

Solid materials can be divided into three groups based on their resistivity and conductivity: conductors, semiconductors, and insulators. While the resistivity is a material's property that defines the resistance to an electric current, the conductivity is defined by the inverse of the resistivity and describes the ability of the material to conduct the current. Both these properties come from charge carriers that become mobile due to the ionization of the material. Figure 2.1 exhibits these properties for selected materials from the groups mentioned above alongside typical ranges of conductivity and resistivity for the classification of each group. Materials with a low resistivity contain many metals, which have mobile electrons that can conduct current in any conditions. The second group is insulators, which are on the right part with large resistivity values. Those materials do not conduct current. Lastly, semiconductors are the materials between conductors and insulators. They do not conduct current in normal conditions but can become conductive due to external conditions, such as an electric field, temperature, etc.

Semiconductors have many applications not only in industry but also in science, e.g., as particle detectors for various physics experiments. Detector applications range from single photon detection to charged particle tracking. Different semiconducting materials are used in detector fabrication, from pure elements like silicon and germanium to different compounds. The most important material properties of semiconductor particle
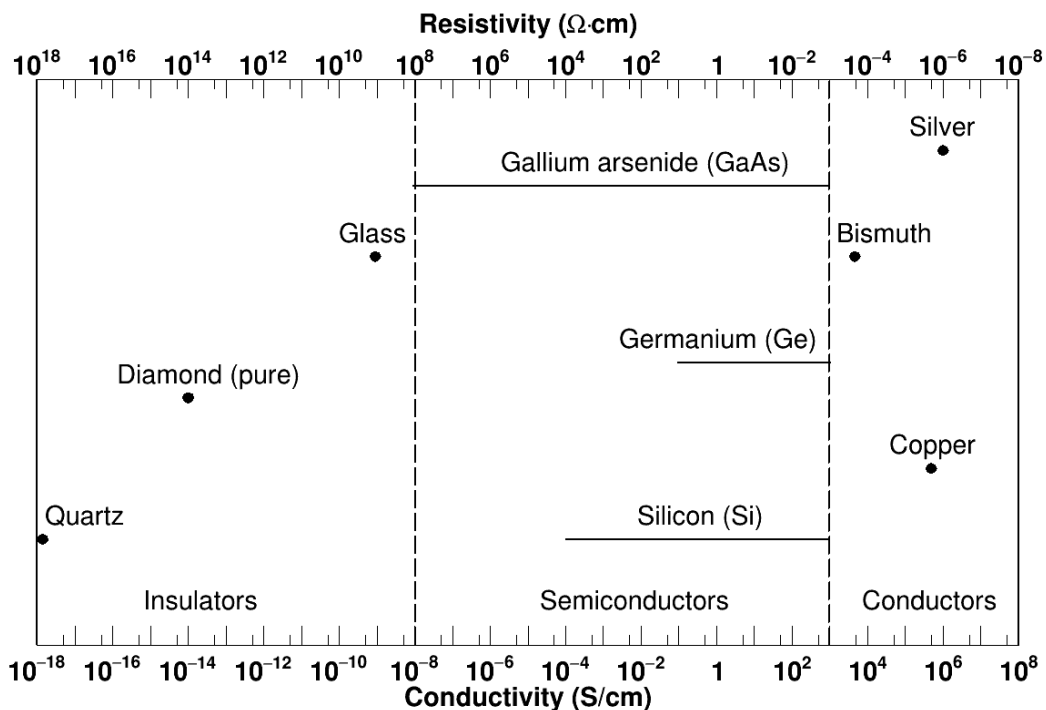

Figure 2.1: Conductivity and resistivity for selected conductors, semiconductors, and insulators. Adapted from [25].

Property	Material		
	Si	Ge	GaAs
atomic number (Z)	14	32	31/33
atom mass (u)	28.09	72.6	72.32
density ρ (g/cm^3)	2.328	5.327	5.32
band gap E_g (eV)	1.12	0.66	1.424
intrinsic charge carrier density (cm^{-3})	1.01×10^{10}	2.4×10^{13}	2.1×10^6
radiation length X_0 (cm)	9.36	2.3	2.29
average energy for (e/h) pair creation (eV)	3.65	2.96	4.2

Table 2.1: Selected properties of the silicon, germanium and gallium arsenide. Temperature-dependent properties are given at 300 K. Adapted from [25].

detectors are summarized in Tab. 2.1. A more detailed description of the individual properties will be discussed later in this chapter.

As this work is focused on the silicon-based detector, an overview of semiconductor physics and silicon-based detectors will be given in this chapter.

2.1 Semiconductor physics

2.1.1 Energy bands

In a single atom, electrons occupy orbitals that have discrete energy levels. However, according to Pauli's exclusion principle, electrons, which are fermions, cannot occupy the same quantum state simultaneously. In solid materials, on the other hand, atoms do not exist in isolation. Instead, they are organized in so-called crystal lattices, which are repeating structures of atoms. Consequently, each atom interacts with nearby atoms of the lattice, which leads to the splitting of individual energy levels. Some energy levels are so dense that one speaks of a continuous range of energies rather than discrete values. Such kinds of ranges are called *energy bands*, which are separated (except for conductors) by a *band gap*. The energy band formation is schematically
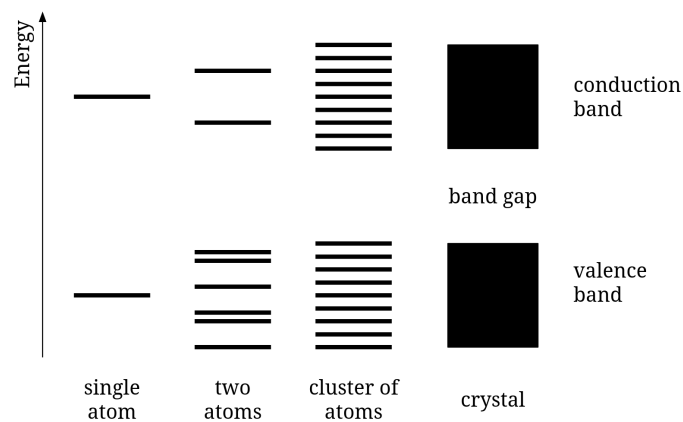

Figure 2.2: Energy bands formation for different groups of atoms. Adapted from [26].
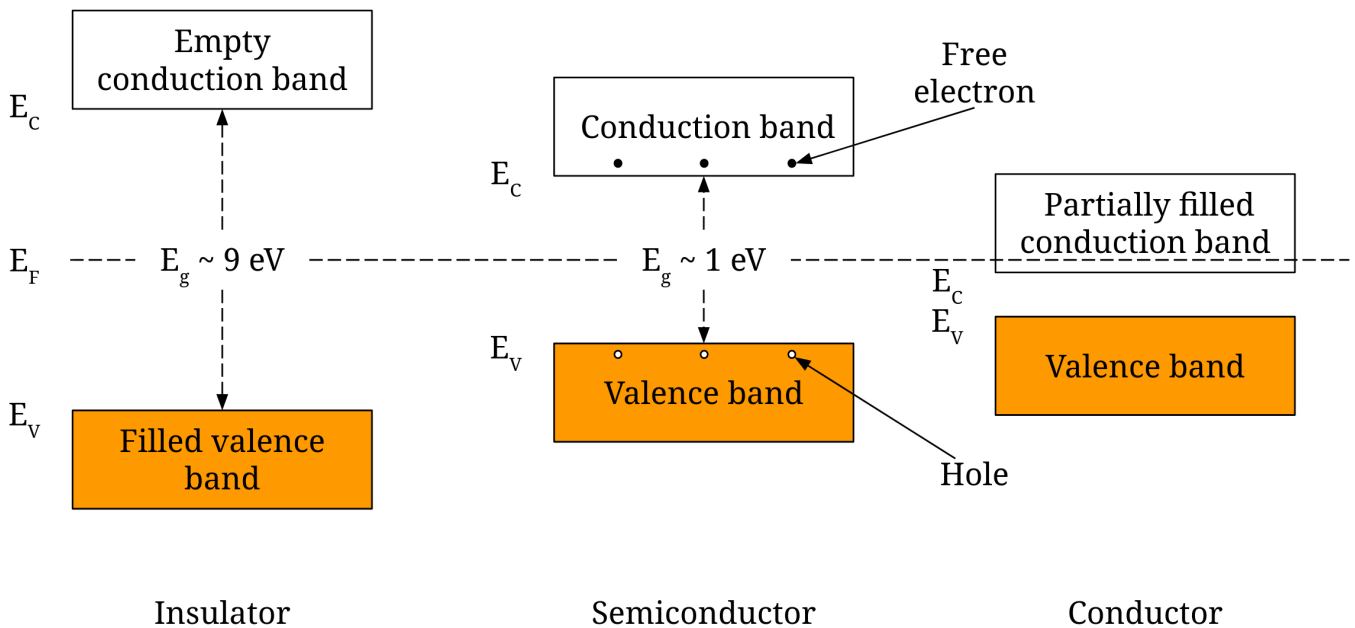
Figure 2.3: Energy bands diagram for conductor, semiconductor, and insulator. Adapted from [27].

demonstrated in Fig. 2.2. At absolute zero, the energy band with the lowest energy is the so-called *valence band* and the high energy band (*conduction band*) will be empty in insulators and semiconductors or partially filled in metal. The valence band can be characterized by the highest possible energy level in this band (denoted as E_V) and the conduction band by the lowest possible level for this band (denoted as E_C). The energy between the valence and the conduction band is known as the band gap E_g and is equal to the amount of energy, needed to transport an electron from a valence to a conduction band. In reality, not only two, but many bands are present. However, only the valence and conduction bands are important in terms of the conductive properties of materials. The main reason is that energy bands below the valence band are fully filled, and all energy bands above the conduction band are empty. Furthermore, electrons from the valence band do not contribute to the conductivity, as they cannot move between atoms. Conduction band electrons, however, are able to move between atoms acting as charge carriers. The schematic energy bands diagram for the insulator, semiconductor, and conductor is shown in Fig. 2.3.

In insulators, the gap between the conduction and valence band is relatively large (about a $10\,\text{eV}$). Therefore, the thermal energy of the electrons or external electric field is not enough to move an electron from a valence band to a conduction band. In conductors, conversely, either a valence and a conduction band overlap, or the conduction band is partially filled so that electrons can move among atoms and current can flow in the material. In semiconductors, on the other hand, a band gap is smaller when compared to insulators. Thus, if the temperature is high enough, thermally excited electrons can transition from the valence to the conduction band. According to [26], the band gap in semiconductors is not constant and changes with temperature and pressure.

The classification of materials based on their band gap (E_g) and carrier density (n) is shown in Tab. 2.2.

2.1.2 Charge carriers concentration in semiconductors

Charge carriers in semiconductors are electrons and holes. When electrons have enough energy for the transition from the valence to a conduction band, a vacancy is created in the valence band. This vacancy can

Material	E_g (eV)	n (cm^{-3})
Insulator	$E_g \geq 4$	$\ll 1$
Semiconductor	$0 < E_g < 4$	$< 10^{17}$
Semi-metal	$E_g \leq 0$	$10^{17} - 10^{21}$
Metal	no energy gap	10^{22}

Table 2.2: Classification of materials based on their respective energy gap E_g and intrinsic carrier density n at room temperature. Data taken from [27].

be described by a quasiparticle called *hole*. As a hole denotes the absence of an electron, it has a positive charge. The hole can be occupied by the electron from the valence band, consequently, creating a hole in the valence band. As surrounding electrons can occupy the created hole, it can be interpreted as a movement of the hole in the opposite direction from the electron. Electrons occupy bands starting from the lower to higher energy (Fig. 2.3). Subsequently, if holes are created in the lower energy levels, electrons move to the lower level, and holes move to the higher. Because of this, electrons occupy lower energy levels in the conduction band, while holes occupy higher levels in the valence band. Electrons in the conduction band and holes in the valence band can be interpreted as free particles which can conduct current.

Intrinsic semiconductors

The thermally generated amount of electrons and holes are the same in a pure semiconductor without any impurities, a so-called *intrinsic semiconductor*. The charge carrier distribution in the energy range dE can be described as

$$n(E)dE = g_n(E)f(E)dE \tag{2.1}$$

for electrons in the conduction band and as

$$p(E)d(E) = g_p(E)(1 - f(E))dE \tag{2.2}$$

for holes in the valence band. Here, $g_n(E)$ and $g_p(E)$ denote the density of energy states in the conduction and valence band, respectively, which are calculated as

$$g_n(E)dE = \frac{1}{2\pi^2}\left(\frac{2m_n}{\hbar^2}\right)^{3/2}\sqrt{E - E_C}dE, \tag{2.3}$$

$$g_p(E)dE = \frac{1}{2\pi^2}\left(\frac{2m_p}{\hbar^2}\right)^{3/2}\sqrt{E_V - E}dE, \tag{2.4}$$

using m_n and m_p as the effective mass of electron and hole, respectively, and $\hbar$ is the reduced Planck constant. The concept of effective mass comes from electrons (and holes) moving in a periodical lattice structure. The effective mass can be interpreted as the mass a particle seems to have when calculating its interactions in the periodical lattice [27]. The term f(E), on the other hand, describes the particles' distribution over energy states, which, for fermions such as electrons and holes, follow a Fermi-Dirac distribution:

$$f(E) = \frac{1}{exp\left(\frac{E - E_F}{kT}\right) + 1},$$

where k is the Boltzmann constant, T is the temperature, and E_F is the Fermi level. The Fermi level is the energy level which has exactly 50% probability to be occupied by an electron [27]. It should not be confused

with the Fermi energy, which is the highest occupied energy level for fermions at $0\,$K. As shown in Fig. 2.3, the Fermi level is in the middle of the band gap for intrinsic semiconductors. Integrating Eq. 2.1 and Eq. 2.2 gives the total electrons concentration in the conduction band

$$n = N_c exp\left(-\frac{E_C - E_F}{kT}\right),\tag{2.5}$$

and total holes concentration in the valence band

$$p = N_v exp\left(-\frac{E_F - E_V}{kT}\right),\tag{2.6}$$

where N_c and N_v are the effective level density in the conduction and a valence band, respectively [26].

Doped semiconductors

Introducing additional impurities in semiconductors changes their properties. Replacing some of the original atoms of a semiconductor with atoms that have a different number of valence electrons than the original atom (called doping) can lead to an excess number of electrons or holes. These introduced additional electrons and holes can freely move and, consequently, increase the conductivity of the doped material. Figure 2.4 schematically shows bonding in doped silicon with arsenic and boron atoms.

(a) n doped
(b) p doped
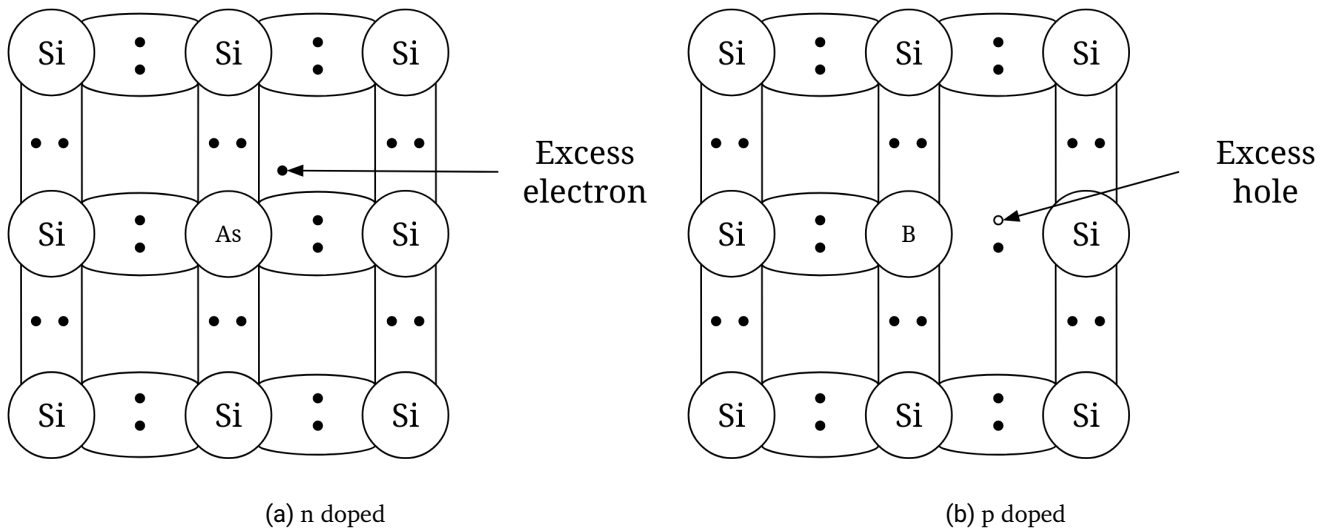
Figure 2.4: Doping in semiconductors with donor atoms (a) and acceptor atoms (b). Adapted from [25].

For pure silicon crystals, i.e. without doping, each atom forms a valence bond with four neighboring atoms. Replacing one silicon atom with an arsenic (As) atom, which has five valence electrons, one excess electron is obtained. Consequently, since this introduces an additional negative charge carrier, the semiconductor is called n-doped, and the doping atom is called a donor. In the case of doping with boron, which has only three valence electrons, the absence of one electron is created in the form of a hole. This type of semiconductor is therefore called p-doped (as a positive charge carrier is introduced) and the doping atom is called an acceptor. It is important to mention that doping atoms do not change the band gap in the original crystals; they only introduce additional donor (E_D) and acceptor (E_A) energy levels close to conductive and valence bands, respectively. Those additional energy levels, introduced by doping atoms, are shown in Fig. 2.5.

As the energy difference between the donor energy levels and the conduction band, as well as the acceptor energy levels and valence band, are much smaller than the band gap, conductivity can occur at lower temperatures. However, at very high temperatures, transitions from the valence to the conduction band become dominant, and the semiconductor behaves like an intrinsic semiconductor. The total charge carrier
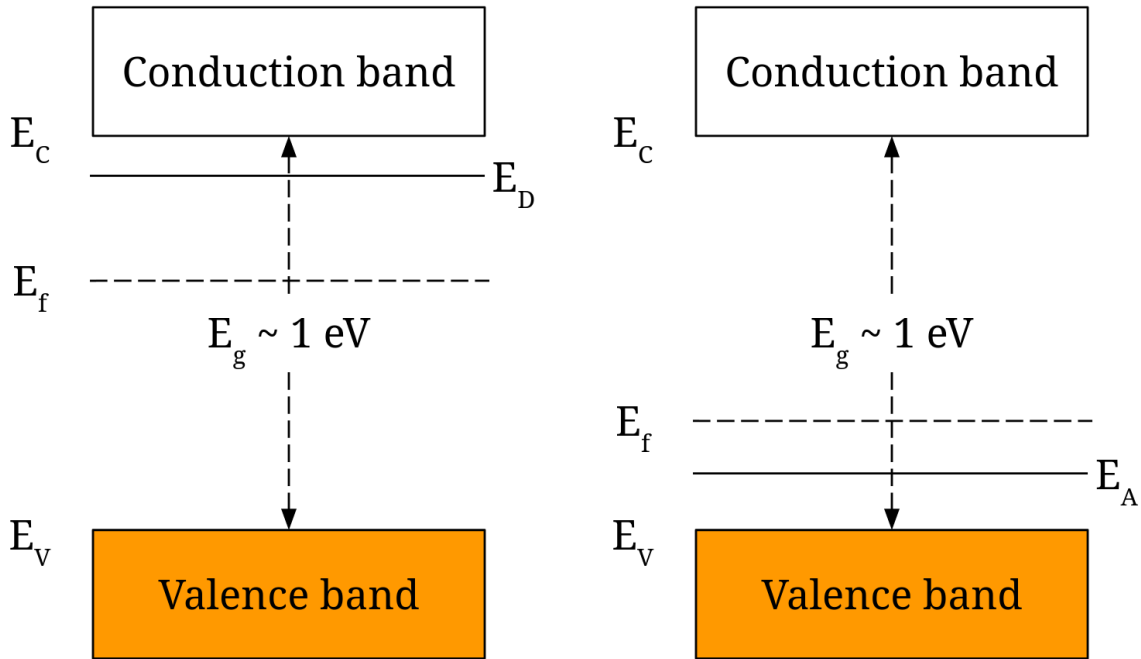

Figure 2.5: Energy bands structure in doped semiconductors. The left picture exhibits energy bands in a n-doped semiconductor and the right picture shows the energy bands for a p-doped semiconductor. Adapted from [27].

density in the case of doped semiconductors for n- and p-doping is:

$$n = n_i exp \left(\frac{E_f - E_F}{kT} \right), \qquad (2.7)$$

$$p = p_i exp \left(\frac{E_F - E_f}{kT} \right), \qquad (2.8)$$

where E_f is the new Fermi level in the doped semiconductor, n_i and p_i are the carrier density in the intrinsic semiconductor, given by Eq. 2.5 and Eq. 2.6, respectively [25].

2.1.3 P-n junction

When p- and n-doped materials are brought into contact, a so-called p-n junction is formed. In this case, a concentration gradient for both types of charge carriers is formed in the contact region, leading to a diffusion (see Sec. 2.1.4). Consequently, the electrons diffuse into the p-doped part and holes diffuse into the n-doped. Due to the electron-hole recombination processes in this region, the conduction electrons "re-occupy" the energy state in the valence band and, therefore, become bounded, which creates a zone with no charge carriers near the boundary, which is called a *depletion zone*. However, since atoms in this region become

ionized, this depletion zone features a *space charge*. Figure 2.6 demonstrates the process of a depletion zone creation. While the p layer features a space region with a negative charge, the n layer features a positive one.
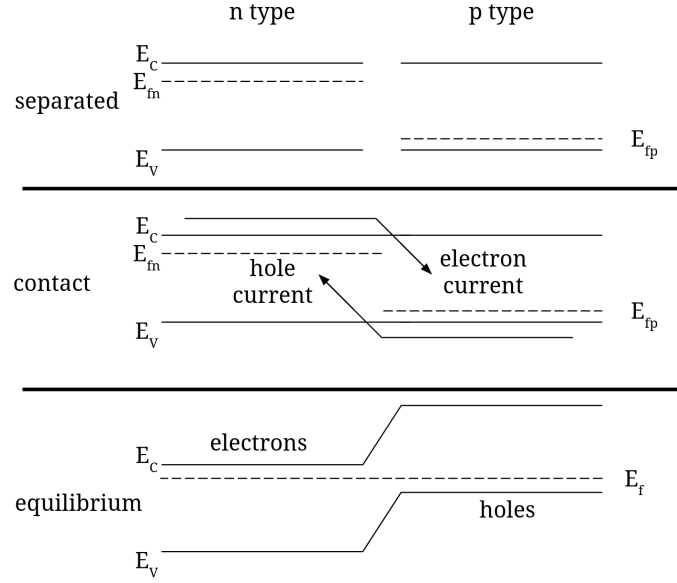

Figure 2.6: Creation of a depletion zone in p-n junction without external electric field. The upper plot shows p- and n-doped semiconductors separately. The middle plot exhibits a diffusion current at the moment semiconductors come into contact. The bottom plot demonstrates established equilibrium. Adapted from [28].

Due to this fact, an internal electric field is created which causes a drift current in the opposite direction of the diffusion. The drift and diffusion currents are in equilibrium without an external electric field. The resulting *diffusion potential* V_{bi} that prevents any charge transfer can be described as follows[25]:

$$V_{bi} = \frac{kT}{e} ln \frac{N_A N_D}{n_i^2},$$

where N_A and N_D are the doping atoms concentrations in p- and n-doped semiconductors, respectively, and $n_i^2 = np$ with n and p is electrons and holes concentrations defined by Eq. 2.7 and Eq. 2.8, respectively.

If an external electric field is present, it disturbs this equilibrium. Depending on the polarity of the applied external field, the aforementioned depletion zone can be increased or decreased. A p-n junction with an applied external voltage is shown in Fig. 2.7. Applying a positive potential to the p-doped side is called forward biasing (Fig. 2.7a). In this case, the depletion zone is decreased. If, on the other hand, a positive potential is applied to the n-doped side, the depletion zone increases, which is also referred to as reverse biasing (Fig. 2.7b).

The particle detectors are typically operated in reverse bias mode to have the full sensor depleted and, therefore, sensitive for the detection of ionizing particles. The current in reverse bias, which is described by the Schockley equation reads as follows [25]:

$$I = I_S \left(exp \left(\frac{eV_{ext}}{kT} \right) - 1 \right), \tag{2.9}$$

$$I_S = eA \left(\frac{D_n n_{p0}}{L_n} + \frac{D_p p_{n0}}{L_p} \right), \tag{2.10}$$
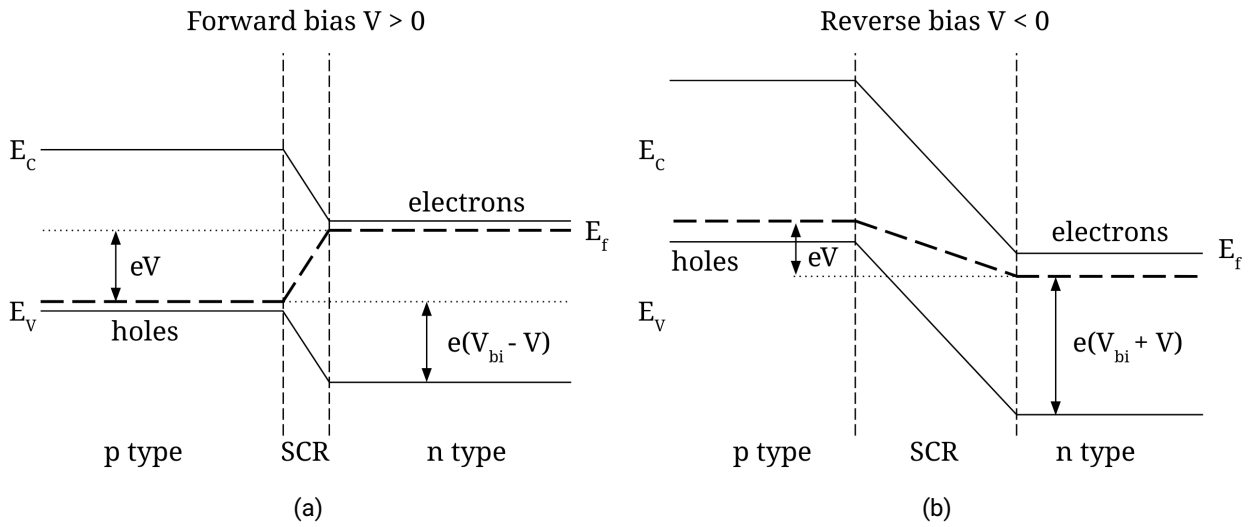
Figure 2.7: A p-n junction with applied external voltage. (a) shows applied forward bias, and (b) shows applied reverse bias. V_{bi} is a diffusion voltage and V is an external voltage. Adapted from [28].

where I_S is the saturation current in reverse bias, A is the contact area cross-section, $L_{n,p}$ the carriers diffusion length for electrons and holes, respectively, and n_{p0} and p_{n0} are the minority carrier densities in equilibrium for n- and p-doped semiconductors. The graphical representation of Eq. 2.9 is given in Fig. 2.8. As one can
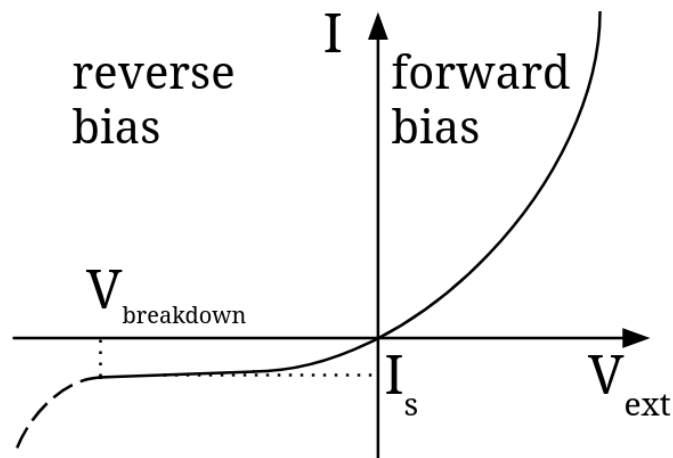
Figure 2.8: Schematic I-V relation in semiconductor diodes as described in Eq. 2.9. The dashed line represents the breakdown of the diode in case of high reverse bias. Adapted from [25].

see from Fig. 2.8, the current increases exponentially in the case of forward biasing. However, when a reverse bias is applied the current saturates at the value given by Eq. 2.10. The reverse bias value is limited by the electric breakdown.

Since fully depleting the sensor is important for the sensitivity to detect particles, an external voltage above the full depletion voltage V_{FD} should be applied. This value can be calculated as follows [28]:

$$V_{FD} = \frac{D^2}{2\epsilon\mu\rho},$$

where D is a detector thickness, $\epsilon = \epsilon_0 \epsilon_{sc}$ is the permittivity defined by the product of the vacuum permittivity and the semiconductor material and ρ is the resistivity.

2.1.4 Charge carriers transportation

Electrons and holes that are not bound with the lattice, e.g. the electrons in the conduction band and holes in the valence band, are free particles. Its transportation occurs due to drift and diffusion. The presence of an electric field $\vec{E}$ causes them to be able to drift, while a non-homogeneous charge concentration leads to the diffusion of charge carriers.

Drift

Even without the presence of an external electric field, charge carriers experience a random motion due to their thermal energy. The average displacement of the charge carriers, in this case, is zero. The mean distance between collisions is the so-called mean free path and the mean time between collisions (or mean free time) is τ. In the presence of an external electric field, the particle experiences a force equal to $q\vec{E}$. The momentum gain between two collisions equals $q|\vec{E}|\tau$ which, after re-writing, leads to

$$m_{eff}\vec{v}_D = q\vec{E}\tau, \tag{2.11}$$

where m_{eff} is an effective mass of the electron or hole as was introduced above and $q = \pm 1$ is the charge in terms of the elementary charge. Here $\vec{v}_D$ denotes the particle's drift velocity over a mean free path, which can be described as follows [25]:

$$\vec{v}_D = \frac{q\tau}{m_{eff}}\vec{E} = \mu\vec{E}. \tag{2.12}$$

The new parameter

$$\mu = \frac{q\tau}{m_{eff}}$$

is called mobility, which is an important concept in semiconductor physics that describes the influence of an external electric field on a particle's velocity. It has to be noted that due to different effective masses, electrons and holes have different mobility, as shown in Tab. 2.3. A drift current density $\vec{j}$ for electrons and holes can be expressed as follows:

$$\vec{j}_{n,drift} = -en\mu_n\vec{E} \quad \text{and} \quad \vec{j}_{p,drift} = ep\mu_p\vec{E}, \tag{2.13}$$

where e is the electron charge, $\mu_{n,p}$ the mobility of electrons and holes, and n and p are defined in Eq. 2.7 and Eq. 2.8, respectively.

The relation in Eq. 2.12 is only true for the low electric fields. However, at high enough electric fields, the velocity of charge carriers becomes saturated and no longer depends on this field. In this case, the drift velocity can be estimated as follows [26]

$$v_D = \frac{\mu_0 E}{\left(1 + \left(\frac{\mu_0 E}{v_{sat}}\right)^\beta\right)^{1/\beta}},$$

where v_{sat} is a saturated velocity, β is a temperature-dependant parameter and μ_0 is the mobility in the presence of a low electric field with no saturation effect.

Diffusion

A diffusion occurs when a charge carrier concentration gradient exists. In this case, carriers flow from a high-concentration region to a low-concentration region, causing a diffusion current. The created current density can be described as follows [25]:

$$\vec{j}_{n,diff} = -eD_n\vec{\nabla}n \quad \text{and} \quad \vec{j}_{p,diff} = -eD_p\vec{\nabla}p, \tag{2.14}$$

where D_n and D_p are the diffusion coefficients and $\vec{\nabla}n$ and $\vec{\nabla}p$ are the concentration gradients for electrons and holes respectively. The relation between the diffusion coefficients and carrier's mobility is expressed through so-called *Einstein relation*:

$$D_{n,p} = \frac{\mu_{n,p}kT}{e}$$

The total observer current is a combination of electron and hole current

$$\vec{j}_{total} = \vec{j}_n + \vec{j}_p,$$

which is, subsequently, a combination of a drift (Eq. 2.13) and diffusion(Eq. 2.14) [25] currents for electrons and holes respectively:

$$\vec{j}_n = -e\mu_n n\vec{E} - eD_n\vec{\nabla}n \quad \text{and} \quad \vec{j}_p = e\mu_p p\vec{E} - eD_p\vec{\nabla}p. \tag{2.15}$$

Equation 2.15 describes the current for both intrinsic and doped semiconductors. However, for homogeneous semiconductors, only the drift components play an important role, while for a p-n junction both drift and diffusion components are important.

A summary of the parameters that define the charge carriers transportation in semiconductors is shown in Tab.2.3 for selected semiconductors at a temperature of $300\,\text{K}$.

Material	Electrons mobility μ_n, $cm^2/(Vs)$	Holes mobility μ_p, $cm^2/(Vs)$	Saturation velocity v_{sat}, cm/s	Electron diffusion coefficient D_n, cm^2/s	Hole diffusion coefficient D_p, cm^2/s	Electron thermal drift velocity v_{th}^e, cm/s	Hole thermal drift velocity v_{th}^h, cm/s
Si	1450	500	1×10^7	36	12	2.3×10^7	1.65×10^7
Ge	3900	1800	7×10^6	100	50	3.1×10^7	1.9×10^7
Diamond	≈ 1900	≈ 2300	7×10^6	57	46	$\approx 10^7$	$\approx 10^7$

Table 2.3: Transportation parameters in selected semiconductors. The temperature dependant parameters are given at $300\,\text{K}$. Adapted from [25].

2.2 Operation principle of a silicon-based particle detector

As discussed above, to be sensitive enough for the detection of ionizing particles, the volume inside the semiconductor sensor should be fully depleted. In a fully depleted detector, the volume with no intrinsic charge carriers exists. Whenever an ionizing particle passes through this volume, electron-hole pairs are created and drift due to the external electric field. The charge carriers' drift allows the detection of the incident particles by measuring the current induced by the movement of those charge carriers.

The energy deposited by the incident particle is proportional to the created charge, and the energy measurements are enabled by collecting the created charge in the detector. However, to measure the hit position, a detector segmentation, which is typically realized through strips or pixels, is needed.

2.2.1 Energy loss of charged particle

The mean energy loss of a charged particle in the material due to interactions with the shell electrons of the target atoms, which is also called a *stopping power,* can be described by the Bethe-Bloch formula [25]:

$$-\left\langle \frac{dE}{dx} \right\rangle_c = K\frac{Z}{A}\rho\frac{z^2}{\beta^2}\left[\frac{1}{2}ln\frac{2m_ec^2\beta^2\gamma^2T_{max}}{I^2} - \beta^2 - \frac{\delta\beta\gamma}{2} - \frac{C(\beta\gamma, I)}{Z} \right]. \tag{2.16}$$

The parameters in Eq. 2.16 are briefly summarized in the following:

- $K = 4\pi N_A r_e^2 m_e c^2 = 0.307 MeV cm^2/mol$, where N_A is the Avogadro constant and r_e is the classical electron radius,

$$r_e = \frac{e^2}{4\pi\epsilon_0 m_e c^2},$$

  e is an elementary charge, m_e is an electron mass, c is the speed of light in a vacuum and ϵ_0 is a permittivity in a vacuum

- $z, \beta = v/c$ is the charge and velocity of an incident particle

- $\gamma = 1/\sqrt{1 - \beta^2}$ is the Lorentz factor

- Z, A is the atomic number and atomic mass of the material

- I is the mean excitation energy

- T_{max} is the maximum possible energy transfer to a shell electron defined as

$$T_{max} = \frac{2m_ec^2\beta^2\gamma^2}{1 + 2\gamma m_e/M + (m_e/M)^2},$$

  with M as the particle mass

- δ is the density correction factor, which is important for high-energy particles

- C/Z is the shell correction, important for small β values.

Another contribution to the energy loss comes from the interaction with atomic nuclei and the emission of photons. In this case, so-called radiative losses can be calculated as follows [27]:

$$-\left\langle \frac{dE}{dx} \right\rangle_r = \frac{NEZ(Z+1)e^4}{137m_o^2c^4}\left[4ln\frac{2E}{m_oc^2} - \frac{4}{3} \right], \tag{2.17}$$

where m_0 is the electron mass, N is the atom concentration in a medium, Z is the atomic number of the nuclei, and e is the elementary charge. In the case of heavy-charged particles, ionization is the main energy loss process. However, for electrons and positrons, radiative losses become dominant at lower energies due to their lower mass.

The total energy loss for electrons is the sum of Eq. 2.16 and Eq. 2.17:

$$\left\langle \frac{dE}{dx} \right\rangle_{total} = \left\langle \frac{dE}{dx} \right\rangle_c + \left\langle \frac{dE}{dx} \right\rangle_r$$

Figure 2.9 exhibits the total energy loss for electrons (Fig. 2.9a) and protons (Fig. 2.9b) in silicon which are a sum of collision and radiative losses for electrons and positrons and nuclear stopping power for ions. The nuclear stopping power is important for the ions due to their high mass and results from the scattering of ions on the nuclei.
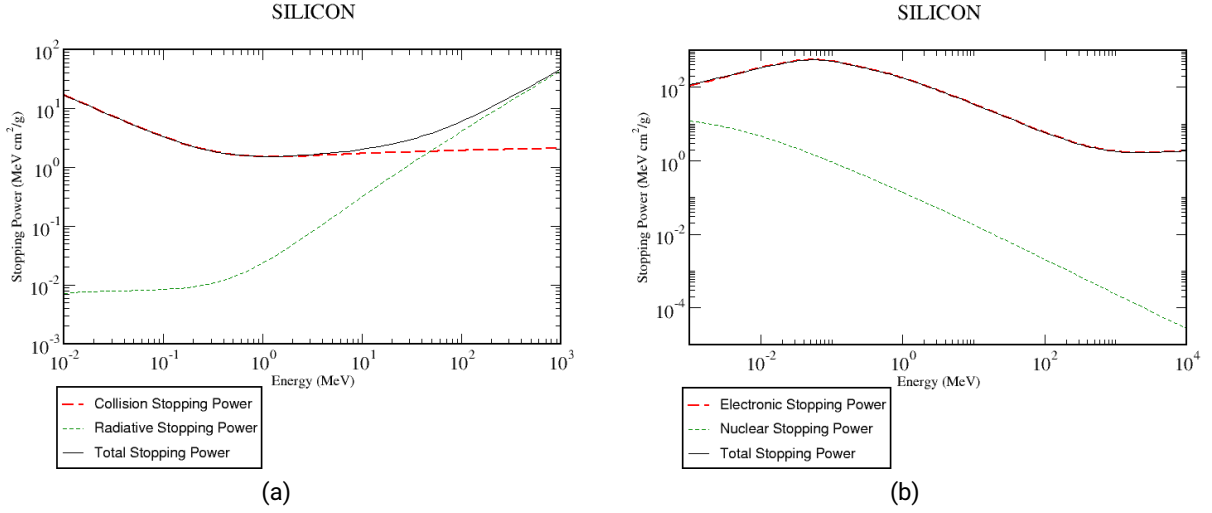

Figure 2.9: Energy loss in silicon for electrons (a) and protons (b). The data was obtained from the NIST PSTAR database [29].

2.2.2 Energy loss fluctuations

The first solution for the distribution of energy losses of a charged particle traveling through the medium was proposed by Landau with the assumptions that the electrons are quasi-free, and the particle's energy losses due to travel through the material are negligible [25]. However, those assumptions are only correct for minimum ionizing particles (MIPs) in thin detectors. MIPs are the particles that deposit energy at the minimum of the energy loss function defined by Eq. 2.16. In that case, the energy deposited by passing particles in a thin detector, follows the Landau distribution [25]:

$$f_L(\lambda) = \frac{1}{\pi} \int_0^\infty exp(-t \cdot lnt - \lambda \cdot t) * sin(\pi \cdot t) dt \tag{2.18}$$

The parameter λ is defined as follows [25]

$$\lambda = \lambda(\delta E_w, \xi) = \frac{\delta E - \delta E_w}{\xi} - 0.22278, \tag{2.19}$$

where δE_w is the most probable energy loss (maximum of Landau distribution) and ξ is a material dependant constant and defined via the Bethe-Bloch formula (Eq. 2.16) as follows [25]:

$$\xi = \frac{1}{2} K \frac{Z}{A} \rho \frac{z^2}{\beta^2} \Delta x,$$

using delta Δx as the material thickness and the other parameters as defined in Eq. 2.16. Figure 2.10 shows a Landau distribution. The long tail towards $\lambda \to \infty$ originates from a small number of events with large energy loss, causing a considerable asymmetry in the distribution. Because of this, the most probable value (MPV) is 30% lower than the average energy loss [28]. Because of that asymmetry, the MPV is used more often than the mean energy loss.
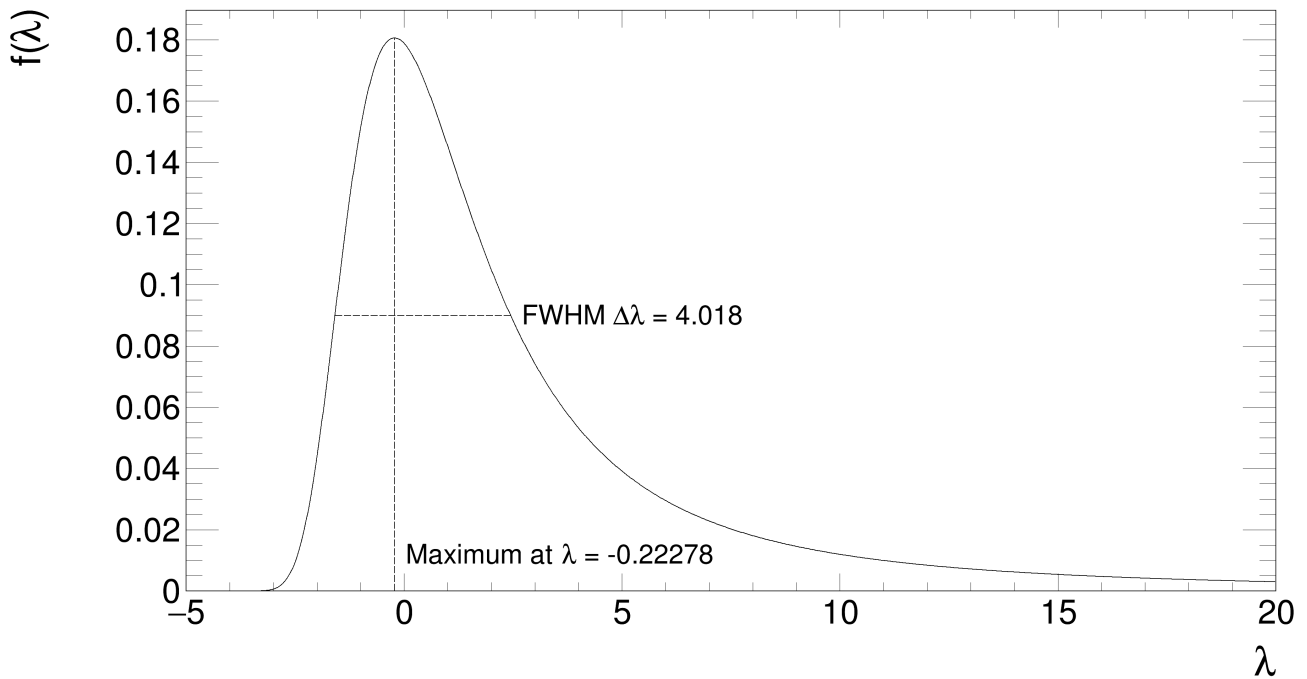
Figure 2.10: A Landau distribution. An MPV (maximum of a distribution) and full width at half maximum (FWHM) are shown in the figure. Produced with the ROOT analysis framework [30].

2.2.3 Signal formation in silicon detector

The basic overview of the operation of a simple n-in-p silicon detector is given in Fig. 2.11. This detector consists of a p-bulk (marked as p) region with the addition of the n-doped (denoted as n^+) and p-doped (marked as a p^+) implants with high respective charge carriers concentration. These implants form a pn-junction with a bulk region. Additionally, the readout electrodes are attached to the implants to form an
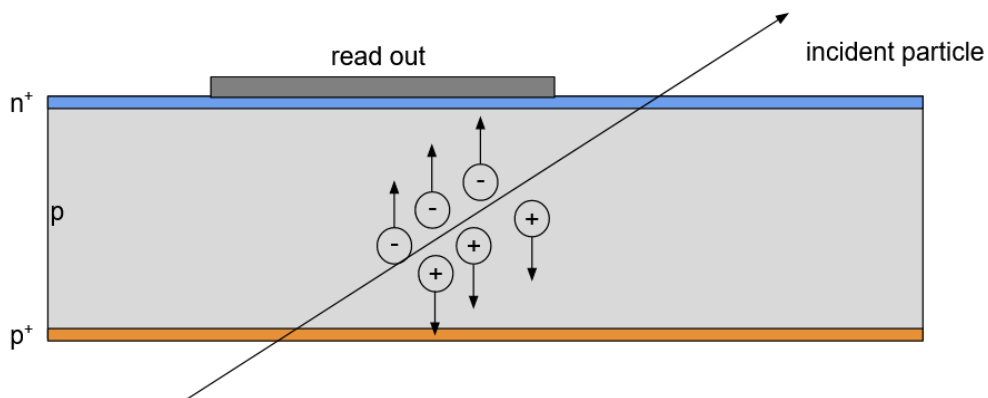

Figure 2.11: Signal formation in n-in-p silicon detector. The "+" sign next to n and p indicates higher doping concentrations. Electrons, denoted with the "-" sign, move towards the n^+ side, and holes (denoted with the "+" sign) move towards the p^+ side.

ohmic contact [28]. In the simplest case, the sensitive volume is directly connected (a so-called DC-coupling) to the readout electrodes.

When a particle passes through a detector, it loses energy and creates electron-hole pairs. Due to the presence of an electric field, holes drift towards the p^+ doped side while electrons drift towards the n^+ side. According to the Schockley-Ramo theorem [28], the charge movement induces a current that can be registered on the readout electrodes. In the last step, the readout chain pre-amplifies, shapes, and further processes the induced current, producing the resultant signal.

According to Tab. 2.1, the average energy for electron-hole pair creation (I) in silicon is $3.65\,\text{eV}$ at $300\,\text{K}$. The MPV for an energy loss for MIPs (dE/dx) in silicon is $0.28\,\text{keV}/\mu\text{m}$ [25]. The amount of generated electron-hole pairs in $300\,\mu\text{m}$ thick detector can be calculated as follows:

$$\frac{\left(\dfrac{dE}{dx}\right)_{MPV} * d}{I} = \frac{0.28\,\text{keV}/\mu\text{m} * 300\mu m}{3.65\,\text{eV}} = 2.3 * 10^4.$$

When compared to the intrinsic charge carrier density in silicon ($1.01 \times 10^{10}\,\text{cm}^{-3}$ according to Tab. 2.1), it becomes apparent that the number of created charge carriers due to the passage of a particle is much smaller. This again highlights the necessity to operate silicon detectors as a pn-diode with a reverse bias to create a depletion region and enable particle detection, as discussed in Sec. 2.1.3.

3 Low gain avalanche diodes

Silicon detectors have been used in physics for a long time. The main focus of silicon-based detector applications was position tracking and energy measurements. However, since the luminosity of physics experiments is continuously increasing, the requirements for particle detectors have also become more demanding. Due to the increasing luminosity, more particles have to be tracked at a time, which is particularly challenging for existing detector systems when overlapping events have to be resolved. However, adding the time information to already existing position information can improve the event reconstruction at those high particle rates [31]. This will allow higher luminosity for experiments.

Ultra-fast silicon detectors (UFSDs) based on LGADs are especially developed for such an application as they can simultaneously measure the position (with a resolution of tens μm) and time (with a resolution of tens ps) [32]. An overview of the basics of silicon detectors was given in the previous chapter. This chapter is focused on an LGAD's introduction together with the basics of time measurements.

3.1 Basics of an LGAD

3.1.1 Gain

Assuming a 100% efficient charge collection with a pn-diode operated as a detector, one can measure an induced current on a read-out electrode that is proportional to the number of electron-hole pairs created by charged particles passing through the detector as described in Sec. 2.2.3. However, it is possible to multiply initial electrons and holes by having a so-called gain (G) mechanism in the detector. The gain is defined as the ratio of the total observed electron-hole pairs (N_{eh}) compared to the number of electron-hole pairs produced without multiplication (N_{eh_0}) inside the detector ($G = N_{eh}/N_{eh_0}$). However, in order to achieve charge multiplication inside a silicon detector, an area with a high electric field (> 300 kV/cm [33]) has to be created. In such high fields, the charge carriers are accelerated to energies high enough to cause secondary ionization via impact ionization. This process is called an avalanche or avalanche multiplication. However, if the electric field is strong enough, the energy of secondary charge carriers is high enough to produce more secondary particles which, consequently, leads to an uncontrolled current flow in the detector. This effect is called an avalanche breakdown. However, it has to be mentioned that the avalanche breakdown can be stopped by employing the additional elements, such as quenching resistors, as described in [34]. Some silicon detectors, such as silicon photomultipliers (SiPMs) and some types of avalanche photodiodes (APDs), operate in the avalanche breakdown mode. APDs and SiPMs are widely used detectors with gains of several hundred [35] and 10000 and more [36], respectively. Such high gain is suitable for APD and SiPM applications but not for the timing measurements due to high noise levels and long charge collection time as a large number of electron-hole pairs is created per incident particle. Consequently, for a detector that aims at optimized timing performance, e.g. an LGAD, the gain should be in the order of 10-20 [31] to avoid avalanche breakdown and reach desirable timing resolution, which will be discussed in Sec. 3.2.

To allow impact ionization inside the LGAD, an electric field of about $300\,\text{kV/cm}$ [37] is required. This high electric field is not reachable by applying an external voltage (as it causes an electric breakdown in the detector) but by placing an additional positively doped (gain) layer close to the negative electrode of the
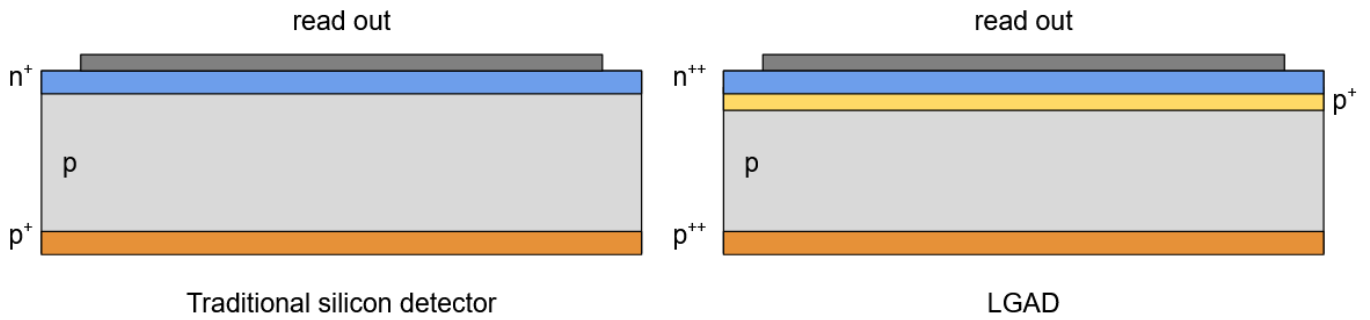
Figure 3.1: Schematics of a traditional n-in-p silicon sensor (left) and an LGAD (right). Adapted from [38].

detector. Boron and Gallium are typical implants used in LGADs with a concentration of about $10^{16}\,\mathrm{cm}^{-3}$ [39]. The total amount of charge carriers after the multiplication process can be described as follows according to [37]:

$$N(d) = N_0 \cdot exp(\alpha(E) \cdot d),$$

where N_0 is the number of charge carriers before multiplication, d is the path length of the particle in the detector's sensitive volume, and $\alpha(E)$ is the impact ionization rate. The comparison of a conventional n-in-p silicon detector and an LGAD sensor is shown in Fig. 3.1. As one can see, an additional positively doped layer (shown in yellow and marked as p^+) close to the n-implant is introduced in the LGAD. It creates a local high electric field that allows charge multiplication, as discussed above.

3.1.2 Signal formation

As described in Sec. 2.2.3, after the ionization particles pass through the detector, the charge carriers are created. Electrons drift towards the negative electrode and holes drift towards the positive. When electrons pass through the gain region their kinetic energy becomes high enough for impact ionization, and additional (gain) electron-hole pairs are created.

To demonstrate the signal formation in LGADs in more detail, a Weightfield2 [40] simulation of the MIPs signal in a $50\,\mathrm{\mu m}$ thick LGAD with gain 15 was done in [33] and is shown in Fig. 3.2. Gain electrons, created closely to the negative electrode, are absorbed after a short drift distance. Consequently, they only contribute at the beginning of the signal. However, gain holes, drifting towards the opposite side of the detector, have the largest contribution to the signal.

3.1.3 Detector segmentation

As mentioned, the LGAD is designed for simultaneous time and position measurements. The sensitivity to the particle position is reached through the detector's segmentation. Several LGAD designs are developed with different segmentation methods. The very first LGAD design with segmentation employed additional structures, namely junction termination extension (JTE) and p-stop implants to avoid electric breakdown between the readout contacts in the segmented detector. An LGAD scheme with JTE and p-stop is shown in Fig. 3.3.

However, the presence of JTEs and p-stops introduces a region in sensor volume where no multiplication occurs due to the absence of the doping layer. Consequently, no high electric field is created in this region, which, therefore, also features no or a reduced gain. In such an area, where no full gain is reached, either the time resolution strongly deteriorates, or no signal can be detected at all. Consequently, this region is often referred to as the dead area of the sensor. An example of a gain profile and dead area with no gain caused by
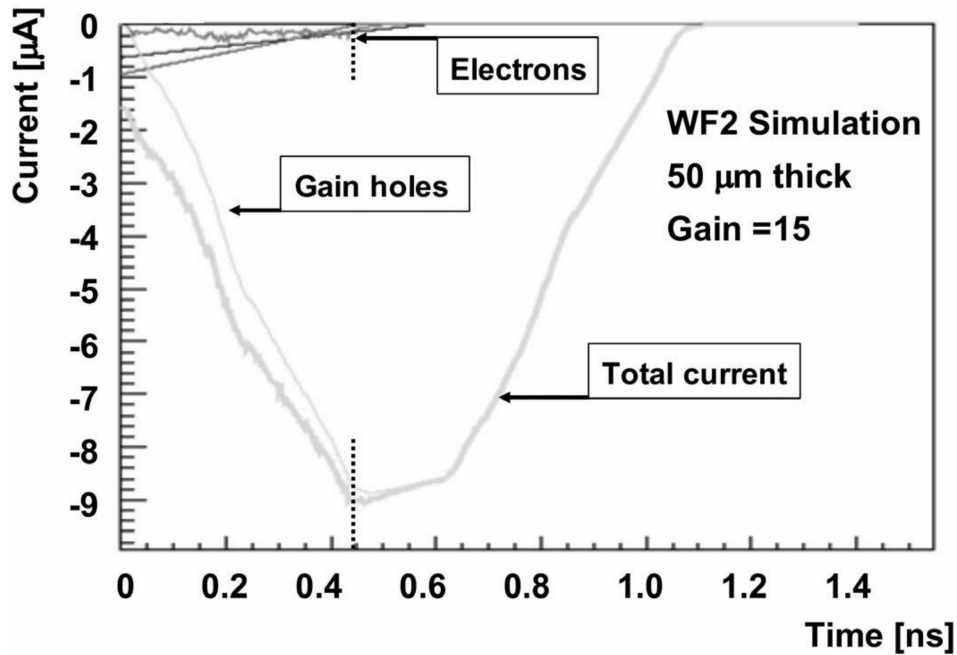
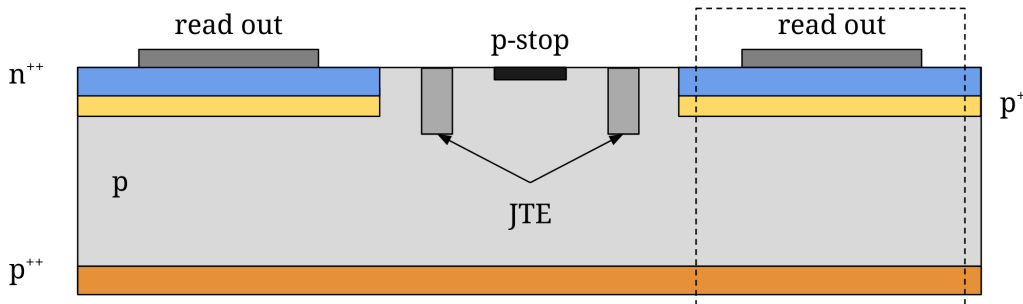Figure 3.2: LGAD simulated signal for MIPs in a $50\,\mu m$ thick sensor with gain 15. Taken from [33].

Figure 3.3: LGAD schematic with JTE and p-stop. The dashed area represents simplified schematics of LGAD as in Fig. 3.1. Based on description in [33] and [41].

the aforementioned segmentation method is shown in Fig. 3.4. Considering that not all detector volumes are sensitive to the initial passing particle, as there are regions without gain, a new parameter to represent the detector's sensitive volume can be introduced. To describe what part of the sensor is sensitive to the particles, we can introduce the so-called fill factor, which is defined as the ratio between the detector area with gain to the total detector area:

$$\text{fill factor} = \frac{\text{gain area}}{\text{total area}}.$$

Consequently, to achieve the best possible detection efficiency, the dead area without gain should be minimized. Several different segmentation methods were developed to reduce the no-gain region in LGADs: double-sided LGAD, resistive AC-coupled silicon detector, and trench-isolated LGAD. Those segmentation methods are schematically shown in Fig. 3.5. In a double-sided LGAD, the gain layer is continuous, and the segmentation is done on the back side of the detector. In the case of trench-isolated LGADs, the electrical isolation of the read-out contacts is done in the form of physical trenches (in size of a few microns) in silicon, filled with silicon oxide. For a resistive AC-coupled silicon detector, there is also no segmentation in the gain layer. In
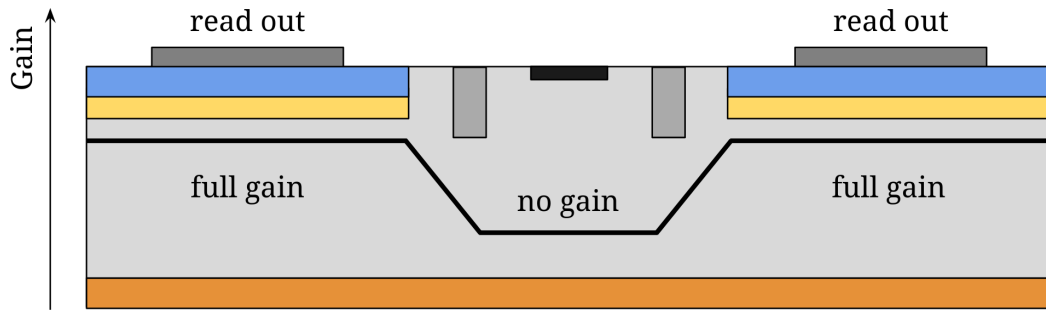
Figure 3.4: Scheme of an LGAD gain profile and dead area, introduced by JTE and p-stop for sensor, shown in Fig. 3.3. Based on description in [33] and [41].
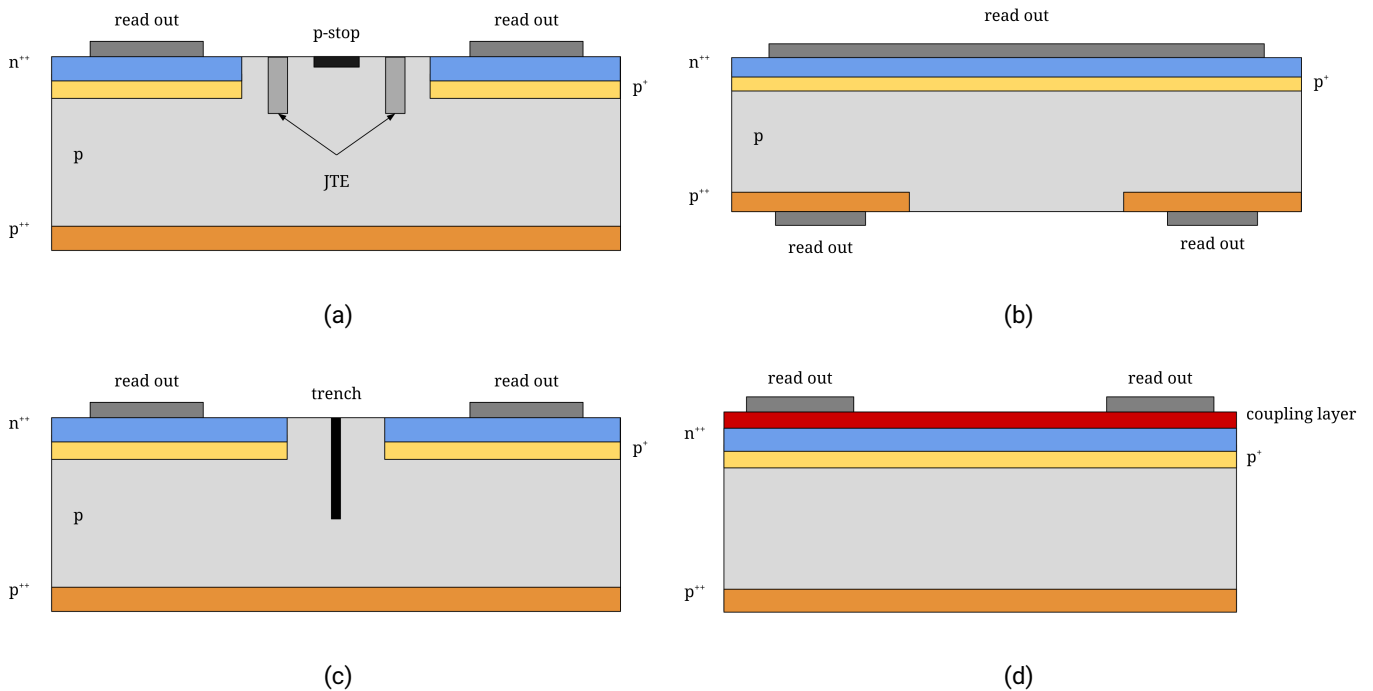

Figure 3.5: Different LGAD segmentation technologies: (a) shows LGAD segmentation with JTE, (b) shows double-sided LGAD, (c) shows trench isolated LGAD, and (d) shows resistive AC-coupled LGAD. Based on the description in [42].

this case, the segmentation is done through read-out contacts that are capacitively coupled to the detector via an additional dielectric layer.

All sensors used in this work employed the LGADs with the JTE segmentation methods.

3.2 Basics of time measurements

3.2.1 Electronics

The ability to detect particles with a time resolution of several tens of picoseconds is the main goal for LGAD-based particle detection systems. To achieve this goal, suitable readout electronics are also vital. Figure 3.6 exhibits the main components of such a time measurement detector. First of all, a detector able to produce
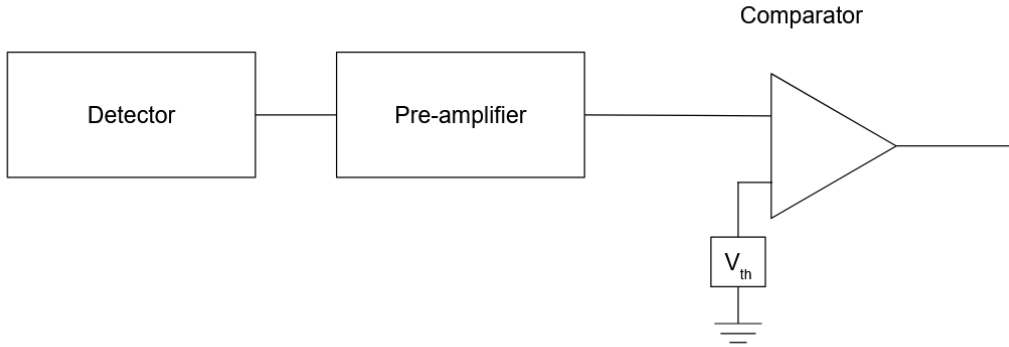

Figure 3.6: Scheme of the detector's read-out chain for time measurements. Adapted from [31].

signals with constant shape is needed. The signal amplitude should ideally depend linearly on the energy deposited inside the detector. First, the pre-amplifier reads out the initial signal generated inside the sensor and shapes it. In the next step, the amplitude of the shaped signal is compared to a threshold voltage (V_{th}), and the signal is digitized by a time-to-digital converter (TDC).

3.2.2 Measurement principle

The measurements performed in this work are based on the so-called time over the threshold (ToT) method which measures the signal width utilizing a leading-edge discriminator. The scheme of the measurements is shown in Fig. 3.7. As discussed above, the pre-amplified signal is compared with a constant threshold voltage V_{th}. If the signal is above the threshold, it's further processed. In the ToT method, the time of crossing the threshold is recorded. The rising part of the signal from 0 to the amplitude S is called a leading edge, and the respective time is called a rising time t_r. Consequently, the falling part from the amplitude S to 0 is called a trailing edge. When the signal rises above the threshold, the so-called *leading edge time* (t_{LE}) is recorded. Consequently, when the signal falls below the threshold, the *trailing edge time* (t_{TE}) is recorded. The ToT (the width of the signal) is calculated as follows: $ToT = t_{TE} - t_{LE}$. It is worth mentioning that the leading edge time is often called the time of arrival (ToA) as it denotes the time when the particle was registered. Further in this dissertation, the ToT will be used to indicate the signal width and ToA to indicate the particle registration time.

3.3 Precision of the time measurement

According to [31], several effects contribute to the time resolution (σ_{total}) of the detector as follows:

$$\sigma_{total}^2 = \sigma_{TimeWalk}^2 + \sigma_{LandauFluctuations}^2 + \sigma_{distortion}^2 + \sigma_{jitter}^2 + \sigma_{TDC}^2, \tag{3.1}$$
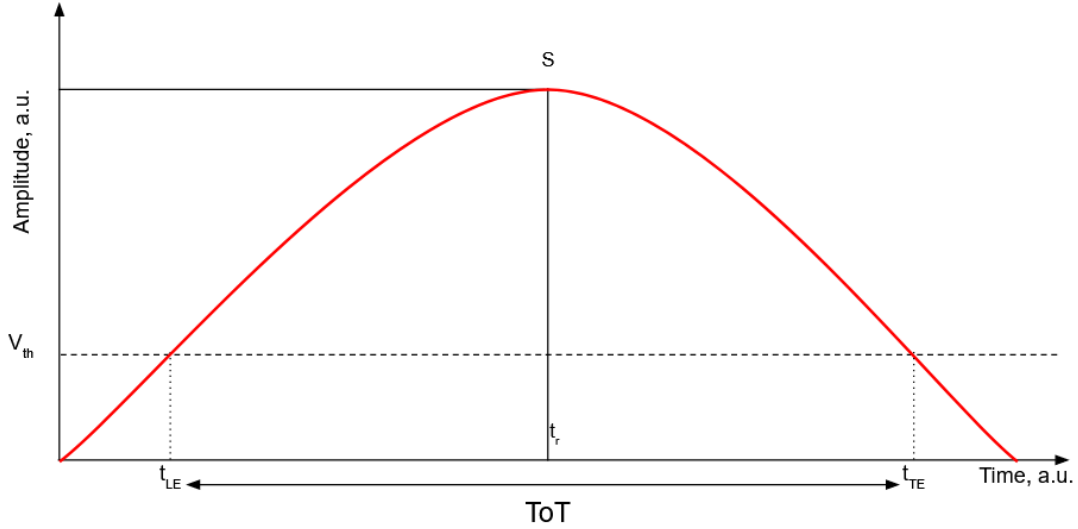
Figure 3.7: Scheme of the time measurement utilizing the leading-edge discriminator. The horizontal dashed line represents threshold voltage V_{th}, t_{LE}, and t_{TE} represents the time of leading and trailing edge, respectively, and t_r denotes the rise time to the maximum of the signal (amplitude) S.

where $\sigma_{TimeWalk}$ represent the contribution from the time walk effect, $\sigma_{LandauFluctuations}$ represent the effect of Landau fluctuations, $\sigma_{distortion}$ represent the effect of the non-uniform electric field inside the sensor and σ_{jitter} represent the jitter effect contribution to the total time resolution. The last contribution that comes from the TDC, is defined as $\sigma_{TDC} = \Delta T/\sqrt{12}$, where ΔT is the TDC binning and can be reduced by employing TDC with high resolution.

3.3.1 Landau fluctuations

As described in Sec. 2.2.2, the energy deposition inside a thin silicon detector follows a Landau distribution (Eq. 2.18). The energy deposition inside such a detector can be described as the sum of individual energy loss processes:

$$\Delta E_{deposited} = \sum_{i=1}^{N} \Delta E_i,$$

where N is the number of interactions in the detector material and ΔE_i is the energy loss of the individual interactions. Both the number of collisions and corresponding energy loss vary on an event-by-event basis. This fact leads to different amounts of electron-hole pairs produced by each individual particle. Consequently, not only the amplitude but also the shape of the signal varies. This effect is also referred to as Landau fluctuations. To highlight the significance of those Landau fluctuations, Fig. 3.8 shows the energy deposition and the resulting signal for two different events in a silicon detector with gain one in the entire sensor volume and the resulting signal in the detector for two different events. As described above, the variation in the energy deposition in these two events led to variations in both the signal amplitude and shape, as shown on the right-hand side of Fig. 3.8. Several methods can be used to compensate for variations in the signal amplitude, which will be briefly introduced in Sec. 3.3.2. Variations in the signal shape, however, cannot be compensated fully as they originate from the physics of energy deposition. The contribution of those Landau fluctuations can only be reduced by employing a thinner sensor. In this case, the energy deposition will be more uniform than inside a thick sensor. However, there is a lower limit for Landau fluctuation that varies depending on
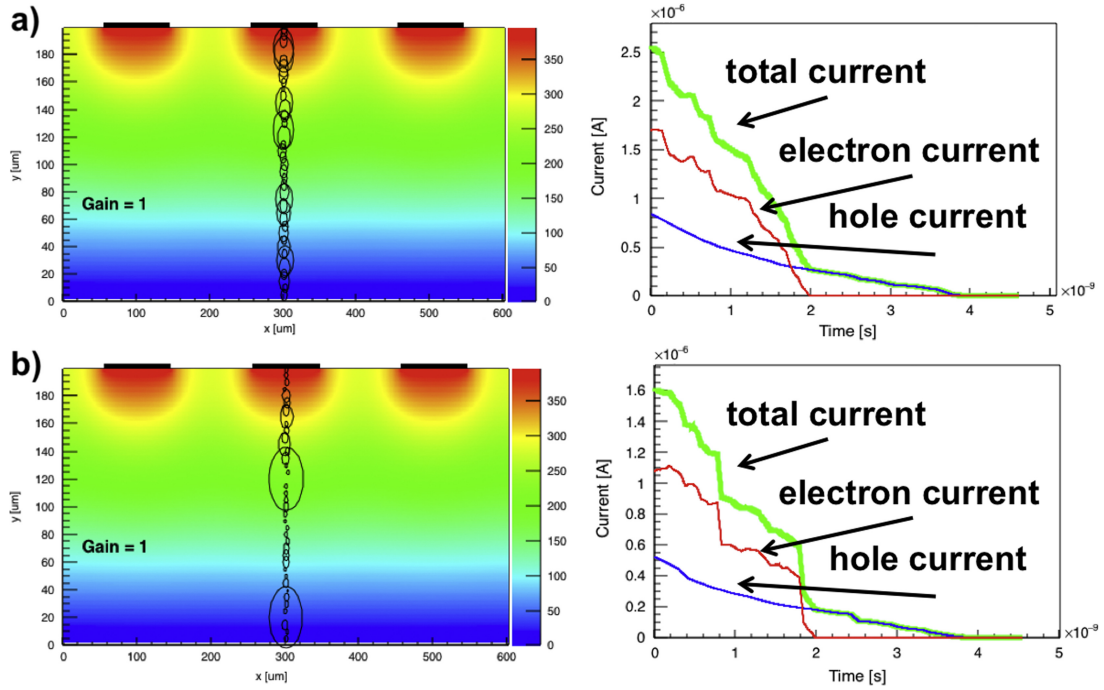
Figure 3.8: An energy deposition in a silicon detector with gain one in two different events, represented by (a) and (b). The left part of the figure shows a simulated energy deposition in a detector and the corresponding signal is shown in the right part. Taken from [43].

the detector thickness. E.g for $50\,\mu m$ thick LGADs it is $\sim 25\,ps$ and for $300\,\mu m$ thick sensors it is $\sim 60\,ps$ [33]. Consequently, Landau fluctuations are the major contribution to the total detector timing performance [37].

3.3.2 Time walk effect

As mentioned in Sec. 3.3.1, the signal amplitude can vary for individual particles. Consequently, after shaping the signal and comparing it to the constant threshold V_{th} (Fig. 3.9), the signals with lower amplitude cross the threshold value later than signals with higher amplitude, leading to a delay in the signal registration. This effect, which is also called the time walk effect, is exhibited in Fig. 3.9. According to [31], the time walk can be described as the root mean square (RMS) value of threshold crossing delay :

$$\sigma_{TimeWalk} = [t_d]_{RMS} = \left[\frac{V_{th}}{S/t_r}\right]_{RMS} \propto \left[\frac{N}{dV/dt}\right]_{RMS},$$

where S is the signal amplitude, t_r is the rise time to signal amplitude S, t_d is the delay before crossing the threshold. Also, the relation $S/t_r = dV/dt$ was used with dV/dt denoting the so-called slew rate. The slew rate is a characteristic of how fast the signal is rising. N represents the noise in the system. The threshold value V_{th} is often represented as a value proportional to the noise level N.

There are several methods to mitigate the time walk effect. The first method relies on a constant fraction discriminator (CFD). In the case of CFD, instead of a fixed threshold value, the threshold is set to a certain fraction of the signal amplitude S (e.g. 5%, 10%, etc.). Consequently, the absolute value of V_{th} is different for signals with different amplitudes, but the rise time from 0 to V_{th} would be the same for all signals, and, therefore, no time walk will be present. The second method is to measure and compensate for the time walk effect using the ToT of the signal. Last, there is the so-called multi-sampling (MS) method, which is generally
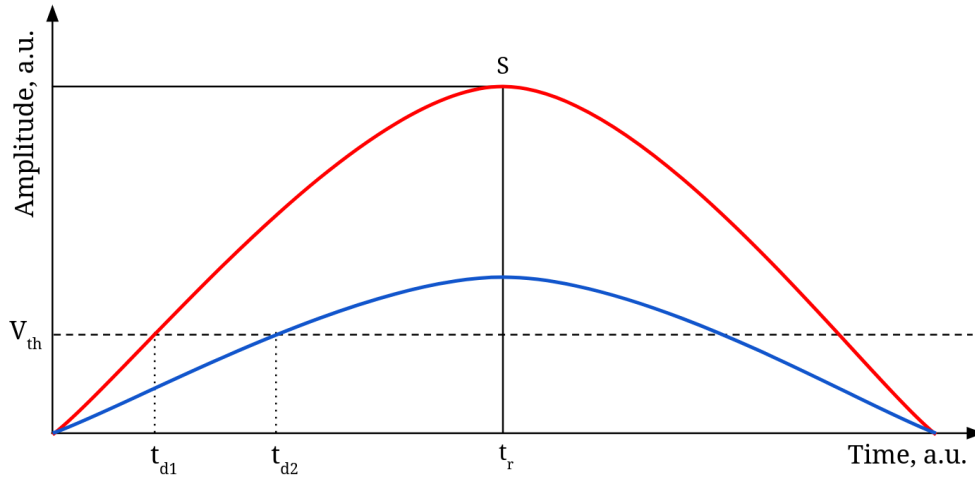
Figure 3.9: Schematic illustration of a time walk effect. V_{th} represent threshold level, t_{d1} and t_{d2} is the ToA of two signals, t_r is the rise time from 0 to signal maximum amplitude S. Difference between t_{d1} and t_{d2} represent a time walk effect.

more complicated than the CFD and ToT methods as MS requires the digitization of the signal waveforms. The ToT compensation method was used in this work, which will be further discussed in Chapter 4 and Chapter 5.

3.3.3 Jitter effect

Another effect that influences the time precision is due to the presence of noise in the system, which is also called jitter. As shown in Fig. 3.10, due to the noise, the firing time of the comparator is shifted (jitter effect). This effect can be described as follows [31]:

$$\sigma_{jitter} = \frac{N}{dV/dt},$$

where the N is the noise level in the system and dV/dt is a slew rate. A jitter contribution can be lowered by keeping the noise in the system low and having a larger slew rate.

3.3.4 Non-uniform electric field and non-saturated drift velocity

According to [31], the shape of the signal can be calculated using the Ramo–Shockley's theorem:

$$i(t) = -q \cdot \vec{v} \cdot \overrightarrow{E_w}, \tag{3.2}$$

where q is the charge of the particle, $\vec{v}$ is the drift velocity and $\overrightarrow{E_w}$ is the weighting field [25]. The weighting field describes the coupling of the charge to the readout electrodes. As one can see from Eq. 3.2, both the drift velocity and the weighting field define the signal's shape. Ideally, the drift velocity should be constant in the entire detector volume. A non-uniform drift velocity causes variations in the shape of signals, which, consequently, worsens the time resolution. The solution to mitigate this effect and have a more uniform signal shape is to saturate the drift velocity. To achieve this, the electric field should be high enough in the entire detector volume to saturate the velocity. At room temperature, the drift velocity saturates at field values $\sim 30\,\mathrm{kV/cm}$ [31]. Cooling down the detector allows to saturate the drift velocity at even lower electric fields.
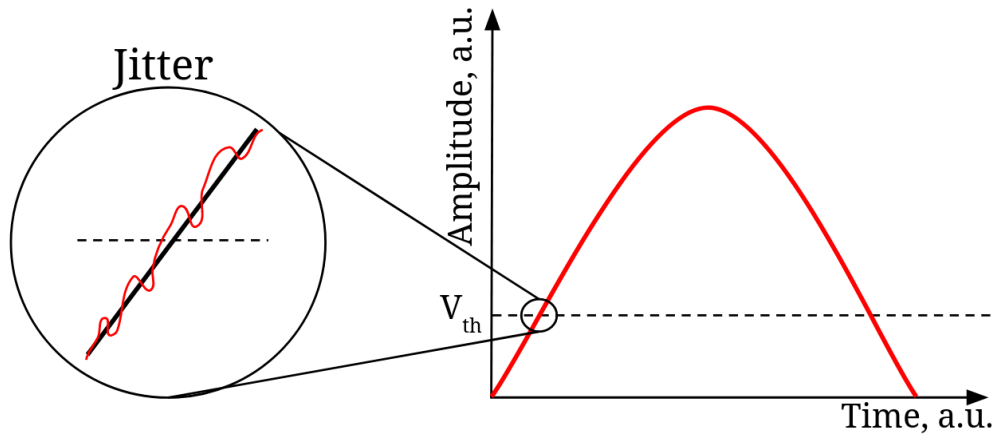
Figure 3.10: Illustration of a jitter. The firing time of the comparator is shifted due to the noise in the system.

Similar requirements are also needed for the weighting field. Ideally, it should be uniform in the entire detector volume. In the case of a non-uniform weighting field, the shape of the signal becomes position-dependent, leading to variations in the signal shape, which, as mentioned before, deteriorates the time resolution. Since the weighting field strongly depends on the detector geometry and segmentation, those parameters should be optimized to achieve a weighting field that is as uniform as possible. Figure 3.11 exhibits the weighting field along a strip for wide and thin strips. As one can see in Fig. 3.11, in the case of a wide strip,
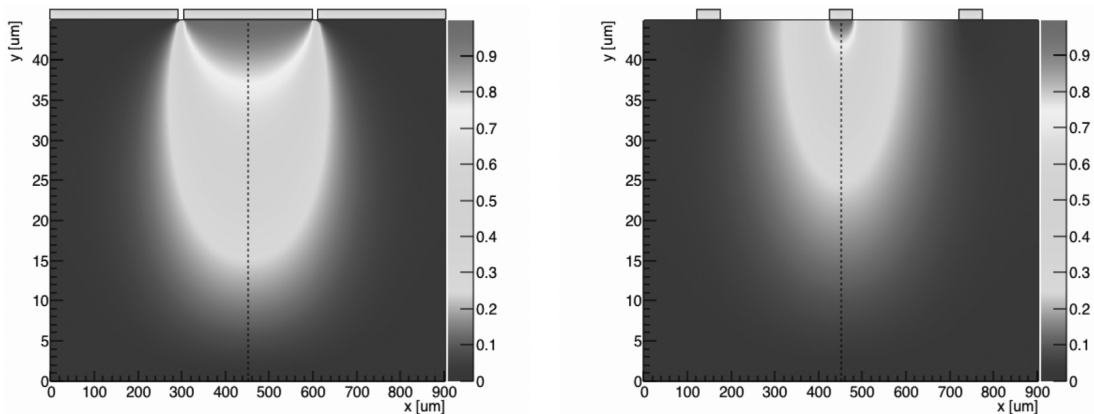

Figure 3.11: Weighting field dependence on a strip width. The left picture represents a wide strip and the right picture represents a narrow strip. Taken from [33].

the weighting field along the strip pitch stays constant. However, for the thin strip, the weighting field is much stronger directly below the strip electrode when compared to the detector volume between the electrodes.

To lower the contribution from the non-saturated drift velocity and non-uniform weighting field effects, the detector geometry should be optimized. It should be as close as possible to a parallel plate capacitor, and the strip width should be similar to the strip pitch and much bigger than the sensor thickness [44].

3.3.5 LGAD design optimization for time measurements

As discussed in [38], an LGAD design optimization is important to achieve the best possible time resolution. According to [38], the maximum current in a detector without gain can be calculated using the Ramo–Shockley's

theorem (Eq. 2.9):

$$I_{max} \propto 75 \cdot d \cdot q \cdot v_{sat} \frac{1}{d} = 75 \cdot q \cdot v_{sat}, \tag{3.3}$$

where d is a detector thickness, $75 \cdot d$ is the induced current, $E_w \propto 1/d$ is the weighting field, and v_{sat} is the drift velocity, which is assumed to be saturated. However, when closely looking at Eq. 3.3, it becomes
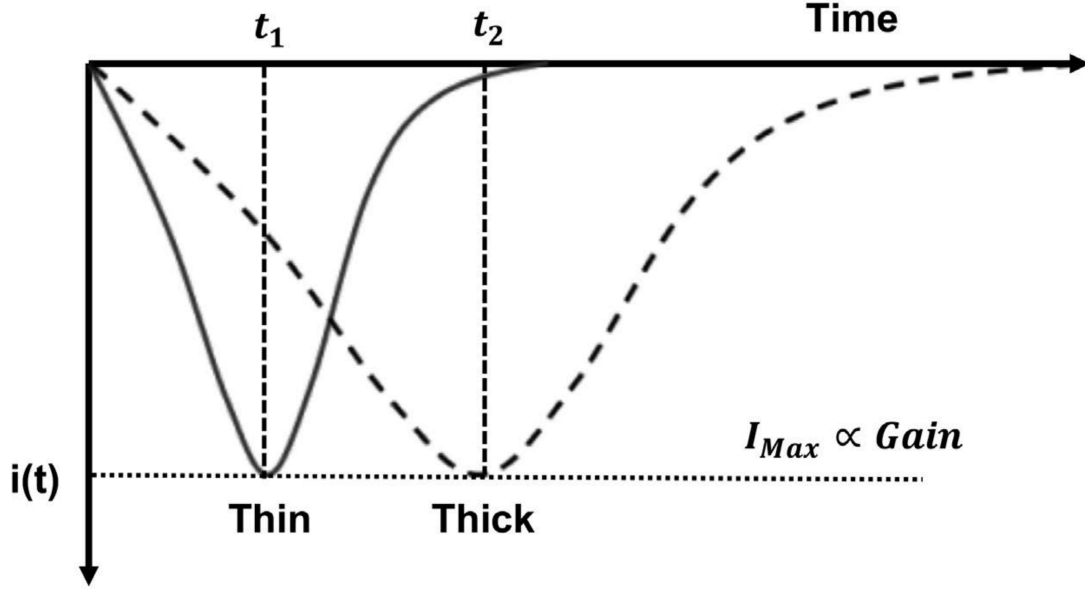
Figure 3.12: LGAD signal in detectors with different thicknesses. Detectors with two different thicknesses and the same gain level have the same signal amplitude but different rise times. Taken from [33].

apparent that the maximum current does not depend on the sensor thickness. For LGADs, on the other hand, the gain G has to be included in Eq. 3.3, which results in the following gain current [38]:

$$dI_{gain} = dN_{gain} \cdot q \cdot v_{sat} \frac{k}{d} \propto \frac{G}{d} dt \tag{3.4}$$

Rearranging Eq. 3.4, one can get an expression for a slew rate, which is defined by the gain G and the detector thickness d only [38]:

$$\frac{dI_{Gain}}{dt} \sim \frac{dV}{dt} \propto \frac{G}{d} \tag{3.5}$$

Equation 3.5 indicates that maximal signal amplitude is defined exclusively by gain while a signal rise time is defined by sensor thickness only. Figure 3.12 exhibits those effects.

To verify Eq. 3.5, simulations for different gain values and detector thicknesses were done [33]. The results of these simulations are shown in Fig. 3.13. It demonstrates an important fact for the LGAD design optimization: low gain values ($\sim$10-20) together with low sensor thicknesses ($\sim$50 μm) allow the best possible time resolution [38].

3.4 Radiation hardness

Primarily, LGADs were developed as upgrades for upcoming experiments with increased luminosity to deal with a higher particle fluence. Besides excellent time and spatial resolution, LGADs should sustain the radiation damage caused by those higher fluxes.
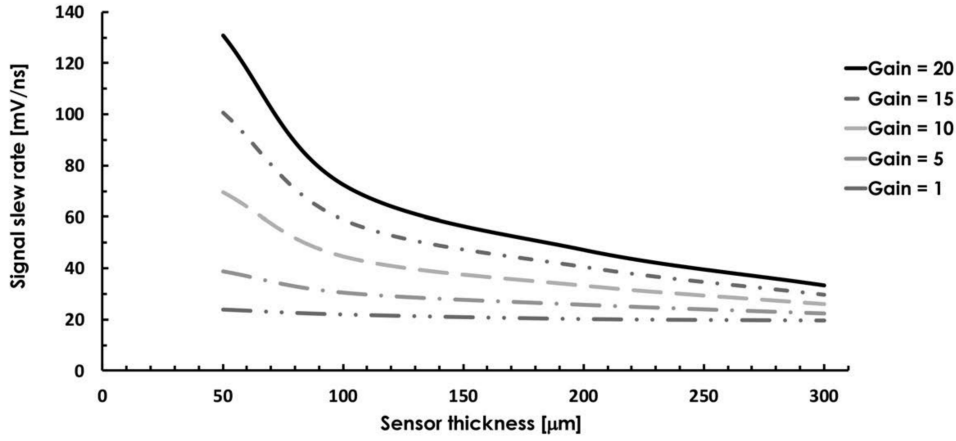
Figure 3.13: Simulated slew rate dependence on gain values and a detector thickness. Taken from [33].

The main effect that comes from irradiation is the so-called acceptor removal. The acceptor removal is defined by changes in the gain layer due to atoms inactivation in this layer [45]. The acceptor removal can be described as follows [33]:

$$N_A(\Phi_{eq}) = N_A(0)exp(-c_A\phi_{eq}) = N_A(0)exp\left(-\frac{\Phi_{eq}}{\Phi_{0eq}}\right),$$

where Φ_{eq} is the irradiation fluence, $N_A(0)$ and $N_A(\Phi_{eq})$ is the initial acceptor density and acceptor density after irradiation, c_A is the acceptor removal coefficient that depends on the initial acceptor concentration and type of irradiation and Φ_{0eq} is the value of fluence that reduces initial acceptor density by a factor of e ($\Phi_{0eq} = 1/c_A$). As the gain layer is crucial for controlling the internal multiplication in the detector, the inactivation of acceptor atoms in this layer directly influences the performance.

A radiation hardness study was done for different LGAD productions, conducted by an external group, presented in [46]. It was shown that the gain decreases with higher irradiation with neutron equivalent fluence up to $6 \cdot 10^{15}$ neq/cm^2. Consequently, the bias voltage should be increased to compensate for this effect and to keep the gain at the same level. This compensation technique, however, only works for relatively low fluence because the maximal value of bias voltage is limited by an electric breakdown in the detector, as discussed earlier in this chapter.

Results from [46] also indicate changes in time resolution after irradiation and exhibit a fluence-dependant degradation of the time resolution with an increase up to $40\,ps$ for the highest fluence of 10^{16} neq/cm^2.

Several irradiation hardness studies of LGADs from different groups [45–47] indicate that LGADs keep the designed timing performance after irradiation with neutron equivalent fluence up to $\sim 10^{15}$ cm^{-2} with slight degradation in performance. Additionally, these studies present potential solutions to further increase the radiation hardness of LGADs.

4 Proof-of-principle test at the S-DALINAC

A timing precision for LGADs below $50\,\text{ps}$ was demonstrated in [7, 48]. This excellent time resolution highlights the potential of LGADs to fulfill the demanding requirements for a beam structure monitoring system at the S-DALINAC in ERL operation mode, as outlined in Sec. 1.2.2. The first proof-of-principle demonstration of the LGAD application for the S-DALINAC beam time structure monitoring was performed utilizing a simplified setup consisting of only one small LGAD ($0.5 \times 1\,\text{cm}^2$) strip sensor, which was only partly read out. The experiment discussed in this chapter was performed at the dedicated detector test area outside of the recirculation beam lines of the S-DALINAC (as shown in Fig. 1.1). However, this meant that only the beam extracted from the S-DALINAC could be measured, which, in contrast to the beams in the recirculation lines, featured a time structure of $3\,\text{GHz}$ instead of $6\,\text{GHz}$ in the ERL mode. Still, measuring the time structure of $3\,\text{GHz}$, corresponding to $\sim 333\,\text{ps}$ between two consecutive bunches, allowed to demonstrate the feasibility of an LGAD-based beam time structure monitoring system for the S-DALINAC, which was the main goal of this experiment.

The analysis of the data presented in this chapter was done using the Go4 [49] and ROOT [30] frameworks. The overview of the results of this experiment was presented at the International Beam Instrumentation Conference (IBIC) 2022 and published in the conference proceedings [50]. However, in this chapter, a detailed analysis and discussion are given.

4.1 Proof-of-principle demonstration setup

4.1.1 LGAD sensor parameters

A simplified setup was prepared based on a single multi-strip LGAD sensor for the first proof-of-principle measurement. This sensor was produced by Fundazione Bruno Kessler (FBK, Italy) with a size of $0.5 \times 1\,\text{cm}^2$, $200\,\text{μm}$ total thickness and $50\,\text{μm}$ pitch. The bias voltage to the sensor was set to $230\,\text{V}$. Figure 4.1 exhibits the sensor used in this experiment, bounded to a printed circuit board (PCB). The PCB contains two stages of amplification close to the sensor. The amplifiers were operated at $1.4\,\text{V}$ with $825\,\text{mA}$.

Figure 4.1: Photo of the LGAD sensor mounted on the PCB, used in the first proof-of-principle test at the S-DALINAC. Taken from [50].

4.1.2 Readout system

Signals from the sensor were read out by the PaDiWa [51] leading-edge discrimination board, which is capable of processing up to 32 channels. The PaDiWa board is connected to the so-called TRB3 platform which contains a field programmable gate array (FPGA) based TDC [52]. Figure 4.2 shows the full experimental setup. Due to the bonding scheme of the sensor to the PCB, only every second channel of the sensor was
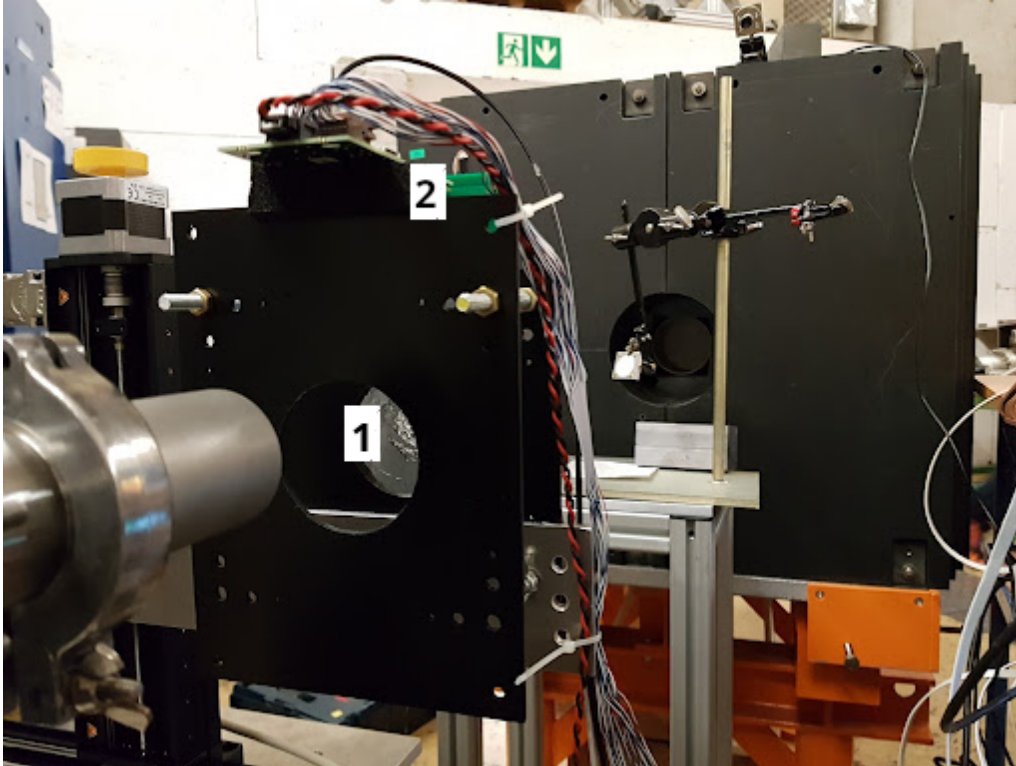

Figure 4.2: Photo of the experimental setup for the first proof-of-principle test at the S-DALINAC. The LGAD sensor is marked as (1) and the PaDiWa board is marked as (2). Taken from [50].

connected to the readout electronics. As a result, only eight channels were connected and actively read out during the experiment. The trigger was set to the channel 2 of the sensor. For each trigger particle, which was used as a reference for a time measurement, all hits and their ToA and ToT were recorded in all connected channels within a predefined trigger window. The trigger window was set to $150\,\mathrm{ns}$ with $100\,\mathrm{ns}$ collected before the trigger event and $50\,\mathrm{ns}$ after. All observed hits in this trigger window were regarded as one event, and for each of those hits in this event, the ToA and ToT were recorded as mentioned in Sec. 3.2.2.

The experiment was conducted in October 2021 utilizing a $85\,\mathrm{MeV}$ electron beam with $3\,\mathrm{GHz}$ time structure.

4.2 Data analysis

During the experiment, the ToA and ToT of the electrons passing through the LGAD sensor were measured. The corresponding raw ToT spectrum is shown in Fig. 4.3. In this figure and all other two-dimensional plots in this thesis, the Z-axis represents the number of entries in linear scale if not mentioned otherwise. Since channel 2 was selected as a trigger, it also showed much higher rates than others. As mentioned before, only half of the read-out channels (even numbers from 2 to 16) were connected to the sensor. This also becomes

apparent when looking at Fig. 4.3, where a small amount of low ToT signals in channels with odd numbers can be observed, representing noise and corresponding to the TDC channels, which were not connected to the sensor.

Channel 2 in Fig. 4.3 exhibits a signal at $\sim 6\,\mathrm{ns}$, which originates from electrons passing the sensor. The same signal is visible in other channels with even numbers but at much lower rates. Additionally, the low ToT signals about $2\,\mathrm{ns}$ are exhibited in channels 1 and 3 which corresponds to noise. Channels 14 and 16 have failed and were excluded from further analysis.
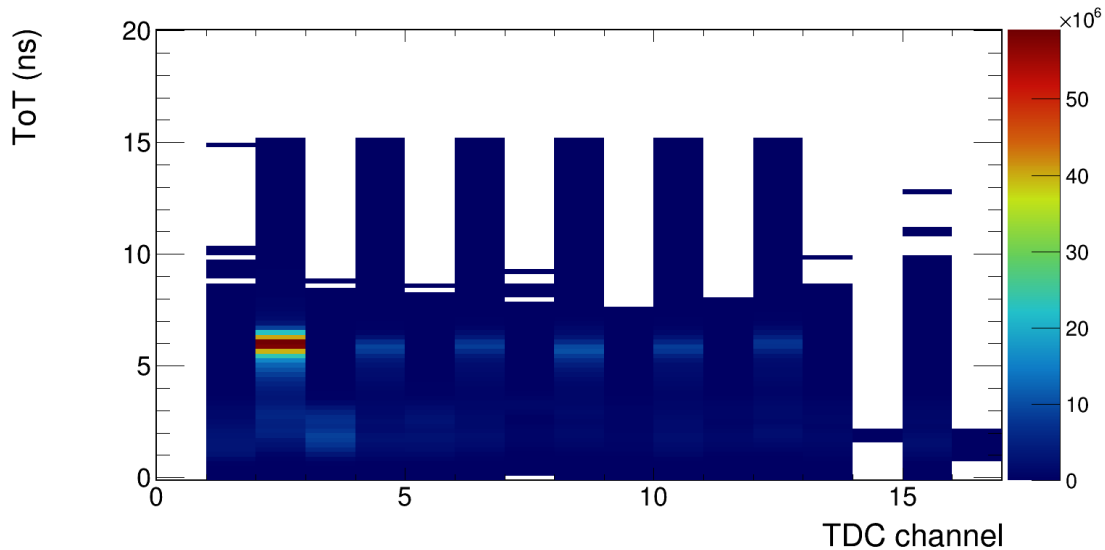
Figure 4.3: The raw ToT spectrum in the proof-of-principle experiment at the S-DALINAC. Channel 2 is the trigger channel, and for this reason, it has a much higher signal rate than the other channels. Each even channel shows the signal at $6\,\mathrm{ns}$, which originates from electrons hitting the detector, while each odd channel contains only noise.

4.2.1 Time walk correction

To resolve the beam time structure the time difference between two hits in the LGAD was calculated. Since the beam in this experiment had a $3\,\mathrm{GHz}$ time structure, which corresponds to $333\,\mathrm{ps}$ between the bunches, this time structure was expected to be also reflected in the aforementioned measured time difference. However, since the signal path is different for different channels in the detector, the measurement will deteriorate if one calculates the time difference between hits in two different channels. Consequently, only the time difference between hits in the same channel were calculated, which, however, required more than one hit in the same channel per recorded event. The number of hits in each channel (also called multiplicity) per event is exhibited in Fig. 4.4. As for the time walk correction, only events with a multiplicity of two or more are required to calculate the time difference between hits in the same channel. This data is shown in Fig. 4.4b.

As was discussed in Sec. 3.3.2, the time walk effect has a significant impact on the timing performance of detectors that employ leading-edge discriminators, and it is therefore necessary to compensate for this effect. To perform the time walk correction, two-dimensional histograms showing a difference between the ToA of two hits inside channel 2 as a function of a ToT for both hits were created. Channel 2 was selected for the time walk correction due to fact that there are much more events with high multiplicity (multiplicity 2 or more), as shown in Fig. 4.4b.
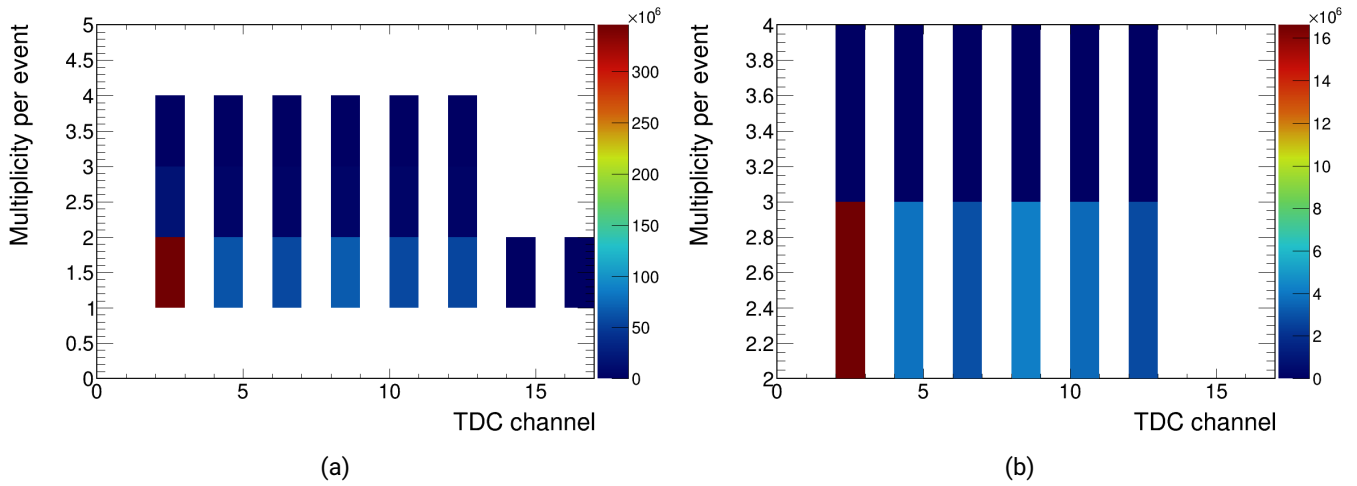
Figure 4.4: Multiplicity per channel per event during the proof-of-principle experiment: (a) shows full multiplicity per channel, (b) shows the multiplicity greater than one per channel.

The time difference is calculated as follows: time difference $= ToA_{\text{correlated hit}} - ToA_{\text{reference hit}}$, where the hit that arrives earlier is used as a reference and is called a reference hit, while the other hits are called correlated. The outcome of this step is shown in Fig. 4.5. The same data in the smaller time difference and
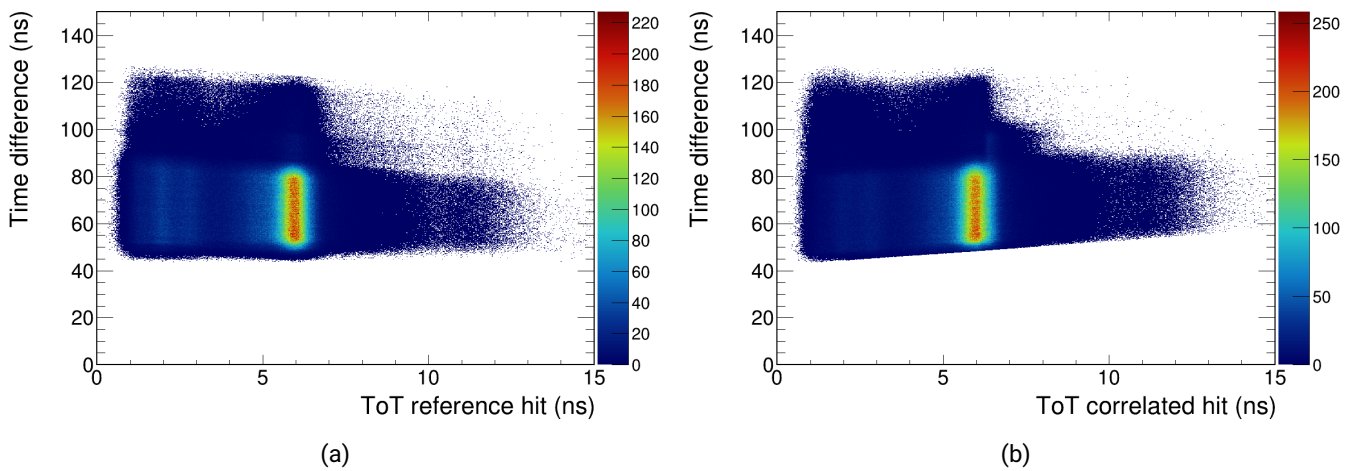
Figure 4.5: Time difference between two hits inside channel two as a function of ToT: (a) shows the time difference between reference and correlated hits as a function of the ToT of the reference hit, (b) shows the same time difference as a function of the ToT of the correlated hit. No data below $50\,\text{ns}$ on the time difference axis represent a dead time of the system.

ToT range for both reference and correlated hits are shown in Fig. 4.6. As one can see in Fig. 4.6, neither the time walk effect nor the time structure is visible. However, before performing the time walk correction, additional ToT cuts ($100\,\text{ps}$ in the ToT range) were applied to the signals of the correlated hits. This ensured that a correlated signal originates from an electron passing through the sensor, which consequently reduces the amount of data in the reference hit spectrum due to exclusion of the noise and capacitive coupling signals.

For this anaylsis, a ToT cut from $5.9\,\text{ns}$ to $6\,\text{ns}$ was applied on the ToT of the signals of the correlated hits as
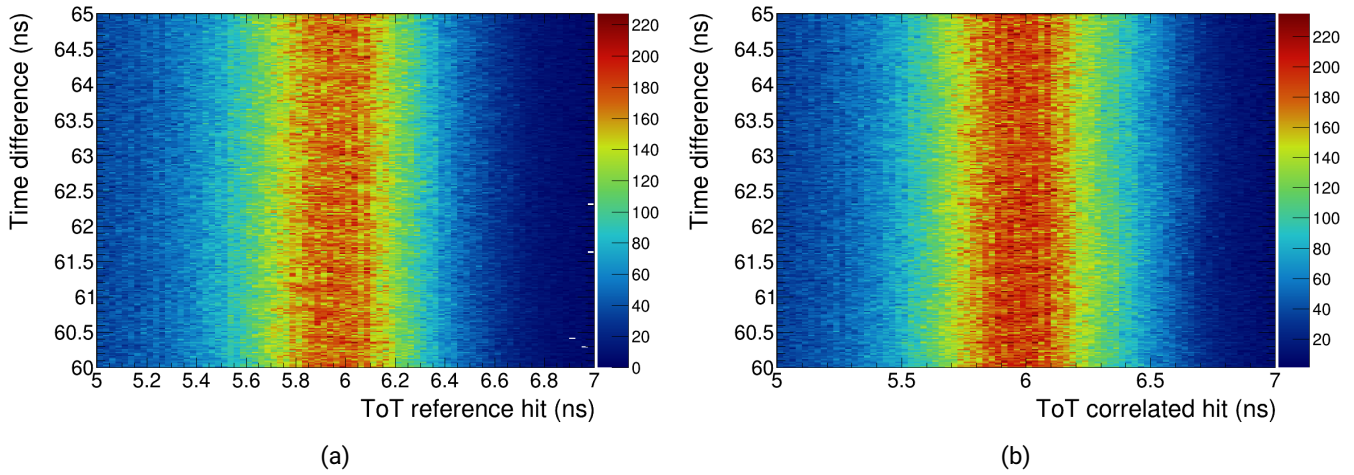
Figure 4.6: Time difference between two hits inside channel two as a function of ToT in small time difference and ToT range: (a) shows the time difference between reference and correlated hits as a function of the ToT of the reference hit, (b) shows the same time difference as a function of the correlated hit. The full dataset is shown in Fig. 4.5.

shown in Fig. 4.7b. An additional cut on the reference signal is not required for the time walk correction as the goal of the correction is to remove the time difference dependence on the ToT of the signal in the full signal range. The outcome of applying a ToT cut on the correlated signal is shown in Fig. 4.7. After the narrow ToT cut application, a periodic time structure with a time walk trend becomes clearly visible (Fig. 4.7a).

For the calculation of time walk correction parameters, one of the peaks visible in the spectrum after the
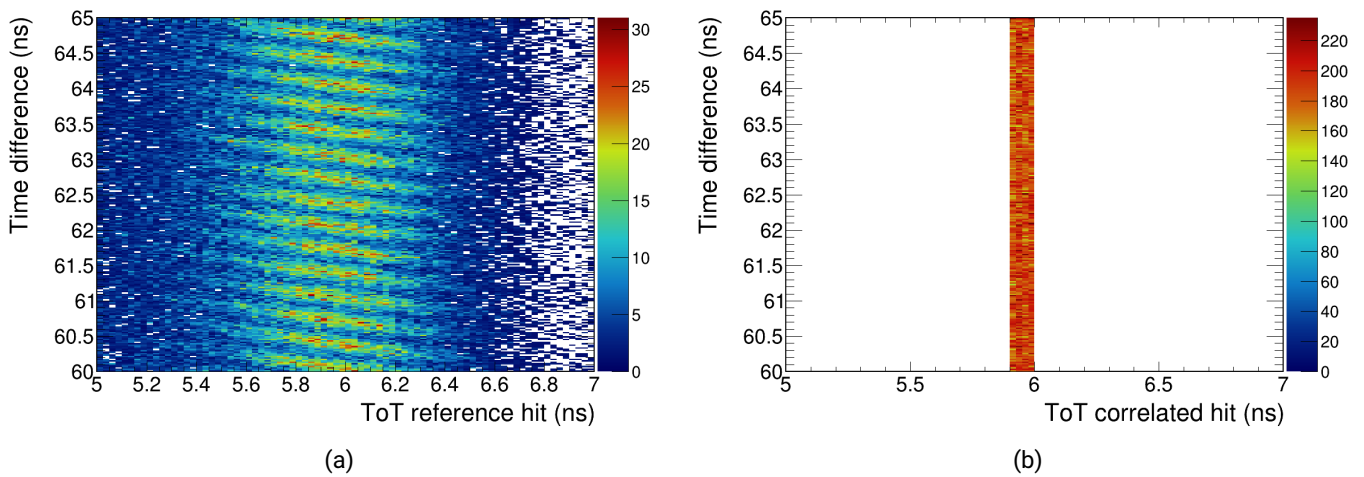

Figure 4.7: Time difference between two hits inside channel two as a function of ToT with applied $100\,\mathrm{ps}$ ToT cut on correlated hit: (a) shows the time difference between reference and correlated hits as a function of the ToT of the reference hit, (b) shows the same time difference as a function of the ToT of the correlated hit. The same data without the ToT cut on the correlated hit is presented in Fig. 4.6.
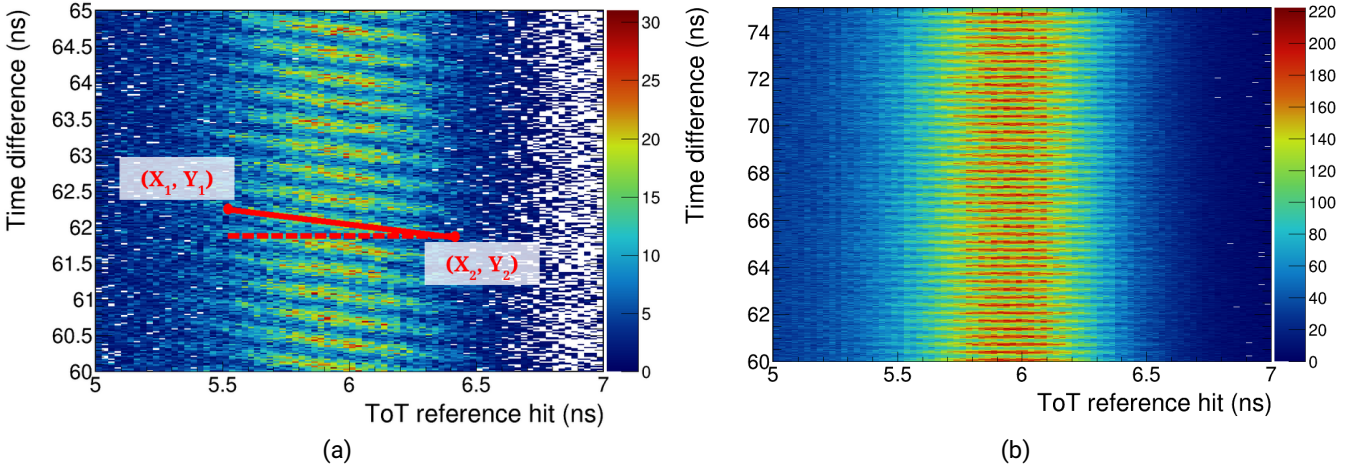
Figure 4.8: The time walk correction parameters calculation scheme and correction result in small ToT and time difference range. (a) A strong time difference dependence on the signal ToT is visible. The red solid line represents the line used to determine time walk correction parameters with respect to the red dashed line. (X_1, Y_1) and (X_2, Y_2) marked with red dots and represents the data points used for the time walk parameters calculation. (b) The result of the time walk correction for channel number two without the narrow cut on correlated hit ToT.

ToT cut application was used. Since the previously mention time walk trend in the time difference structure is linear, a linear function was used to calculate the time walk trend (represented by the solid red line in Fig. 4.8a). This line can be represented as follows:

$$\begin{cases} y_1 = ax_1 + b \\ y_2 = ax_2 + b \end{cases} \tag{4.1}$$

where (x_1, y_1) and (x_2, y_2) are the coordinates of the most left and right points of the line, respectively, with a and b representing the parameters of a linear function, which were determined for the time walk correction. While the x-coordinate represents the ToT value, the y-coordinate represents the time difference value.

To obtain the (x_1, y_1) and (x_2, y_2) data points, a line was drawn manually to approximate one of the peaks in the Fig. 4.7a in the ToT region of interest as shown in Fig. 4.8a. The upmost left and right points of this line were used to calculate the correction parameters. The manual procedure was chosen over developing an automatic one since the peaks are too close to each other, and, for a fixed time difference range, avoid any outliers from the neighbouring peaks as this could deteriorate the outcome of the parameter estimation procedure.

To remove the time difference dependence on the ToT, all time difference values were shifted to the same one to remove the time difference dependence on the signal ToT. y_2 was chosen as the corresponding value, which is represented by the red dashed line in Fig. 4.8a. After this step, Eq. 4.1 can be rewritten as follows:

$$\begin{cases} y_1 - y_2 = ax_1 + b \\ 0 = ax_2 + b \end{cases} \tag{4.2}$$

After rearranging Eq. 4.2 one can calculate the correction parameters:

$$\begin{cases} a = \dfrac{y_1 - y_2}{x_1 - x_2} \\ b = -ax_2 = -\dfrac{y_1 - y_2}{x_1 - x_2}x_2 \end{cases} \qquad (4.3)$$

To correct for the time walk effect, the correction parameters apply to the ToA of all hits as follows:

$$ToA_{corrected} = ToA_{raw} - (a * ToT + b),$$

where the parameters a and b are defined by Eq. 4.3 and ToA_{raw} is the raw recorded ToA. Figure 4.8b exhibits the result of the time walk correction. After the time walk correction, the periodic structure in the main signal region becomes visible, which is expected to represent the beam time structure.

4.2.2 Peak identification

To investigate this periodical structure further and prove that it indeed represents the beam time structure, an identification of the peaks is needed. For this, a projection of the time walk corrected data, shown in Fig. 4.8b, was performed on the time difference axis in the full time difference range. An additional ToT cut ($4\,\text{ns} <$ ToT $< 8\,\text{ns}$) was introduced to exclude signals that originate from capacitive coupling and to only analyze the signals that stem from electrons passing through the LGAD. Figure 4.9 shows the outcome of this step. The region below $50\,\text{ns}$ in Fig. 4.9a shows no data, which is due to the dead time of the system.
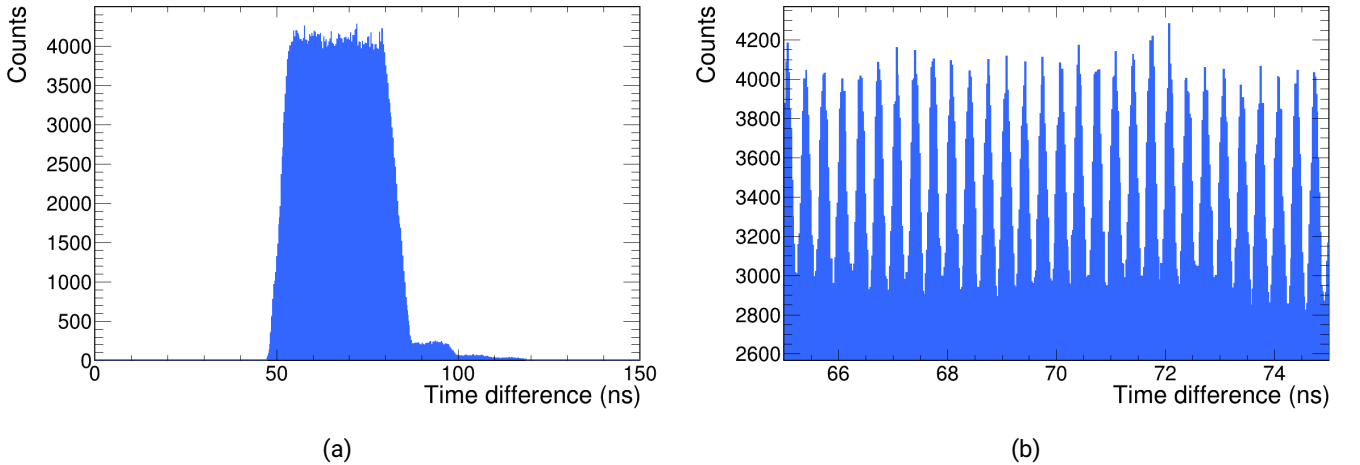

(a)

(b)

Figure 4.9: Projection of the time difference axis of the time walk corrected data from channel two in different time difference ranges. (a) shows the full time difference range, and (b) is zoomed in to a $10\,\text{ns}$ range time difference wide interval.

As shown in Fig. 4.9a, the peak amplitude stays constant with small fluctuations in the time difference range from $50\,\text{ns}$ to $85\,\text{ns}$ and then drastically decreases towards higher time difference values. Additionally, Fig. 4.9b shows that the peak amplitude above the present background in the spectrum is approximately 1/3 of the absolute height.

For the peak identification, a TSpectrum [53] class was used from the ROOT analysis framework, which is an advanced tool for spectrum analysis and includes the peaks identification procedure. It has to be noted

that in the scope of this work, the TSpectrum class functionality was used exclusively for the determination of the peak position.

As one of the parameters for the peaks finder function of the TSpectrum class is the peak amplitude, the time difference spectrum was split into smaller ranges with a time difference range of $10\,\mathrm{ns}$ to maximize the number of identified peaks in the high time difference region, which, consequently, increases the precision of the beam time structure determination. The function *SearchHighRes* from the TSpectrum class was used for the peak identification. In the first step, the biggest peak in the given range was identified. For other peaks to be considered the following condition should be met [54]:

$$A_{pc} - \frac{A_{pc-3sigma} + A_{pc+3sigma}}{2} > \text{threshold}/100 * A_{hp}, \tag{4.4}$$

where A_{pc} is a peak candidate amplitude at the peak center, $A_{pc-3sigma}$ and $A_{pc+3sigma}$ is the amplitude at symmetrical channels $\pm 3sigma$ from the peak center, A_{hp} is the highest peak amplitude, and sigma and threshold are the user-defined parameters.

The graphical representation of the peak identification procedure is shown in Fig. 4.10. One can see three
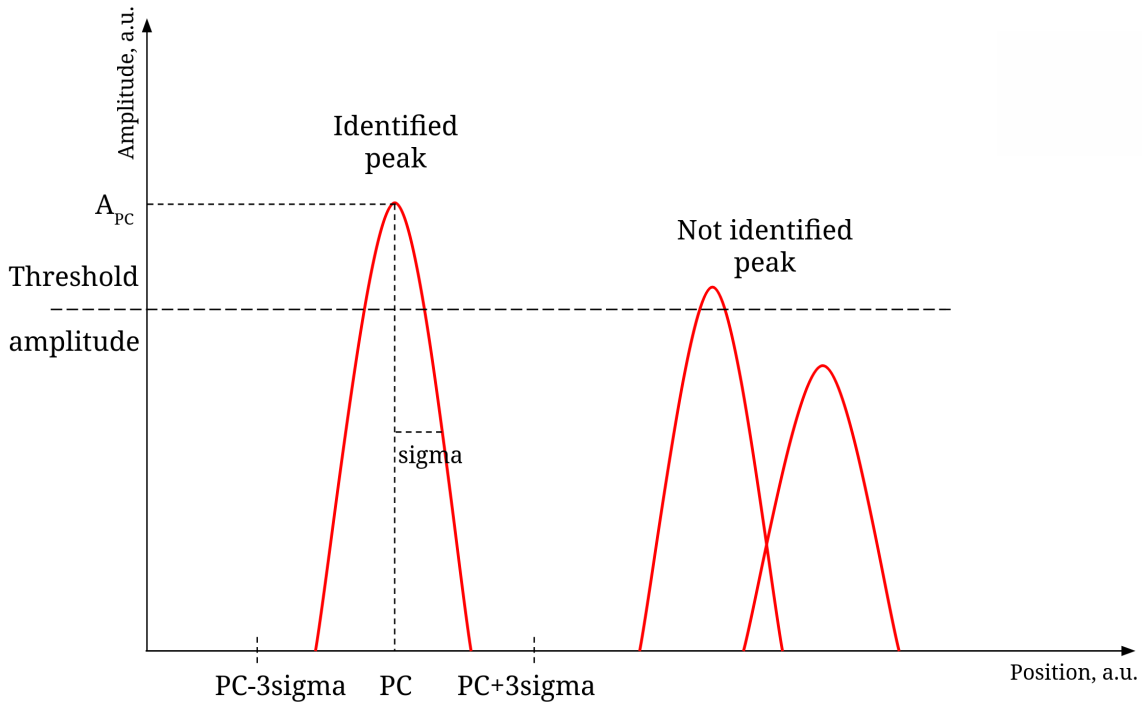

Figure 4.10: TSpectrum peak searching procedure scheme. PC represents the position of the peak candidate position, A_{pc} is a peak amplitude. Sigma and threshold amplitude represent the user-defined parameters of the peak identification algorithm.

peaks in the spectrum. The highest peak amplitude (which is the amplitude of the first peak) in the given spectrum is used as a reference. Based on the highest peak amplitude, the threshold amplitude value is calculated using the user-defined threshold value. As one can see, the third peak amplitude is below the threshold, and consequently, this peak will not be identified by the algorithm. On the other hand, since the second peak amplitude is above the threshold, it will be considered as a candidate by the search algorithm. In the next step, the criteria defined by Eq. 4.4 is checked. For the candidate peak, its amplitude is compared with amplitude at peak center positions $\pm\,3\times$width of the distribution. If the noise level is too high or another

peak is located too close to the peak candidate, the candidate will not satisfy Eq. 4.4 and will be rejected. It has to be noted that this step is sensitive to the width of the distribution, which is defined by the user. Setting this value too high will lead to the rejection of two closely located peaks, while the too low value will lead to misidentification. In the given example, the second peak was rejected due to the location of the third peak, leading to only the first peak being identified.

Table 4.1 summarises the parameters used in *SearchHighRes* function. The parameters were optimized

Parameter	Value
Sigma	3
Threshold	70 (%)
Background removal	false
Deconvolution iterations	10
Markov chain method	false

Table 4.1: Parameters for the TSpectrum peak search function.

empirically to achieve the best possible performance of peak identification. As a result of this step, a list of peaks was obtained with the bin numbers corresponding to peak position and peak amplitude Y_i (marked as a PC and A_{PC} in Fig. 4.10). A bin number was used to obtain a bin center position X_i and used in the further analysis step.

In the next step, the identified peaks that satisfied Eq. 4.4 were fitted with a function consisting of a sum of Gaussian and a constant offset value B:

$$f(x) = [\text{Constant}] \times exp\left(-0.5 \times \left(\frac{x - [\text{Mean}]}{[\text{Sigma}]}\right)^2\right) + B, \tag{4.5}$$

where [Constant], [Mean], and [Sigma] are the fit parameters for the Gaussian function and B is the constant offset for simple background estimation. The initial fit parameters alongside the parameters limit are summarised in Tab. 4.2. However, it has to be mentioned the fit was done in the range $X_i \pm 0.15$ rather

Parameter	Initial value	Parameter limits	
		Minimum	Maximum
Constant	100	100	$0.4 \times Y_i$
Mean	X_i	X_i - 0.15	X_i + 0.15
Sigma	0.01	0.02	1
Background	100	100	$0.9 \times Y_i$

Table 4.2: Fit parameters initial values and limits for peak fitting procedure.

than putting an actual limit on the peak position. The outcome of the peak identification procedure for two small time difference sub-ranges is shown in Fig. 4.11. As one can see in Fig. 4.11a, the six first peaks were not identified because of their low amplitude and, consequently, did not satisfy the condition in Eq. 4.4. Another effect is introduced by dividing the time difference into smaller sub-ranges. As one can see in both Fig. 4.11a and Fig. 4.11b, the last identified peak in both sub-ranges is not a full peak but rather a small part of the next. However, it satisfies the condition in Eq. 4.4 and was used in the further analysis. This effect emerges from splitting the full time difference range into smaller ones and can be removed by refraining from
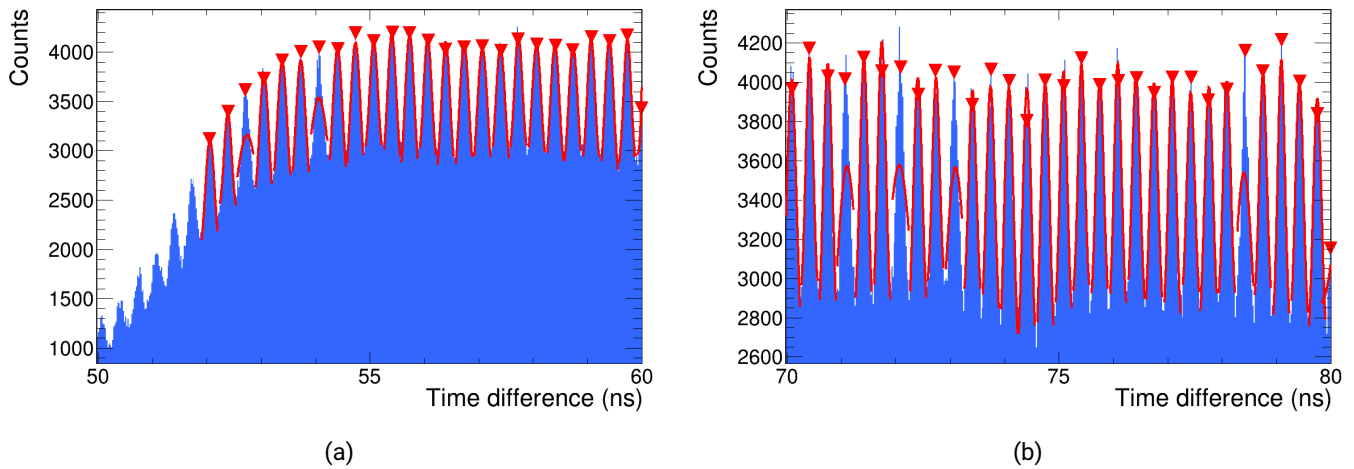
Figure 4.11: The result of peak identification procedure for two small time difference ranges: (a) shows the time difference range from $50\,\text{ns}$ to $60\,\text{ns}$ and (b) shown the time difference range from $70\,\text{ns}$ to $80\,\text{ns}$. Red triangles represent the identified peaks' position and amplitude according to the peak identification algorithm and red solid lines show the fit function for each identified peak defined by Eq. 4.5.

doing so. However, these false identified peaks do not follow the $3\,\text{GHz}$ time structure and can be identified and separated from the true peaks. Consequently, without splitting the time difference range into smaller sub-ranges the efficiency of the beam time structure identification would decrease as a smaller number of true peaks that represent the beam time structure would be identified.

4.2.3 Final result

As a final step in the analysis, the time difference between two consecutive identified peaks was calculated (shown in Fig. 4.12) and the resulting one-dimensional histogram was fitted with the Gaussian function to obtain the mean time difference between recorded hits in the detector. The result of the final analysis step is shown in Fig. 4.12. The mean time difference between two consecutive peaks is $(333.4 \pm 0.3)\,\text{ps}$, which corresponds to the $3\,\text{GHz}$ time structure of the S-DALINAC. This indicates that the time structure of the S-DALINAC electrons beam was successfully resolved in the standard operation mode.

One could see in Fig. 4.12 entries near the main peak. Those entries can be explained by two effects. As discussed, the full time difference range was divided into smaller sub-ranges to obtain a more robust result in the peak searching procedure. Some peaks were split into two parts that belong to two different ranges. Consequently, two peaks were identified instead of one with a smaller distance between them. On the other hand, not all peaks were fitted properly. The fit function parameters' initial values and limits were optimized to increase the fitting procedure performance. However, some peak fits still were not optimal. For example, one can refer to peak numbers four, seven, and ten in Fig. 4.11b. As one can see, these fits do not represent the shape of the peak, but its position is correct. Failure to properly fit a peak led to a slight shift in peak mean position and, consequently, introduced some discrepancy. This effect is exhibited in Fig. 4.12 by small spikes in the time difference around $310\,\text{ps}$ and $355\,\text{ps}$.
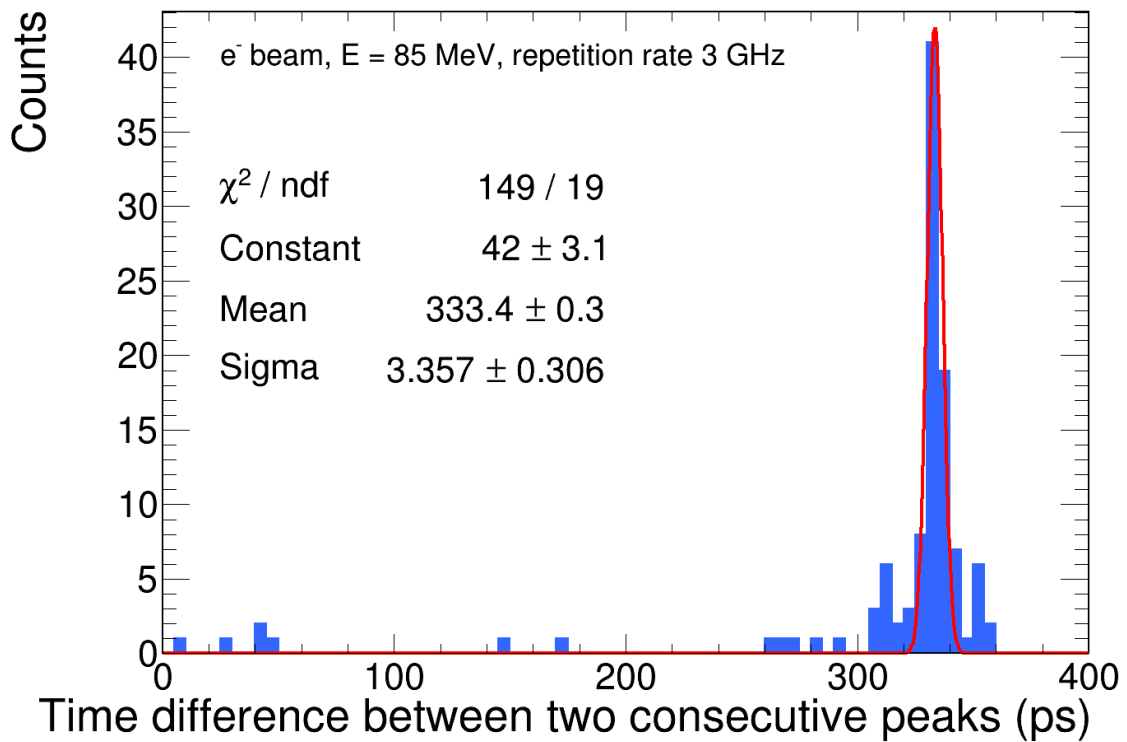
Figure 4.12: The time difference between two consecutive identified peaks and corresponding Gaussian fit (red solid line) with fit parameters.

4.3 Summary

For the first time, the beam time structure of the S-DALINAC was successfully resolved using a simplified setup consisting of only one LGAD strip sensor. The results demonstrate the feasibility of an LGAD-based setup application for beam time structure monitoring at the S-DALINAC. So far, this setup cannot be used as a monitoring tool itself due to the usage of a single LGAD sensor, which results in a small number of active channels in the system. In the next chapter, the performance of the full system, consisting of two LGAD sensors, will be discussed.

5 Performance test of an LGAD-based beam monitoring system

A performance test of an LGAD-based beam monitoring system was done after successfully demonstrating the proof-of-concept with a single simplified LGAD detector prototype (see Chapter 4). Compared to the proof-of-principle experiment described in Chapter 4, the setup in this study consisted of two instead of one sensor, which were also larger in size and fully read out. As for the previous test, the experiment was performed at the dedicated test area of the S-DALINAC. Hence, the experiment also aimed to resolve $3\,\mathrm{GHz}$ time structure and demonstrate the full system performance.

5.1 Experimental setup

An upgraded version of the setup presented in Chapter 4 was prepared for this experiment. As shown in Fig. 5.1, the experimental setup consisted of four LGAD sensors because this system was also used in an experiment at MedAustron (Wiener Neustadt, Austria) as a time-of-flight (ToF) based ion imaging system [55], which also required particle tracking, and therefore a position and direction measurement with multiple LGAD planes. In this work, the focus is put on the first two sensors for the beam monitoring purposes. Sensor number two ("LGAD 2" in Fig. 5.1) was rotated by $90°$ with respect to sensor number one ("LGAD 1" in Fig. 5.1), allowing an online measurement of the two-dimensional beam position on the sensors during the experiment. Each sensor was $200\,\mathrm{\mu m}$ thick, had an area of $1{\times}1$ cm^2 and featured 86 strips with a pitch of
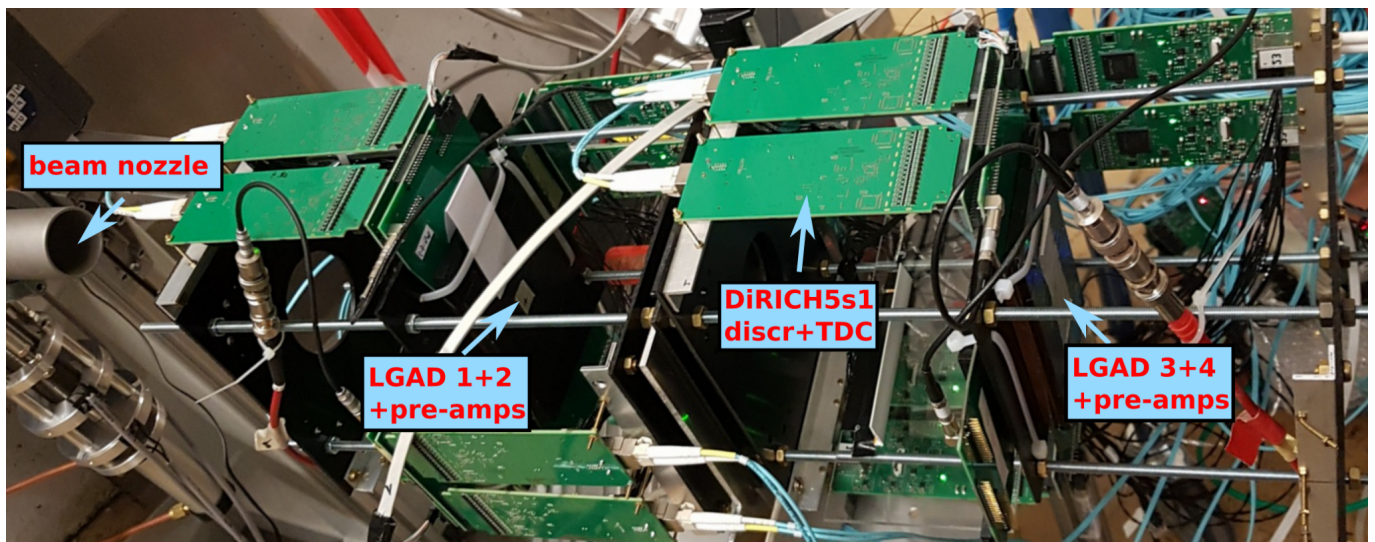
Figure 5.1: Photo of the experimental setup for the full system experiment at the S-DALINAC. Two pairs of LGADs are marked as "LGAD 1+2" and "LGAD 3+4". The "LGAD 1+2" pair was used in the experiment. Read out boards for "LGAD 3+4" sensors marked as "DiRICH5s1 discr+TDC" [56].

100 μm. The LGADs were mounted to the same PCB as described in Chapter 4, which, as previously mentioned, accommodated a larger sensor. The PaDiWa board was replaced with the so-called DiRICH5s1 board, which allows amplification, discrimination, and digitization of signals with a built-in TDC [51] and features 32 read-out channels. However, due to the bonding scheme, four of those DiRICH5s1 boards had to be used per sensor using up to 24 active channels per board. In contrast to the setup presented in Chapter 4 where the digitization of the signals was done via TDCs on the TRB3, the digitization was done directly via the DiRICH5s1, as it also features an on-board discriminator and FPGA-based TDC. Consequently, the TRB3 was used for trigger and data acquisition purposes only.

The second sensor was set as a trigger with a 150 ns trigger window, corresponding to 100 ns before and 50 ns after the trigger event was recorded in the whole system. All recorded hits and their respective ToA and ToT within the single trigger window will be referred to as an event.

The bias voltage for both sensors was set to 250 V with amplifiers on the PCB running at 700 mA. The experiment was performed in November 2022 utilizing a 65 MeV electron beam with a 3 GHz time structure.

5.2 Data analysis

As described in Chapter 4, the ToA and ToT of electrons passing through both LGADs were measured. The measured ToT of the eight connected DiRICH5s1 boards is shown in Fig. 5.2 (further referred to as TDC 1 - TDC 8). While the first four TDCs (TDC 1 - TDC 4) were connected to the first sensor, the last four TDCs (TDC 5 - TDC 8) were connected to the second LGAD, which was also used for triggering purposes.

5.2.1 Normalization of the time over threshold

In Fig. 5.2b, one can see that the MPV of the ToT varied between the individual TDCs and also between the individual channels on a single TDC, which comes from the following effects. First, two different versions of the DiRICH5s1 were used during the experiment, namely original and modified. The modified DiRICH5s1 board featured an adapted electric circuit with respect to the original, unmodified boards, to test different
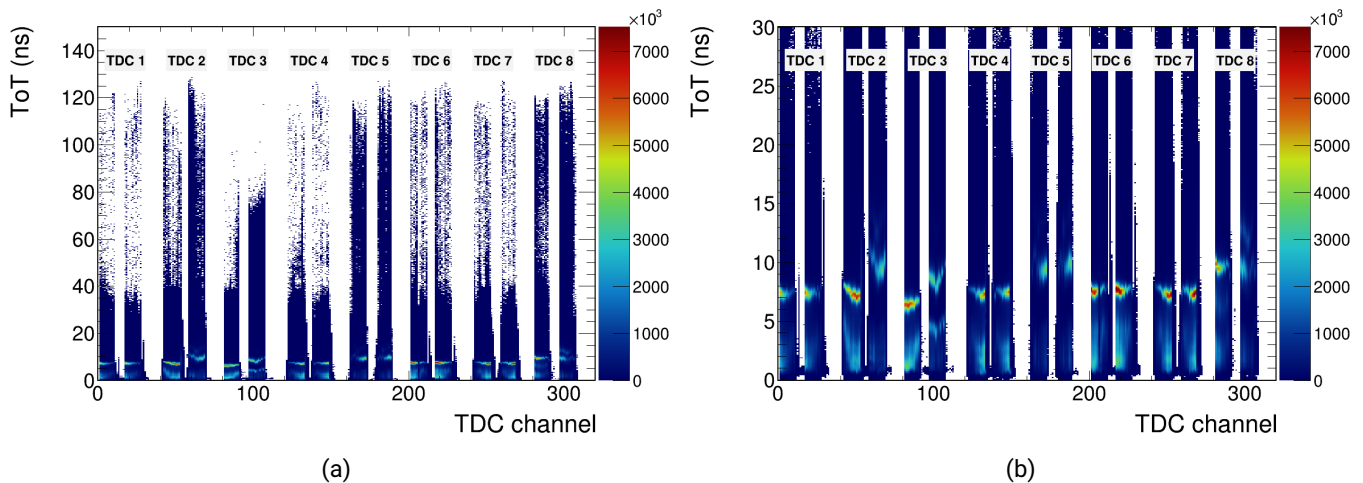

Figure 5.2: The raw ToT spectra per channel in full system test at the S-DALINAC. A total of eight DiRICH5s1 (marked as TDC) was used. (a) represent the full range of ToT, (b) show the small range zoomed for better signal demonstration.

configurations of the pre-amplification and signal shaping scheme. The evaluation of the performance of the modified boards is discussed in details in the master's thesis by Y. Kozymka [57]. Four TDCs in total, i.e. TDCs number two, three, five, and eight, were modified. The second effect, which lead to different ToT values between the TDCs is due to a slight variation in the amplification per TDC. Also, the threshold levels were not the same for different channels due to the channel-dependent noise and variance of the amplification. To compensate for these effects, a ToT normalization was performed.

For this purpose, a projection on the ToT axis was performed for each channel. With this step, a ToT distribution per channel was obtained. As in Sec. 4.2.2, the TSpectrum functionality was used for the peak identification in the ToT spectrum. In this case, a *Search* function was used with the sigma parameter of this function set to 1 and a peak amplitude threshold value of 0.9. The highest peak in a spectrum was assumed to originate from the electrons passing through the sensor. The low ToT part of the signal originates from the noise in the system and capacitive coupling as discussed in [7, 58]. After that, a Gaussian was fitted to the peak in the spectrum within a $\pm 2\,\mathrm{ns}$ time difference window from the identified peak position. The outcome of the fitting procedure is exhibited in Fig. 5.3. The mean value of the fit was used to calculate the
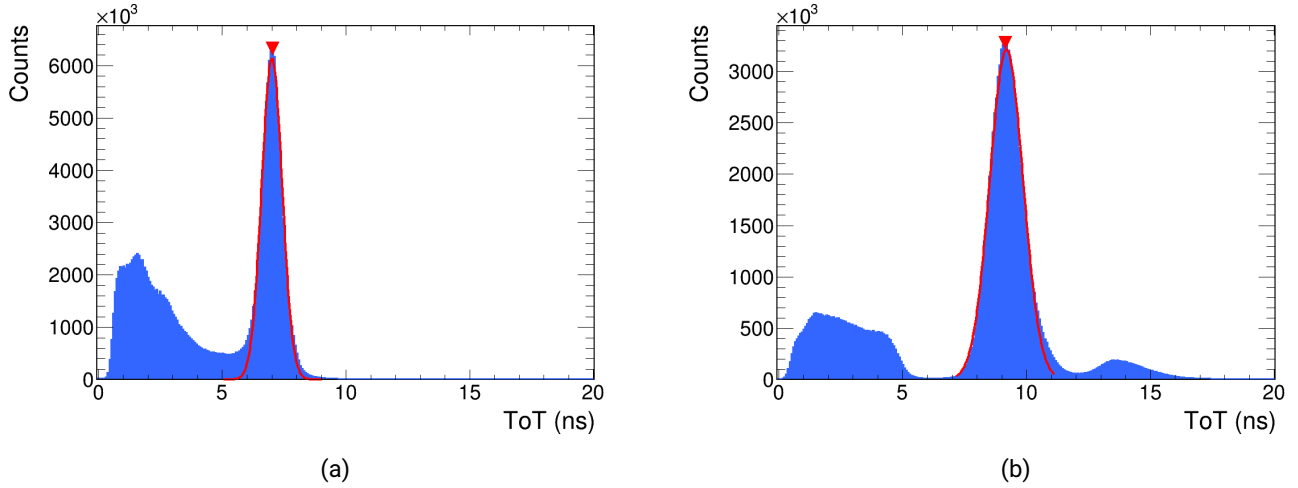
Figure 5.3: The raw ToT spectrum for two different channels in the system and fits for the ToT normalization. The red triangle represents the peak position, which will be normalized, and a red solid line represents the Gaussian fit of this peak.

normalization parameter N as follows:

$$N = \frac{20\,\mathrm{ns}}{\mathrm{mean}},\qquad(5.1)$$

where $20\,\mathrm{ns}$ was selected as the normalization value. After that, a new normalized ToT value was calculated on an event-by-event basis as follows:

$$\mathrm{ToT}_{normalized} = \mathrm{ToT}_0 * N,$$

where ToT_0 is the raw collected ToT and N is the scaling parameter as defined by Eq. 5.1. The normalized ToT spectrum is shown in Fig. 5.4. As one can see, the ToT in all channels in the system is on the same reference value of $20\,\mathrm{ns}$.

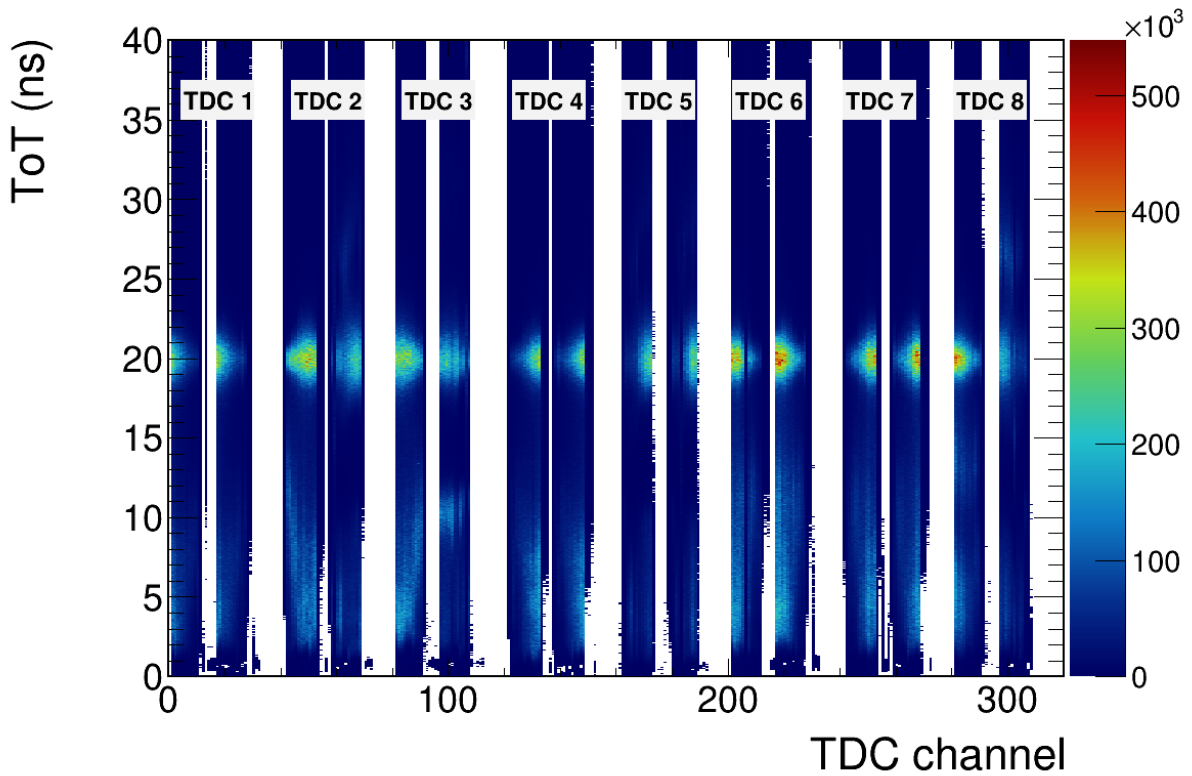Figure 5.4: The normalized ToT spectrum.

5.2.2 Time walk correction

As demonstrated in Sec. 4.2.1, the time walk correction had a significant impact on the LGAD's beam structure monitoring performance at the S-DALINAC. However, a different approach for the time walk correction was used in this analysis compared to the one presented in Sec. 4.2.1. As two sensors were used during the experiments, it was possible to calculate the difference in ToA of the same particle in both sensors. The correlation between signals in both sensors is schematically shown in Fig. 5.5. As one can see, the signals that
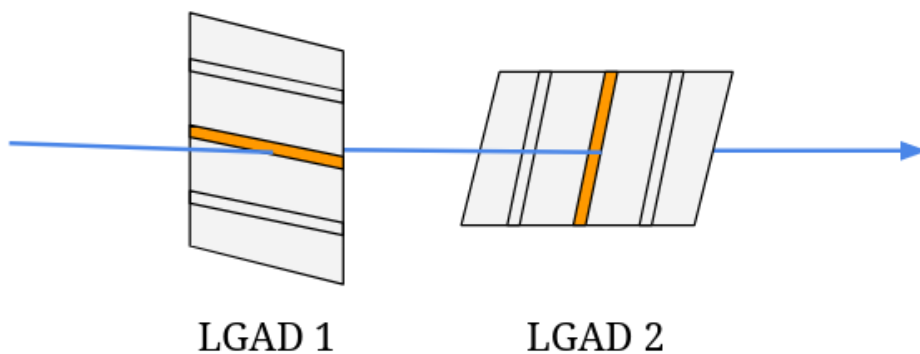
Figure 5.5: The correlation scheme between signals for the time walk correction for a given channel pair. The blue arrow represents the incident particle and the activated channels in both sensors are represented by the orange color.

originates from the same particles passed through both sensors is required.

For the time walk correction, a set of two-dimensional histograms was created. First, two reference channels were selected in both sensors and then the ToAs difference was calculated between all channels ($ToA_{\text{correlated hit}}$) in sensor one and the reference channel ($ToA_{\text{reference hit}}$) in sensor two. The exact time difference was calculated for all channels in sensor two with respect to reference channels in sensor one. It has to be noted that the time difference was calculated as $ToA_{\text{reference hit}} - ToA_{\text{correlated hit}}$ and two different histograms were produced showing the given time difference as a function of both ToT in the first and second sensor.

The time walk correction was carried out in two parts. In the first part, the first sensor was time walk corrected. For this time difference, the histograms for all channels with respect to channel 47 in the second sensor were used. An example of such a histogram used for the time walk correction of channel 37 of the first sensor is exhibited in Fig. 5.6. As shown in Fig. 5.6, a strong dependence of the ToA based on the ToT

(a)   (b)
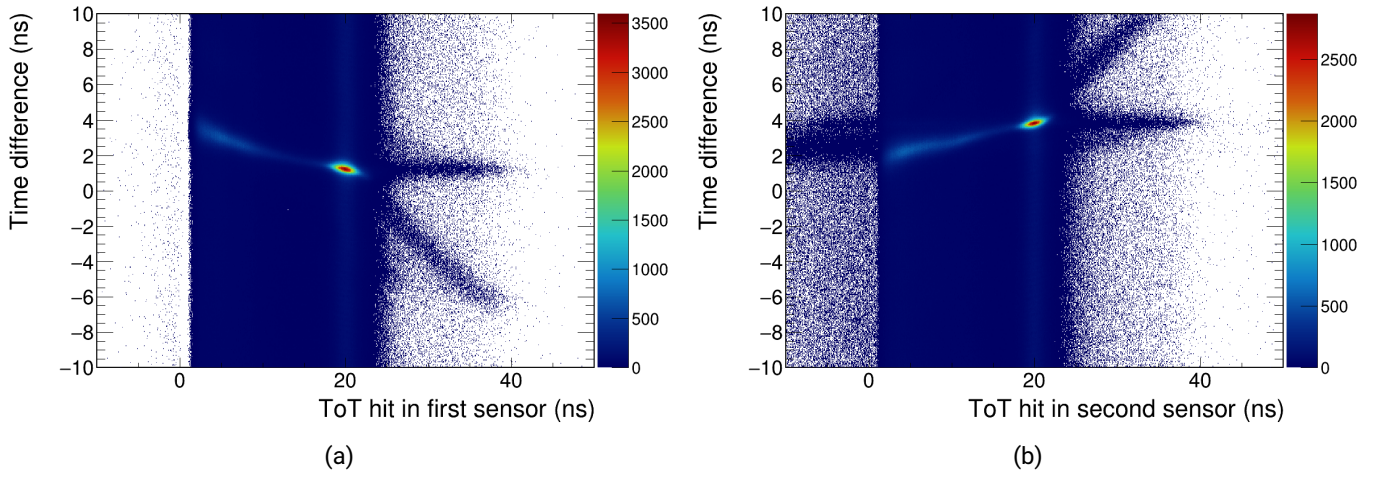
Figure 5.6: First step of the time walk correction. The time difference between hits in two LGAD sensors as a function of a respective hit ToT is shown: (a) exhibits dependence on the ToT of a hit in the first sensor, (b) exhibits dependence on the ToT of a hit in the second sensor.

is present in both plots, indicating the time walk effect. However, the behavior of this dependence differs depending on the sensor (Fig. 5.6a and Fig. 5.6b) due to the different sign obtained in the time difference calculation. In the next step, a projection on the time difference axis of the histogram in Fig. 5.6a was done for each bin to produce the time walk correction parameters. This distribution was fitted with a Gaussian function to obtain the MPV of the measured time difference per ToT bin. To estimate the time walk trend, a linear function was fitted to the MPV ToT values in the signal region (20 ± 1) ns and then extended for the whole ToT range to obtain the time walk correction parameters. The ToA of each hit in the sensor was corrected on an event-by-event basis as follows:

$$ToA_{corrected} = ToA_0 + (a_i * ToT + b_i), \tag{5.2}$$

where ToA_0 is the raw recorded ToA and a_i, b_i are the parameters of the linear time walk function described above where the index i denotes the channel number. The results of those steps are exhibited in Fig. 5.7. When looking at Fig. 5.7, it becomes clear that the linear function did not cover the full ToT range (especially in the low ToT region). However, it fits well with the main signal peak (between 19 ns and 21 ns), which was the goal of this calibration. Further in this chapter, additional ToT cuts will be introduced to remove signals
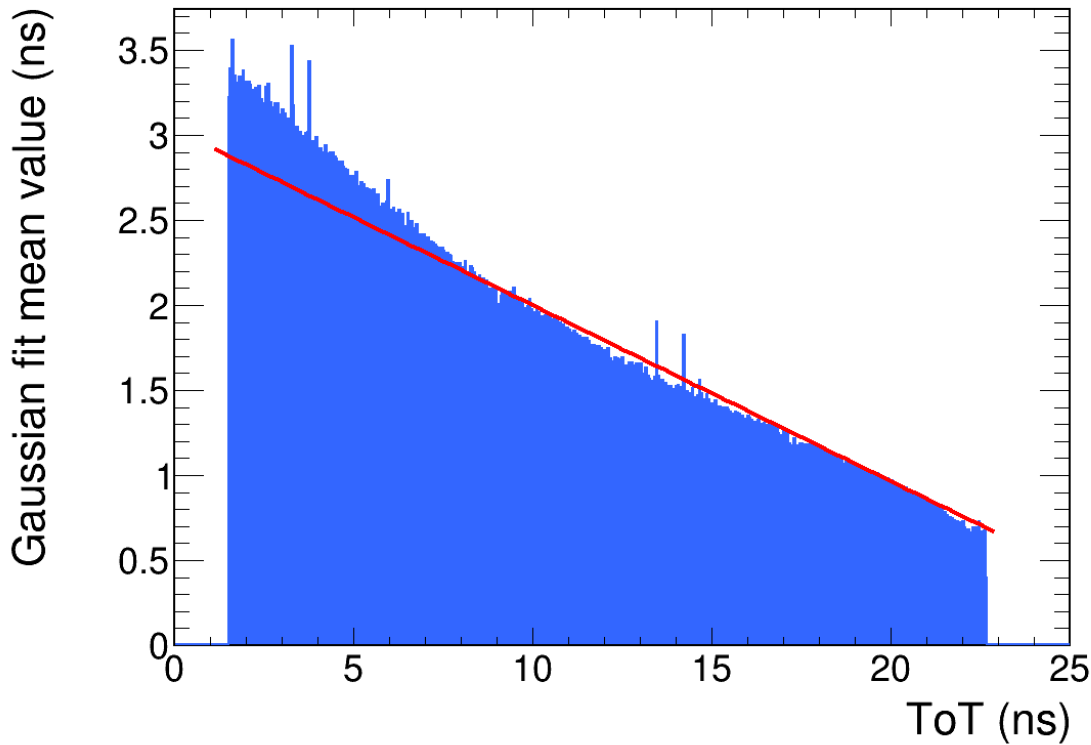
Figure 5.7: Linear fit of ToT mean value per bin. The red line represents the parameters that will be used for the time walk correction.

outside the main signal region, as they originate either from a capacitive coupling effect or electron hits in the LGAD non-sensitive area [7, 58]. Consequently, data that was not fully calibrated was removed from any further analysis. Repeating the same procedure for each channel resulted in a fully time walk corrected first sensor.

The same procedure was then applied to calibrate the second sensor. First, the time difference between the hits in all channels of the second sensor and the reference channel on the second sensor was calculated. Figure 5.8 exhibits the results of this step for one selected channel pair. Data from channel 37 in the first sensor and channel 40 in the second one were used to produce this plot. One can notice the effect of the time walk correction. No dependence of the time difference on the ToT can be observed and the distribution is flat in the main signal (20 ns) region. However, in the low ToT region, a time walk is still present even after the correction, as discussed above.

As a result of the time walk correction, a set of two parameters (a_i, b_i) that define a linear function was obtained for all channels in the system. The full time walk correction result in both LGAD sensors is shown in Fig. 5.9. Figure 5.9 exhibits no systematic dependence of the time difference based on the ToT in the main signal region (20 ± 2) ns, which indicates that the time walk correction was successfully performed.

5.2.3 Time walk correction discussion

When comparing Sec. 4.2.1 and Sec. 5.2.2, one can notice that two different approaches were used for the time walk calibration. The approach presented in Sec. 5.2.2 was not feasible for the proof-of-principle experiment because only one LGAD sensor was used in this experiment. However, the approach from Sec. 4.2.1 could in

principle be also applied to the setup presented in this chapter.

In Sec. 4.2.1, the introduction of $100\,\mathrm{ps}$ cut on the ToT of partner signals made the time walk correction possible. However, this was not the case for the full system test. In this case, the introduction of a narrow ToT cut strongly reduced the amount of data, which, therefore, made the time walk calibration procedure described in Sec. 4.2.1 impossible. The example of the influence of the narrow ToT cut in the selected channel of the first sensor is shown in Fig. 5.10. A zoomed-in version of the data presented in Fig. 5.10 is shown in Fig. 5.11 for a smaller time difference and ToT range. Comparing Fig. 5.11, Fig. 4.7 and Fig. 4.5 one can
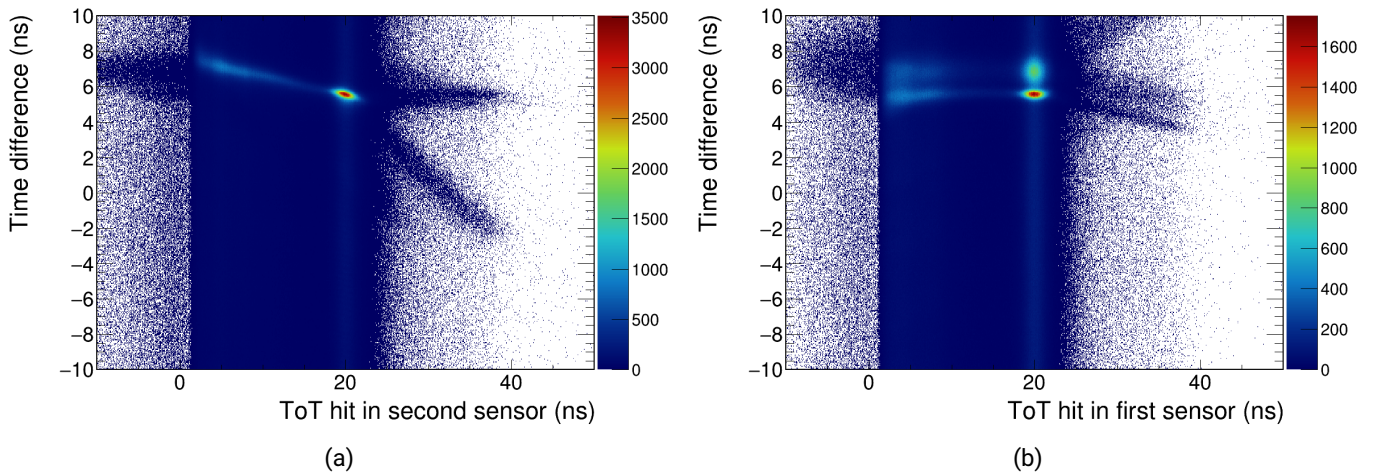
Figure 5.8: Second step of the time walk correction. The time difference between hits in two LGAD sensors as a function of a respective hit ToT is shown: (a) exhibits dependence on the ToT of the hit in the second sensor, (b) exhibits dependence on the ToT of the hit in the first (time walk corrected) sensor. The additional signal is visible in this plot above the main one due to time walk in the second sensor.
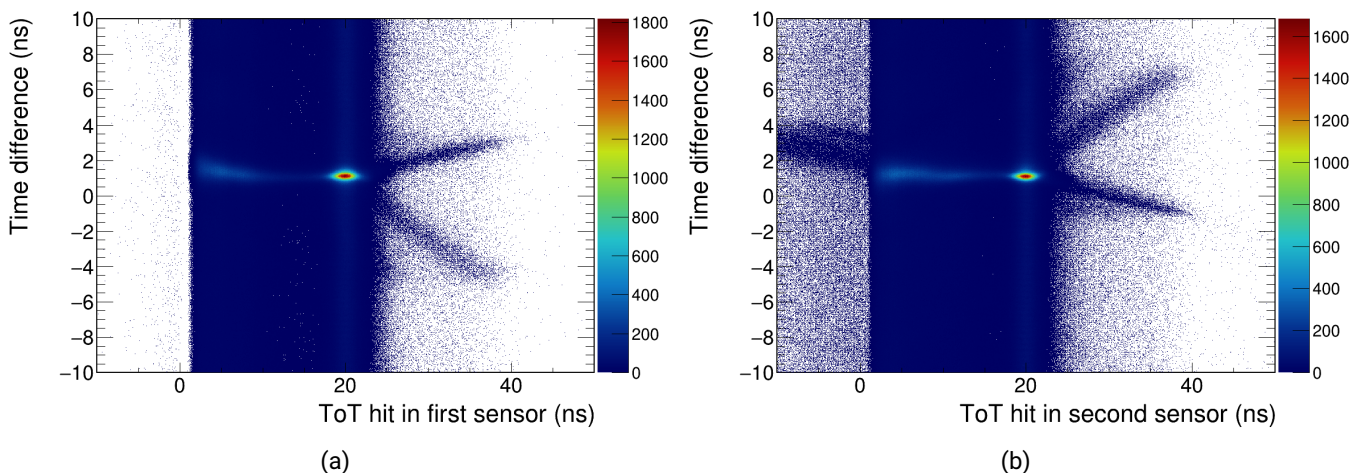
Figure 5.9: The full time walk correction result for selected channels in both sensors. (a) exhibits the time difference depending on the ToT of the hit in the first sensor, and (b) exhibits the time difference depending on the ToT of the hit in the second sensor.
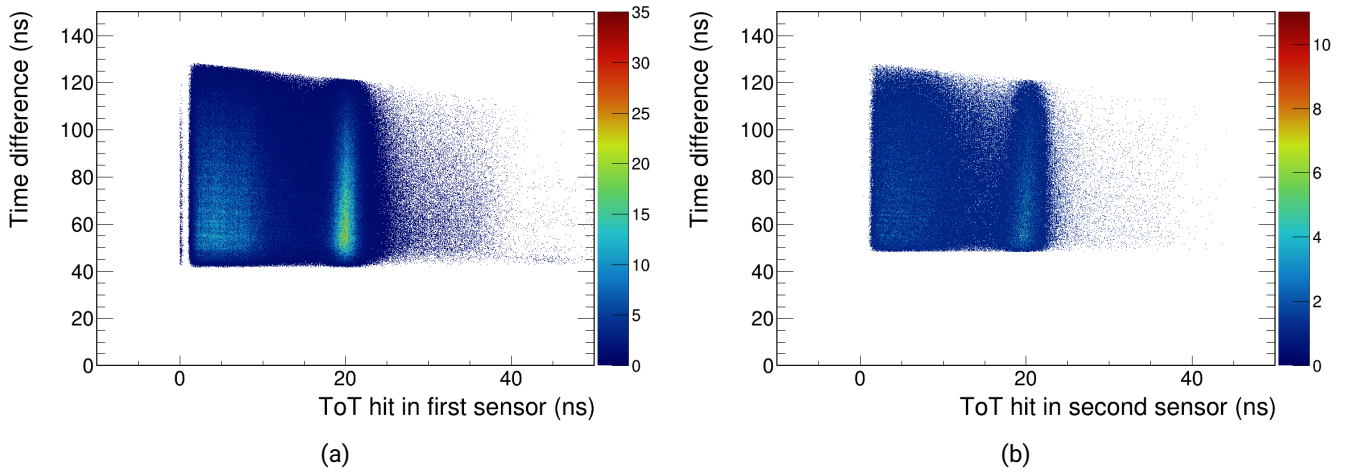
Figure 5.10: Time difference between two hist in channel 37 of the first sensor as a function of the reference hit ToT in a small range: (a) shown the data without narrow ToT cut on correlated signal, (b) shown the same data with narrow ToT cut.
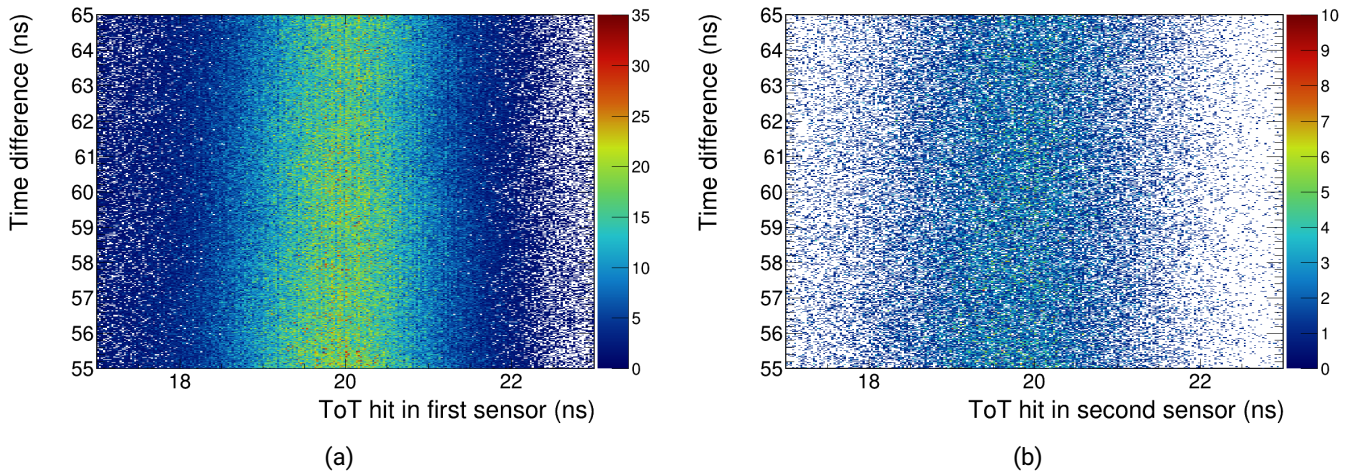

Figure 5.11: Time difference between two hist in channel 37 of the first sensor as a function of the reference hit ToT in a small range: (a) shown the data without narrow ToT cut on correlated signal, (b) shown the same data with narrow ToT cut.

notice that amount of data in both figures are significantly different with much lower amount of entries in Fig. 5.10. To understand this effect, one should look at the multiplicity (number of hits) distribution per event in all channels in the system, which is shown in Fig. 5.12. It has to be mentioned that an additional ToT cut (ToT > 18 ns) on the correlated signal was introduced in Fig. 5.12 to remove the low ToT signals that originated from noise and capacitive coupling. However, one should consider a the narrow ToT cut (100 ps) was introduced to exclude all signals but a small fraction of signals from electrons for the data in Fig. 5.11b. Figure 5.11b demonstrates the amount of data that are relevant for the time walk correction using the approach introduced in Sec. 4.2.1. As shown in Fig. 5.12, the number of events with a multiplicity of more than one is extremely low. However, events with multiplicity one cannot be used for this time walk
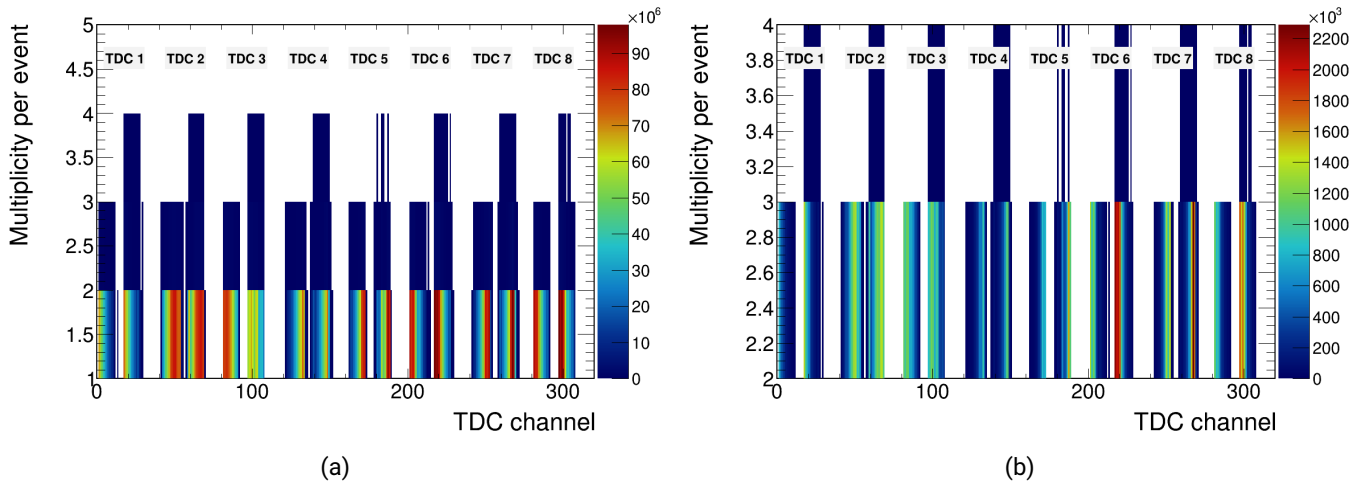
Figure 5.12: Multiplicity distribution per event in all channels of the system: (a) shows all multiplicity, (b) shows multiplicity greater than one.

approach as there is no second hit present to calculate the time difference. Consequently, all channels with a multiplicity of one per event were skipped, thus, reducing the data set. The low amount of events with high multiplicity can explain the insufficient amount of data in Fig. 5.11 for the time walk correction. One possible option would be to obtain more data for the calibration, which, however, would also lead to an increased acquisition and calibration time, given the larger amount of data to be processed. Consequently, the time walk calibration approach from Sec. 4.2.1 was abandoned, and the previously mentioned time walk calibration (Sec. 5.2.2) was used instead.

Another approach would be to further increase the trigger window, which was set to $150\,\mathrm{ns}$ for this experiment. Consequently, more hits would be recorded per event, which would also increase the chance for measuring events with higher multiplicity.

Both approaches will be tested in the future to investigate whether a time walk calibration with only one LGAD sensor is feasible for a full LGAD-based beam monitoring system at the S-DALINAC. The main advantage of such an approach would be the increased flexibility for the geometry of the monitoring system, since only one sensor instead of two would be required for the time walk calibration.

5.2.4 Beam time structure after the time walk correction

An initial beam time structure was obtained after the successful time walk correction. For this purpose, the time difference between two hits inside each channel in the system was calculated. It was done utilizing both sensors independently e.g., without the correlations produced in the previous step. Data from all channels in the same sensor that were time walk corrected was merged into a single histogram. Channels that were not time walk corrected due to the low amount of data in those channels were excluded from the analysis. An additional cut ToT $> 18\,\mathrm{ns}$ on both hits (the reference and correlated hit) was applied. The outcome of this procedure is shown in Fig. 5.13. As one can see, the dead time of the system is about $50\,\mathrm{ns}$, which is represented by the absence of data in the time difference region below $50\,\mathrm{ns}$. However, on the full time difference scale, a periodic structure is not visible. A zoomed-in version of the data presented in Fig. 5.13 is shown in Fig. 5.14 for both sensors and for a smaller time difference range ($10\,\mathrm{ns}$). As shown in those plots, the periodic structure, which is expected to represent the beam time structure, is visible. While the peaks identification and fit procedure will be discussed later in Sec. 5.2.7 and the final results will be discussed in
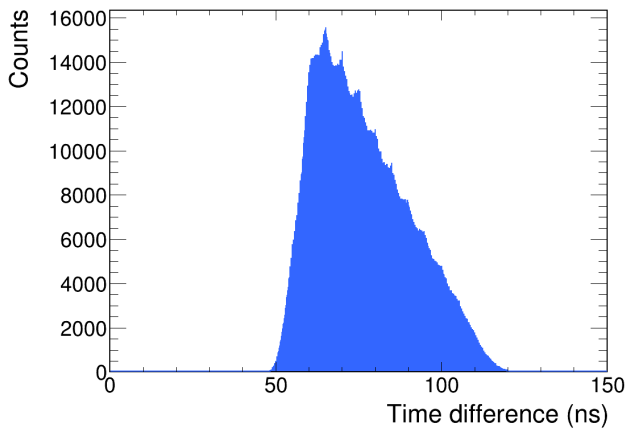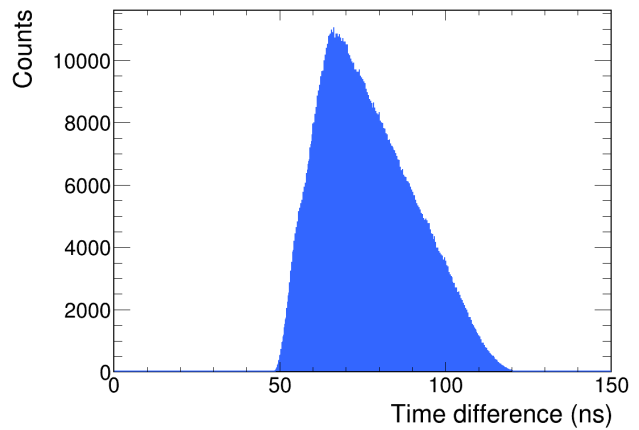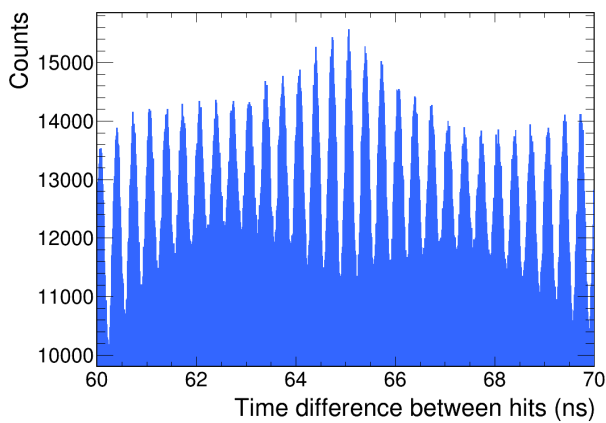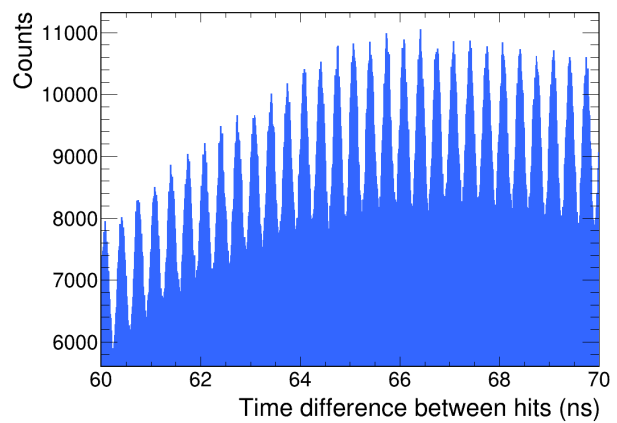
Figure 5.13: The time difference between hits inside the same channels: (a) shows data for all channels in the first sensor and (b) shows data for all channels in the second sensor.

Figure 5.14: The time difference in the small range between hits inside all channels in both sensors: (a) shows data for all channels in the first sensor and (b) shows data for all channels in the second sensor.

Sec. 5.2.8, this section shows only the procedure's outcome to motivate further steps.

As one can see in Fig. 5.14, which exhibits zoomed in time difference range for both sensors, after applying the time walk calibration according to Sec. 5.2.2, the beam time structure could be resolved. However, statistics in both plots in Fig. 5.13, which exhibits the full time difference range for both sensors, are pretty low due to the low multiplicity as discussed in Sec. 5.2.3. An additional correction step was therefore needed to increase the statistics and decrease the measurement time. This step will be discussed in the following section.

5.2.5 Offset correction inside the same sensor

As was discussed in Sec. 5.2.4, the time walk correction was sufficient for resolving the beam time structure at the S-DALINAC. However, this correction procedure required events with high multiplicity to be able to calculate the time difference between two hits inside the same channel, which, as one can see from the previous section, was guaranteed by only considering events with a multiplicity two or more. However, events with only one hit recorded, which represented the major part of the data set in the current experiment, were discarded from the analysis. Up to this point, the time difference between hits inside the same strip of the detector was calculated. On the other hand, it is also possible to include events with multiplicity one into the analysis by calculating the time difference between two hits in different channels in the same detector as shown in Fig. 5.15. As one can see, in this case, one hit in the given channel is sufficient to make a correlation with a hit in another channel of the same sensor. Such an approach would allow to include events with multiplicity one in the analysis. An additional correction is needed for those events since each channel features
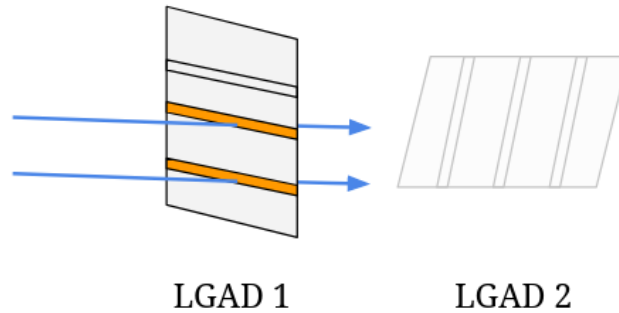
Figure 5.15: The signals correlation scheme for the offset correction. The blue arrows represent two different particles passed through the same sensor and the activated channels are represented by the orange color.

an individual delay due to the different signal path lengths in different channels. A reference channel in each sensor was therefore selected to correct for this offset, and the time difference was calculated between each channel in the sensor and the reference channel. The first sensor was used to illustrate the offset correction. The following procedure was applied for all channels in the same sensor. A ToT cut ($18\,\text{ns} < \text{ToT} < 22\,\text{ns}$) was applied to exclude signals that originate from noise and capacitive coupling. In the next step, as the two particles from the same bunch hit the sensor at the same time, the highest peak in the time difference range $-1\,\text{ns}$ to $1\,\text{ns}$ was identified using ROOT TSpectrum class and fitted with Gaussian function in a range of peak position $\pm\,0.2\,\text{ns}$. In the case of this correction, only one, i.e. the highest peak, is identified. The highest peak was chosen due to the highest number of entries in this peak, and, consequently, a more robust fitting procedure is provided. The mean value of the fit that represents the peak position was used as an offset correction parameter. The correction was done by applying this parameter to all hits ToA in a given channel as follows

$$ToA_{\text{offset corrected}} = ToA_{\text{time walk corrected}} + \text{offset correction parameter}, \tag{5.3}$$

$ToA_{\text{time walk corrected}}$ is the time walk corrected ToA defined in Eq. 5.2, and the offset correction parameter was obtained by the abovementioned procedure. Figure 5.16 exhibits the offset correction procedure for two selected channels in sensor one. As shown in Fig. 5.16, two different groups of channels were obtained. Figure 5.16a represents the first group where the clear separation between peaks is present and, consequently, a proper Gaussian fit can be performed. Also, all peaks in Fig. 5.16a have the same height, but only one
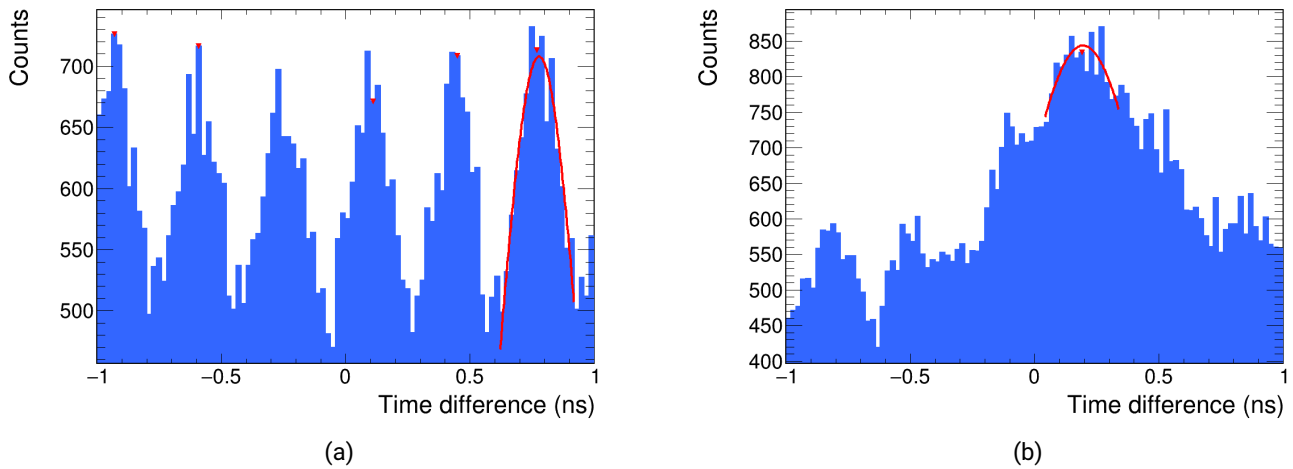
Figure 5.16: The demonstration of the offset correction procedure for two selected channels in the first sensor: (a) shows data from channel 50, (b) shows data from channel 35. The red solid line represents a Gaussian fit of the highest peak in a given range.

peak is selected according to the TSpectrum peak identification algorithm as only one peak needed for this correction. The idea of the offset correction is to overlap particles from the accelerator in time. However, not necessarily particles from the same bunch should be used. Consequently, also particles from different bunches in different channels can be used. Figure 5.16b, on the other hand, exhibits the opposite situation where no single peak exists in a given time difference range. The Gaussian fit in Fig. 5.16b doesn't represent the peak in the given spectrum because of the overlap with neighboring peaks. Consequently, no offset calibration can be done. In the further steps of this analysis, only time walks and offset corrected channels were included, and other channels, where no time walk or offset correction was done, were excluded.

After the offset correction, the time correlation between any two hits in the same event in the sensor was calculated with an additional ToT cut ($18\,\text{ns} < \text{ToT} < 22\,\text{ns}$). The resulting offset-corrected time difference spectrum for the first sensor is shown in Fig. 5.17. The same time difference spectrum for the second sensor is show in Fig. 5.18.

It has to be mentioned that the data set, presented in Fig. 5.17 and Fig. 5.18, corresponds to one minute of the beam time only (while the entire data set for a given detector settings, presented previously in this chapter, corresponds to about 110 minutes of the beam time). After comparing Fig. 5.17 and Fig. 5.18 with Fig. 5.13a and Fig. 5.13b respectively, one can see that the bigger time difference range is covered in both sensors. In general, the proposed approach with both the time walk and offset corrections reduced the amount of required data compared to the approach with the time walk correction only. Consequently, the data acquisition time needed for resolving the beam time structure was drastically decreased after applying all necessary corrections. This fact highlights the importance of an additional offset correction to be able to include events with multiplicity one, which was not the case in the approach without the offset correction (see Sec. 5.2.4).

5.2.6 Time difference correction between sensors

As was shown in the previous section, a single sensor can be used to resolve the S-DALINAC beam time structure. However, as the setup in this experiment employed two LGAD sensors, an additional correction was necessary to utilize both of these sensors together. For this approach, a time difference correction between both sensors had to be performed.
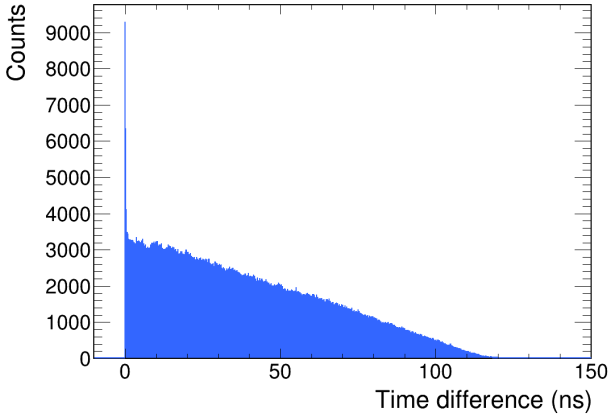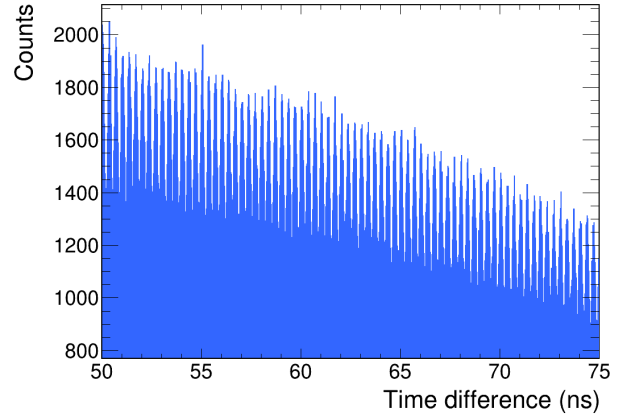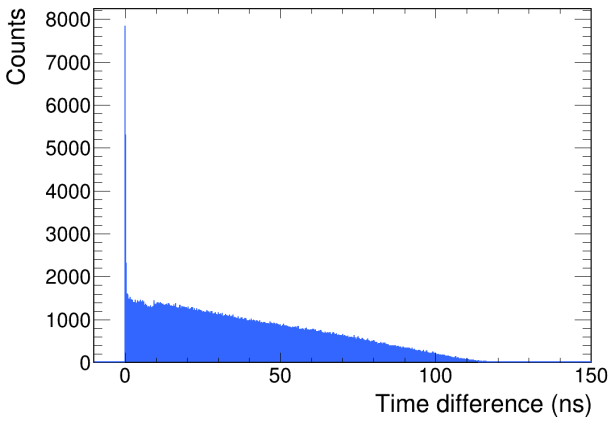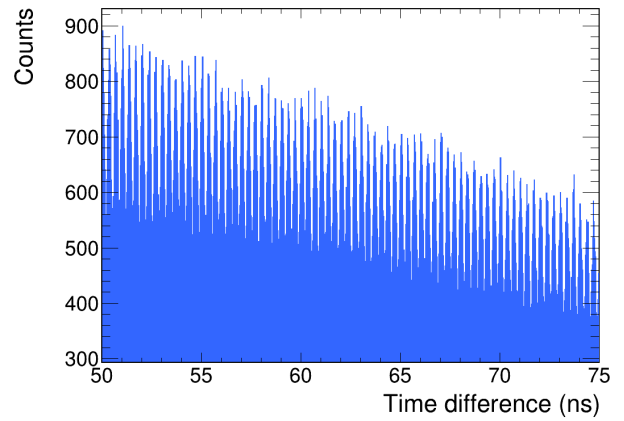
Figure 5.17: The time difference between any two hits in the same event in the first sensor. (a) exhibits the full difference range, and (b) exhibits a small range of $25\,\mathrm{ns}$.

Figure 5.18: The time difference between any two hits in the same event in the second sensor. (a) exhibits the full difference range, and (b) exhibits a small range of $25\,\mathrm{ns}$.

As mentioned before, the signal path length differs for different channels. In the case of two sensors, there is an additional delay in the second sensor's electron registration with respect to the first sensor because of the additional ToF between the sensors. An additional calibration was needed to correct those delays, which was performed in two steps. In the first step, the first sensor was corrected for the ToA delay. For this, a reference channel in the second sensor was selected, and the time difference between hits in all channels of the first sensor was calculated with respect to the reference channel. Additional cuts on ToA and ToT were applied:

$$\begin{cases} |ToA_i - ToA_{ref}| < 10\,\mathrm{ns} \\ 18\,\mathrm{ns} < ToT < 22\,\mathrm{ns}, \end{cases} \tag{5.4}$$

where $\mathrm{ToA_i}$ is the ToA in channel i of the first sensor and $\mathrm{ToA_{ref}}$ is the ToA in the selected reference channel in the second sensor. One can notice an additional time cut on the particle's ToA in both sensors, which was not

used before. The time difference correction utilizes the events when the same particles hit both sensors. As the distance between sensors is about 1 cm, the respective ToF between sensors is short. The ToA cut excludes the signals that originate from different particles hitting the sensors.

After that, a projection on the time difference axis and the spectrum with a peak representing the particle's ToF between sensors was obtained. This peak was fitted with a Gaussian function. The obtained mean value from the fit represents the MPV for the ToF (ToF_{MPV}) and was used for the time difference correction as follows:

$$ToA_{\text{time difference corrected}} = ToA_{\text{offset corrected}} - ToF_{MPV}, \tag{5.5}$$

where ToA$_{\text{offsetcorrected}}$ is the offset corrected ToA defined in Eq. 5.3 and the time difference parameter is defined above (ToF$_{MPV}$). As an intermediate step, all channels in the first sensor were offset-corrected with respect to the selected reference channel in the second sensor. The same steps were taken to correct the second sensor. First, a reference channel in the first sensor was selected, and the cuts from Eq. 5.4 were applied. Next, the fitting procedure was repeated.

After these steps, the measured ToA in both sensors was shifted to the same zero time difference value using Eq. 5.5, which means that the same particle should have the same ToA value in both sensors. An example of the second step of the time difference correction is shown in Fig. 5.19. After the time difference and offset
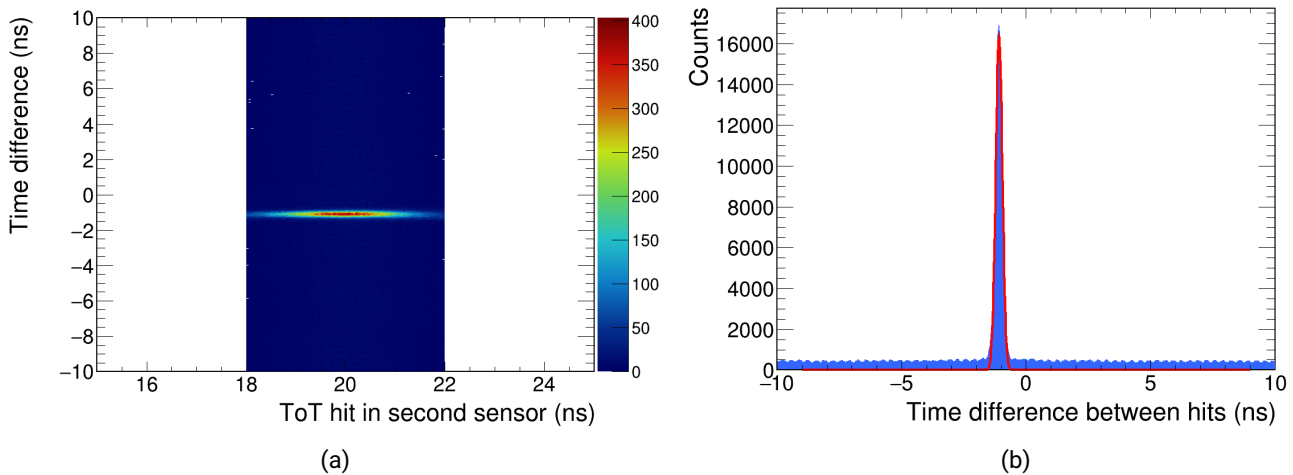

<div align="center">(a)   (b)</div>

Figure 5.19: The example of the time difference correction for the second sensor. (a) shown the time difference between the selected channel in the second sensor and the reference channel in the first sensor and (b) exhibits projection on the time difference axis and Gaussian fit (red solid line).

corrections, it was possible to simultaneously calculate the time difference between any two hits in both sensors. A time difference between all hits in the first and second sensors was calculated for this purpose. The outcome of this step is shown in Fig. 5.20. As one can see in Fig. 5.20a, there is a main peak (Fig. 5.20b) at 0 ns time difference, which corresponds to the same particle hitting both sensors. However, there are also peaks with much smaller intensity outside the main peak, which originates from correlation between different particles. Two selected sub-ranges of the time difference between two hits in both sensors are shown in Fig. 5.20c and Fig. 5.20d.

To resolve the time structure the same approach as presented in Sec. 4.2.2 was used. The data presented in Fig. 5.20 was used and the time difference range from -5 ns to 5 ns was excluded from the analysis to exclude the main peak and fulfill the condition in Eq. 4.4. It has to be mentioned that only offset-corrected channels,
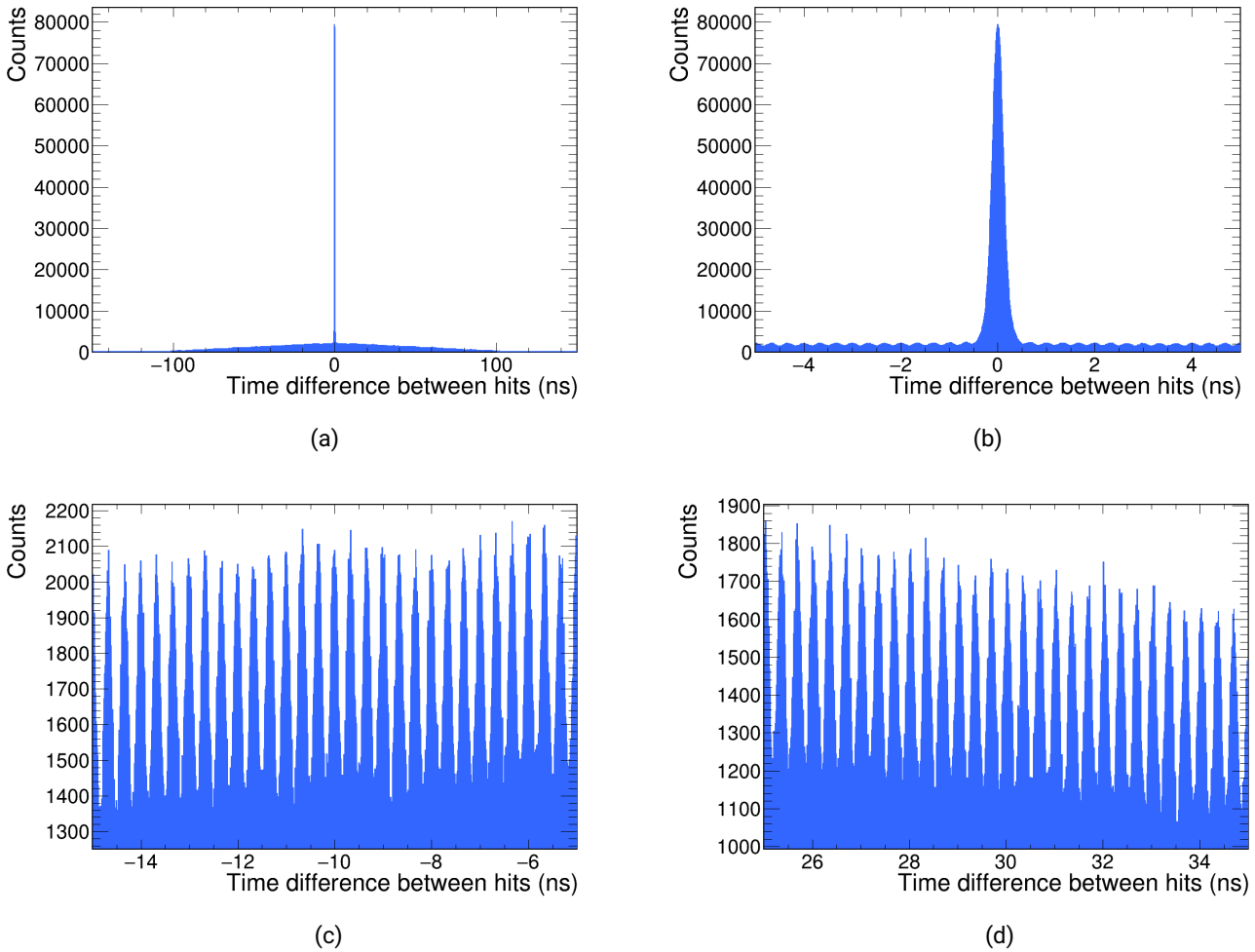
Figure 5.20: The time difference between any two hits in first and second sensors. (a) shows the full time difference range, (b) shows the main peak, which originates from the same particle hitting both sensors, and (c) and (d) exhibits two selected ranges outside of the main peak.

as described in Sec. 5.2.5 in both sensors, were included in this analysis.

5.2.7 Peak identification

In the next step, peaks in Fig. 5.17, Fig. 5.18 and Fig. 5.20 were identified using a similar procedure as described in Sec. 4.2.2.

First, the time difference range was divided into sub-ranges of 10 ns. It was done because the amplitude of the peaks is not constant and changes in different ranges of the time difference range as shown in Fig. 5.20. The splitting into smaller time difference ranges increased the peak identification efficiency. Second, similar to Sec. 4.2.2, each peak in the sub-range was identified using the TSpectrum *SearchHighRes* function. The function parameters used for peak identification are summarized in Tab. 5.1. The condition for the peak identification algorithm stayed the same as described by Eq. 4.4. As a result of this step, N peaks in the spectrum were identified given the peak position X_i and the peak amplitude Y_i. These peaks were fitted in two steps. In the first step, each peak position and amplitude were obtained. This was done by applying a

Parameter	Value
Sigma	15
Threshold	60 (%)
Background removal	false
Deconvolution iterations	10
Markov chain method	false

Table 5.1: Parameters for the TSpectrum peak search function.

Gaussian fit to each peak in the range $X_i \pm 0.2$ ns. The fit parameters for the first step are shown in Tab. 5.2. In the next step, the whole sub-range was fitted with the sum of Gaussian functions as follows:

Parameter	Initial value	Parameter limits	
		Minimum	Maximum
Constant	1	$0.5 \times Y_i$	Y_i
Mean	X_i	no lower limit	no upper limit
Sigma	0.1	0.02	0.5

Table 5.2: Gaussian fit parameters initial values and limits for the first step of the peak fitting procedure as described in the text.

$$f(x) = \sum_{i=1}^{N} [\text{Constant}]_i \times exp\left(-0.5 \times \left(\frac{x - [\text{Mean}]_i}{[\text{Sigma}]_i}\right)^2\right),\tag{5.6}$$

where N is the number of identified peaks in the sub-range, $[\text{Constant}]_i$, $[\text{Mean}]_i$ and $[\text{Sigma}]_i$ are the fit parameters from the first fit step. The summary of the fit parameters for the function defined by Eq. 5.6 is given in Tab. 5.3 The outcome of the peak identification and fitting procedures for the first sensor are shown

Parameter	Initial value	Parameter limits	
		Minimum	Maximum
Constant	Constant_i	no lower limit	no upper limit
Mean	Mean_i	Mean_i - 0.3 ns	Mean_i + 0.3 ns
Sigma	Sigma_i	0.05	0.3

Table 5.3: Gaussian fit parameters initial values and limits for the second step of the peak fitting procedure as described in the text.

in Fig. 5.21. As one can see from these plots, in both time difference sub-ranges all peaks were identified. Additionally, the function defined by Eq. 5.6 correctly fitted the shape of all peaks in the given spectrum in contrast to the procedure described in Sec. 4.2.2.

5.2.8 Final result

The same step as in Chapter 4 was done to obtain the mean time difference between two consecutive peaks. For this, the difference between the position of two consecutive identified peaks (as described in Sec. 5.2.7)
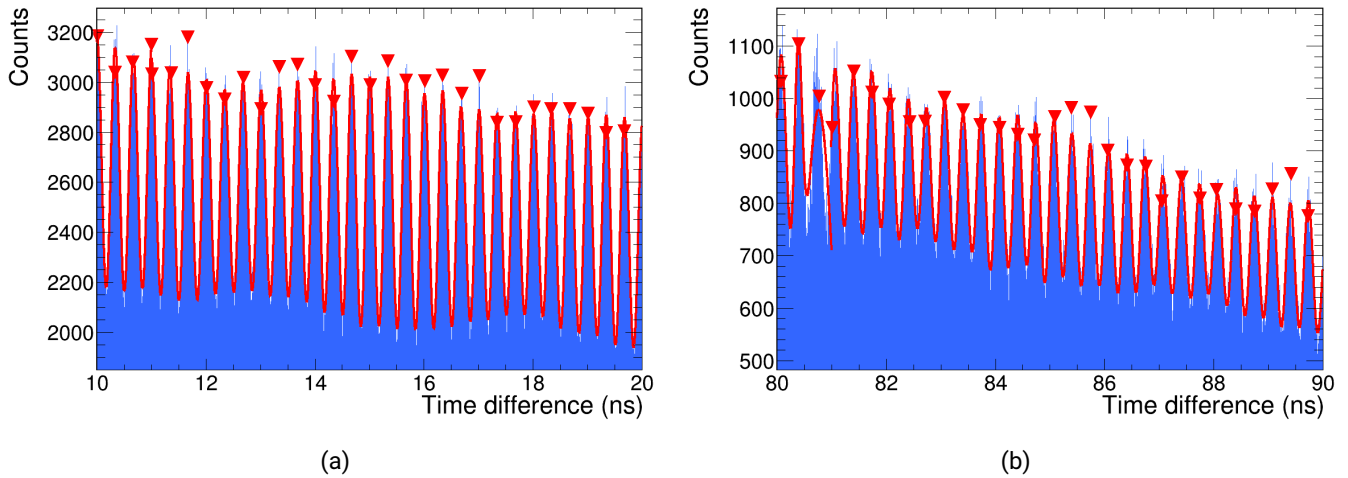
Figure 5.21: The example of the peak identification and fitting procedure for two selected sub-ranges for the first sensor. (a) exhibits the procedure in the $10\,\text{ns}$ to $20\,\text{ns}$ time difference range, and (b) exhibits the same procedure in $80\,\text{ns}$ to $90\,\text{ns}$ range. Red triangles represent the identified peaks' position and amplitude, and the red solid line represents the fit function defined by Eq. 5.6. Full data is show in Fig. 5.17.

was calculated. After that, a one-dimensional histogram was filled with those values. To evaluate the detector's performance, a second histogram was filled with the [Sigma] values obtained from the fit (Eq. 5.6). Both of the resulting histograms were fitted with the Gaussian function to obtain mean values of the mean difference between two peaks and mean peak width (sigma). The outcome of this step is shown in Fig. 5.22 and Fig. 5.23 for the first and second sensors respectively. Additionally, the same steps were applied to the result of the peak identification procedure for the data after the time difference correction between the two sensors as described in Sec. 5.2.6, which is shown in Fig. 5.24. As one can see in all plots, the mean time difference distribution
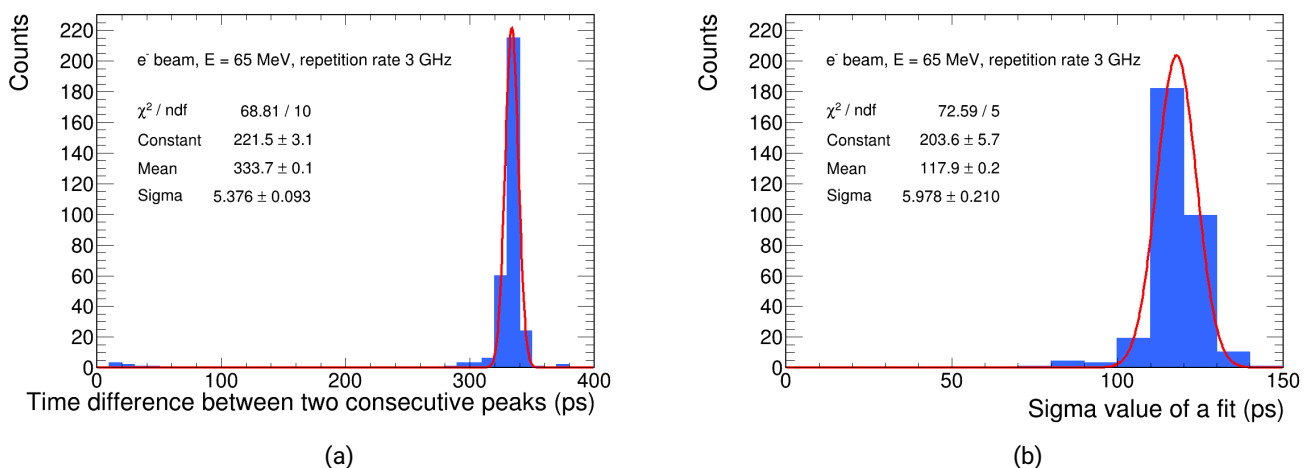
Figure 5.22: The time difference between two peaks and width of peaks for the first sensor. (a) shows the time difference distribution between two peaks, and (b) shows the peak width (sigma) distribution.
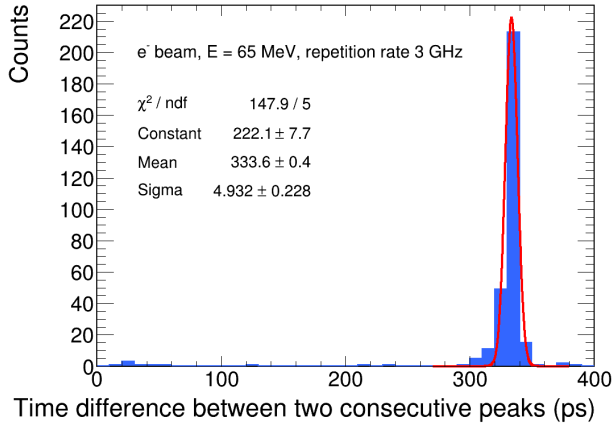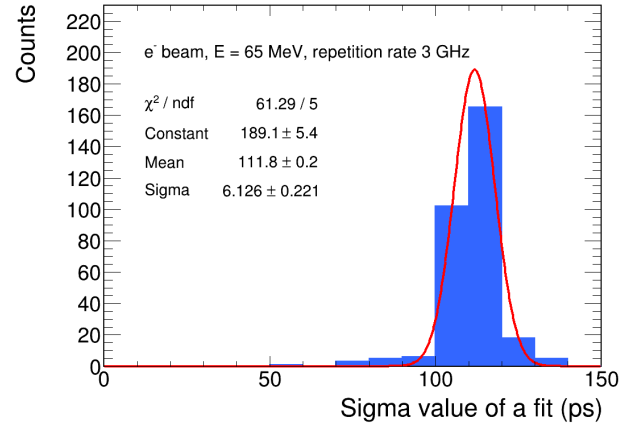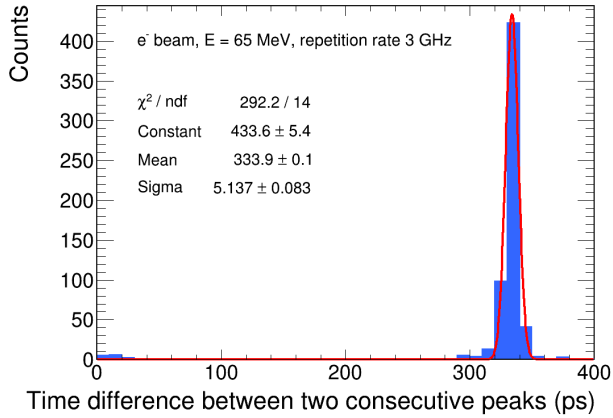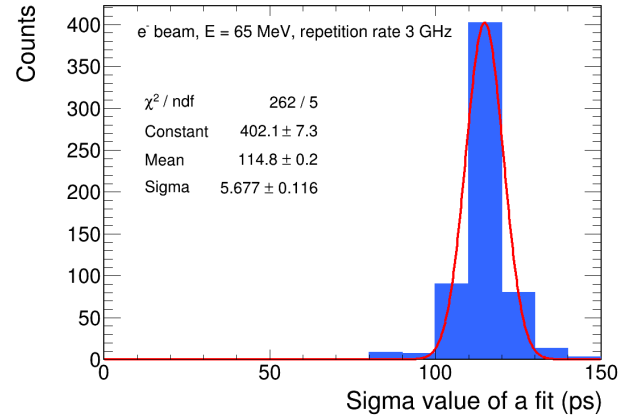
Figure 5.23: The difference between two peaks and width of peaks for the second sensor. (a) shows the difference distribution between two peaks, and (b) shows the peak width (sigma) distribution.

Figure 5.24: The difference between two peaks and width of peaks for correlated signals in both sensors. (a) shows the difference distribution between two peaks, and (b) shows the peak width (sigma) distribution.

has a peak at $333\,\mathrm{ps}$, which corresponds to the $3\,\mathrm{GHz}$ time structure of the S-DALINAC. Additionally, the number of entries outside this peak in both sensors is significantly reduced compared to the results presented in Chapter 4, which indicates further improvements in the peak identification procedure.

Taking into account that two independent time measurements of particles' ToA were done to obtain results from Fig. 5.17, the time resolution of the sensor was estimated as follows:

$$\sigma^2_{t_{total}} = \sigma^2_{t_1} + \sigma^2_{t_2},$$

where σ_{total} was obtained from Fig. 5.22b, Fig. 5.23b and Fig. 5.24b, and $\sigma_{t_1} = \sigma_{t_2} = \sigma_t$ are the time resolution values for the individual sensors, which was assumed to be constant and similar for both sensors for the entire test. This was mainly justified by the fact that no significant radiation damage to the sensors was expected

(see Sec. 3.4 for the LGAD radiation hardness discussion). Taking those assumptions into consideration, the intrinsic time resolution of each sensor was then calculated as follows

$$\sigma_{t_{total}}^2 = \sigma_t^2 + \sigma_t^2 = 2\sigma_t^2$$

$$\sigma_t = \frac{\sigma_{t_{total}}}{\sqrt{2}}$$

The final results of the analysis are summarised in Tab. 5.4. As one can see, the beam time structure (mean

Parameter	Hit correlated in sensor		
	First	Second	Both
Mean time difference between two peaks (ps)	333.7 ± 0.1	333.6 ± 0.4	333.9 ± 0.1
$\sigma_{t_{total}}$ (ps)	117.9 ± 0.2	111.8 ± 0.2	114.8 ± 0.2
σ (ps)	83.37 ± 0.14	79.05 ± 0.14	81.18 ± 0.14

Table 5.4: Summary of the analysis results. The values obtained from fits in Fig. 5.22, Fig. 5.23 and Fig. 5.24
.

time difference between two peaks in Tab. 5.4) obtained from both sensors corresponds to the S-DALINAC operational frequency of 3 GHz. This concludes that the full system test at the S-DALINAC was successful, and the time structure of the S-DALINAC was successfully resolved. The time resolution of 83.4 ps and 79.1 ps for the first and second sensors, respectively, were demonstrated.

The beam time structure utilizing a single sensor with the time walk correction only

As was mentioned before in Sec. 5.2.4, it is possible to resolve the beam time structure using the single LGAD sensor after the time walk correction only. The exact peak identification procedure as presented in Sec. 5.2.7 was applied to the data presented in Sec. 5.2.4. The respective time difference spectrum is shown in Fig. 5.13 and the exact peak identification procedure as presented in Sec. 5.2.7 was applied to the data presented in this figure. The result of the peaks identification procedure is shown in Fig. 5.25. As one can see from Fig. 5.25, the time walk correction was sufficient to resolve the S-DALINAC beam time structure in both sensors. However, this approach required large statistics, and the advantages of the other approaches were shown in Sec. 5.2.5 and Sec. 5.2.6.

5.3 Summary

The successful application of the LGAD-based setup for beam time structure monitoring in the conventional operation mode of the S-DALINAC was demonstrated in this chapter. It was achieved using two LGAD sensors independently and also by pairing them together. For this, several correction steps were performed.

First, the time walk correction was done to achieve the best possible time resolution. For this purpose, the time difference correction was done utilizing both sensors. In the previous chapter, on the other hand, the time walk calibration could be done using only a single sensor. However, in this chapter, it was impossible to achieve the time walk correction utilizing only a single sensor due to the low amount of data (see Sec. 5.2.3). Further investigation to allow for a time walk correction using only one sensor with the current setup should be tested during further experiments as a time walk correction is crucial for the detector's performance. The ability to perform the time walk correction utilizing only one sensor would allow for more flexibility in the
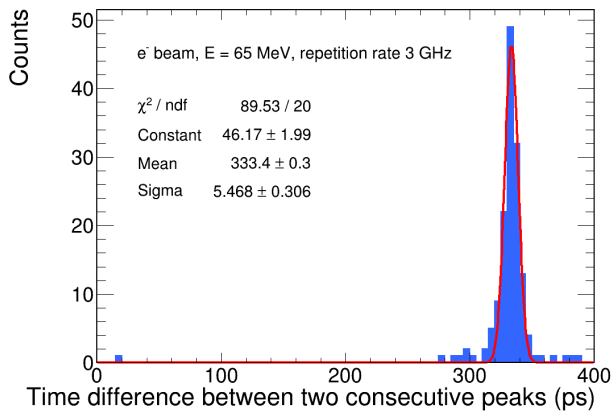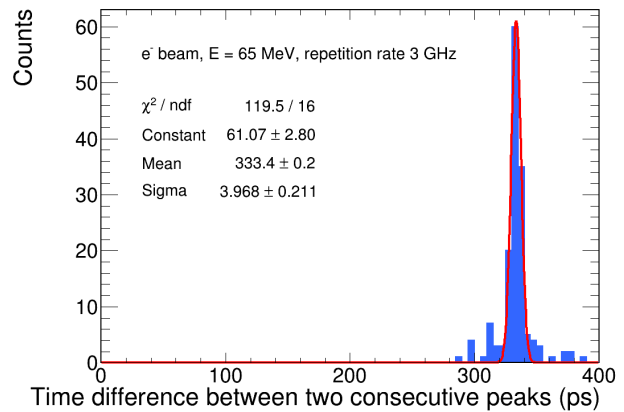
Figure 5.25: The time difference between two consecutive identified peaks in the same channel and corresponding Gaussian fit (red solid line) with fit parameters. (a) shows the time difference in the first sensor, and (b) shows the time difference in the second sensor.

design of the proposed beam time structure monitoring system, as this will allow usage of either a single- or multi-sensor system.

The offset correction inside the same sensor was utilized to increase the statistics and reduce the amount of the data required to resolve the beam time structure. However, it was not possible to perform this correction for all channels. As discussed in Sec. 5.2.5 and shown in Fig. 5.16, some channels had insufficient time resolution, which made an offset correction impossible. The reason for this is currently unknown and requires further investigation.

Ultimately, the setup and necessary analysis software are prepared and ready for testing in the S-DALINAC ERL operation mode. However, for such a test, the setup should be moved inside the accelerator hall and placed close to the beam recirculation lines. Design and geometry optimization for the test in the accelerator hall will be discussed in detail in the following chapter.

6 Geant4 feasibility study of an LGAD-based beam monitoring system for the ERL mode at the S-DALINAC

Computational simulations play a crucial role in modern experiments. They allow to estimate the experimental outcome prior to conducting the experiment, which can help to optimize the experimental setup and detector performance. It includes but is not limited to detector performance, an experiment design, and possible physics results.

Geant4 [59–61] is a framework for simulations of a particle's interactions with matter using the Monte Carlo methods. The Monte Carlo method is a general name for a class of numerical algorithms that uses random sampling to simulate complex systems with many different parameters and obtain the probability distribution or numerical value for the parameters of interest [62].

While the results shown in the previous chapters demonstrated the feasibility of an LGAD-based detector system for measuring the beam time structure of a $3\,\mathrm{GHz}$ beam, the main objective for a future detector system is also to resolve the beam structure of the S-DALINAC operated in its ERL mode. However, in order to achieve that, the detectors have to be moved into the main accelerator hall. Furthermore, the LGAD installation should be non-destructive, which means it cannot be installed in the beam path directly and it should be mounted close to the recirculation line. Due to those positioning constraints of the detector, only two possibilities for measurement exist. The beam time structure could be either monitored by measuring the beam halo outside the recirculation line or pairing the LGAD with a wire scanner [24], which is currently being developed. In the case of the wire scanner, a thin wire is moved through the beamline for a short time (order of seconds) and particles by the scattered beam can then be measured. In both cases, the LGAD-based system close to the recirculation beamline can be used to measure either the beam halo or re-scattered particles.

This chapter presents the results of a Monte Carlo feasibility study of an LGAD-based beam monitoring system for the S-DALINAC operated in its ERL mode paired with a wire scanner. This mainly involves geometry optimizations of the LGAD system and an estimation of the detector performance. The different detector positions along the beam line were simulated, and the position-dependent ToA spectra were studied. The obtained ToA spectra were used to estimate the detector performance and optimize the detector placement.

6.1 Simulation setup

Geant4 is a framework that provides users with a wide range of tools to simulate conditions in an experiment. However, to create a realistic simulation that correctly reflects those experimental conditions, the geometry and underlying physics have to be defined accordingly by the user. This also includes a correct definition of the geometry of the simulation, as well as listing all involved particles and their corresponding physics processes. All steps of creating a realistic Monte Carlo simulation in Geant4 of an LGAD-based beam monitoring system for the S-DALINAC will be presented in this section. The simulation was done using Geant4 version 11.01 patch 02.
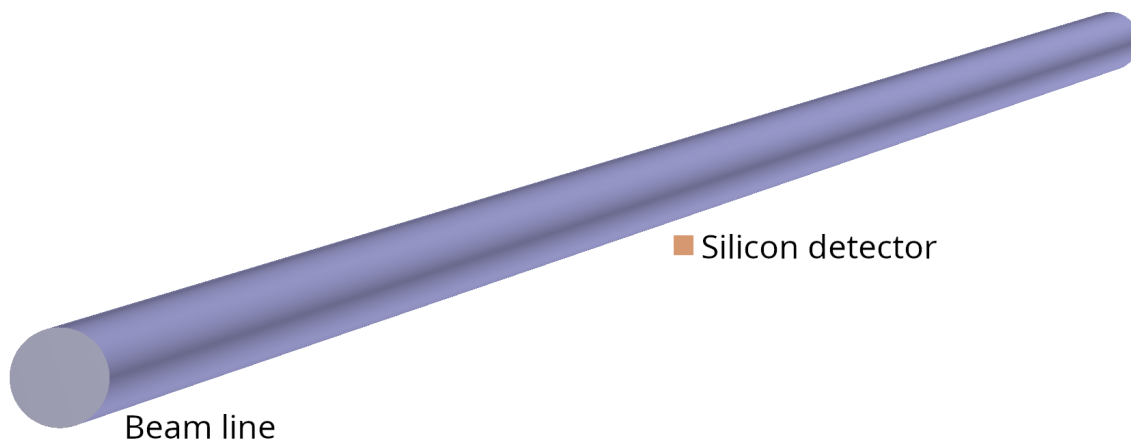
(a)
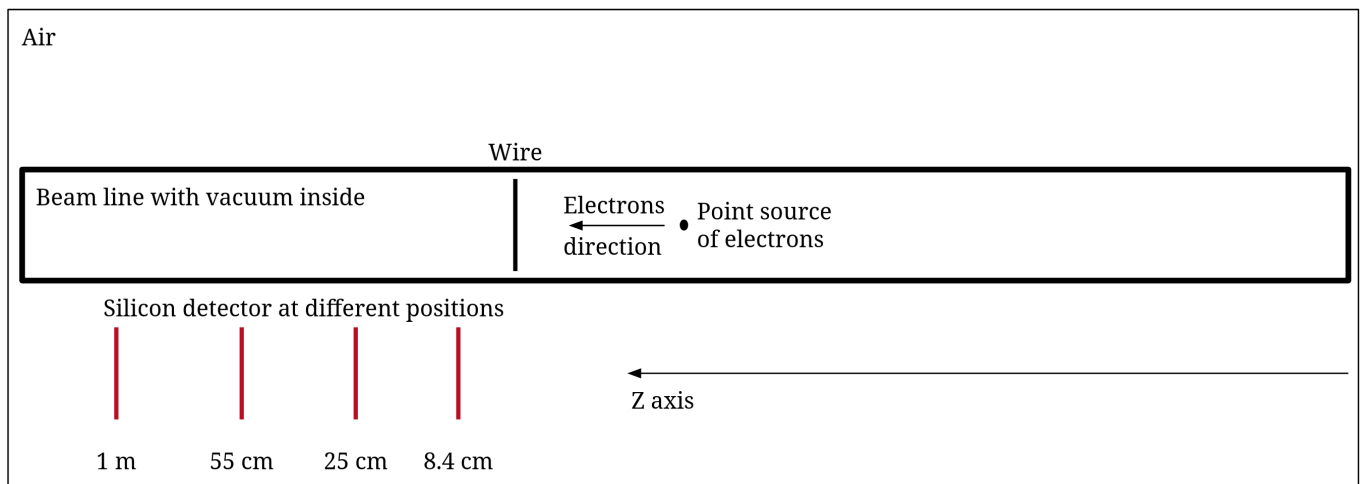
(b)

Figure 6.1: Geant4 simulation geometry: (a) show the silicon detector position with respect to the beam line. The world is not shown in the figure, (b) shows the scheme of the simulation geometry with all objects, the primary particle source, and the detector in four different positions. Distances are not up to scale.

6.1.1 Geometry of the simulation

As a starting point of each simulation, a world object should be created. This object contains the particle source, all necessary detectors and passive materials, which are required to recreate the experimental conditions of the actual experiment correctly. The primary particles will be generated inside the world volume, and they, as well as any secondary particles, are transported through the world object according to the underlying physics. After leaving the world boundaries, any particle is destroyed. Box geometry is most commonly used to define the world volume. To simulate the possible conditions in the accelerator hall, the world volume was defined as a box filled with air and dimension $100\,\text{cm} \times 100\,\text{cm} \times 700\,\text{cm}$ in X, Y, and Z direction, respectively. The center of the world object defines the coordinate system of the simulation and is its zero point.

Next, the S-DALINAC recirculation beam line was created. For this, an iron pipe was created. The inner radius of the actual pipe is $17.5\,\text{mm}$, its thickness is $1.5\,\text{mm}$ [63]. A small part of the beam pipe was simulated

with a total length of $6\,\text{m}$. This long pipe is needed due to studies of the influence of the detector position along the beam pipe on the particle's ToA. The pipe was placed at the center of the world volume. A vacuum was defined inside the tube. $30\,\text{µm}$ thick glass exit windows were created at both ends of the pipe using the custom-defined material as stated in Tab. 6.1.

To simulate the wire scanner, a $100\,\text{µm}$ thick and $2.4\,\text{cm}$ long tungsten wire was placed inside the beamline orthogonal to the beam direction and placed $5\,\text{cm}$ downstream the particle source, which will be described later. As it was mentioned before, the wire can be moved inside the beam line. However, in the simulation, it was made stationary to increase the number of interactions with the incident particles, as will be discussed later.

To simulate the LGAD detector, a $1\,\text{cm} \times 1\,\text{cm} \times 50\,\text{µm}$ silicon box was created. It was used as a so-called *sensitive detector*, which means that any particle's interaction inside this box was recorded and saved for further analysis while no information was recorded about the interaction outside of the sensitive detector. The silicon detector was placed at four different positions below the beamline to investigate the position's influence on the ToA spectrum. The detector was set to the following positions: $(0, -3.4\,\text{cm}, 8.4\,\text{cm})$, $(0, -3.4\,\text{cm}, 25\,\text{cm})$, $(0, -3.4\,\text{cm}, 55\,\text{cm})$ and $(0, -3.4\,\text{cm}, 1\,\text{m})$.

The following information was collected for each interaction in the detector:

- hit position in a local coordinate system (coordinate system of the detector)

- global hit time (time since the beginning of the Geant4 event)

- local hit time (time since creation of a particle)

- deposited energy

- particle's momentum

- particle's name

- kinetic energy

- parent particle ID

- track ID

- particle's creation volume name

- particle's initial kinetic energy

- particle's creation process name

- particle's total energy deposition in the detector volume

The geometry of the simulation is shown in Fig. 6.1 and a summary is given in Tab. 6.1.

6.1.2 Simulation of primary particles

In the simulation, the conditions of the beam, close to the ones described in Chapter 5, were recreated. The simulation used $65\,\text{MeV}$ electrons as primary particles. All electrons originated from the center of the coordinate system and were launched along the Z-axis in a positive direction. 10^8 electrons per run were simulated. Considering the stationary position of the wire, a point-like source of particles was simulated to guarantee that all primary particles hit the wire. It has to be mentioned that it is possible to simulate the

Volume name	Object type	Size, cm	Position, (x, y, z) cm	Material	
				Name	Geant4 definition
World	Box	$100 \times 100 \times 700$	(0, 0, 0)	Air	G4_AIR
Beamline	Tube	$1.75 \times 1.9 \times 600$	(0, 0, 0)	Iron	G4_Fe
Vacuum	Tube	$0 \times 1.75 \times 599.994$	(0, 0, 0)	Vacuum	G4_Galactic
Exit window	Tube	$0 \times 1.75 \times 30 * 10^{-4}$	(0, 0, -299.9985) (0, 0, 299.9985)	Glass	Custom material: • 70 % SiO_2 • 15 % CaO • 15 % Na_2O
LGAD	Box	$1 \times 1 \times 50 * 10^{-4}$	(0, -3.4, 8.4) (0, -3.4, 25) (0, -3.4, 55) (0, -3.4, 100)	Silicon	G4_Si
Wire	Tube	$0 \times 50 \times 1.7$ 90° rotated along the X axis	(0, 0, 5)	Tungsten	G4_W

Table 6.1: Summary of the Geant4 simulation geometry. Box size column represents width $\times$ height $\times$ length, tube geometry given as inner radius $\times$ outer radius $\times$ length.

entire beam profile. Considering that the wire was placed stationary introducing the beam profile will lead to events where particles will not have any position overlap with the wire, and, consequently, no scattering will occur. Such events do not provide any information as particles will never reach the detector. To avoid that situation, a point-like source was chosen, which was placed in a position to overlap with a wire. Consequently, all simulated primary electrons should interact with the wire.

6.1.3 Physics processes

Describing particles and physics processes is one of the most crucial steps in Geant4 simulations. A user can define every particle and every process in the simulation or use a pre-defined Geant4 physics list. This simulation used a physics list called *FTFP_BERT_EMV* [64]. FTFP_BERT is a default Geant4 physics list covering a wide range of energies and particles. Since the energy of primary particles is small, an electromagnetic part of the physics list is the most important. The "_EMV" part in the physics list name indicates that a so-called standard electromagnetic physics constructor with the default option was used. The "_EMV" physics list covers an energy of 0 to 100 TeV for gammas, electrons, and positrons [64], which is a much wider energy range than required for the simulation. On the other hand, all required processes are included in the desired energy range. For example, multiple scattering, ionization, Bremsstrahlung, and positron annihilation are implemented for electrons and protons in this physics list below 100 MeV [64]. Furthermore, the corresponding processes that are relevant in the given energy range for other particles, like protons, neutrons, and ions, are implemented in the physics list as well.

6.2 Results

6.2.1 Time of Arrival

As the main application of an LGAD in the scope of this work is time measurements, the ToA of each particle hitting the detector was measured. However, not all of these particles would be detected in an actual detector because not all of these events will occur with the energy deposition in the detector. Because of that, an additional analysis flag *firstEdepInVolume* was introduced. This flag indicates the first interaction for each track (assigned to each particle in the simulation and is unique for a given particle per simulated primary particle) in the detection volume that deposited energy. The simplified assumption was made that any energy deposition leads to particle detection and no minimal deposited energy is required. Consequently, any first step with a non-zero energy deposition value for each track was assigned with the *firstEdepInVolume* flag. As a result, the ToA of the particle will be the first hit with energy deposition only. If not mentioned otherwise, all the following figures in this chapter were created with the *firstEdepInVolume* condition. Data with *firstEdepInVolume* condition is shown in Fig. 6.2 and Fig. 6.3 for particle's ToA and type of particle respectively. After considering the deposited energy (by application of the *firstEdepInVolume* condition), the
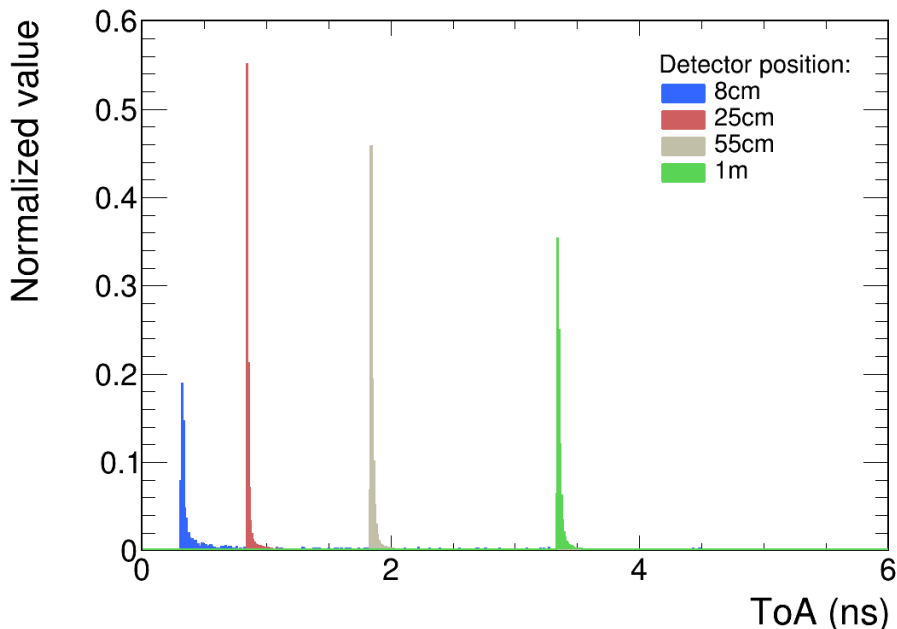
Figure 6.2: The ToA of particles that deposited energy in the detector (flag *firstEdepInVolume* is active). Each histogram is normalized to a number of respective entries.

significant contribution originates from electrons hitting the detector. Taking into consideration that in ERL operation mode, the S-DALINAC has a repetitive bunch rate of $6\,\mathrm{GHz}$, which corresponds to six peaks per nanosecond, a long tail can reduce the signal-to-noise ratio and have a significant impact on the detector performance. The same effect can be observed in the experiments discussed in Chapter 4 and Chapter 5 (Fig. 4.9 and Fig. 5.17), where all peaks were suitable on a continuous background. Understanding the origin of the tail is important for reaching the best possible detector time resolution.

To better understand the origin of the tail in the ToA spectra, one can take a look at the creation volume for each particle detected in the LGAD as shown in Fig. 6.4. As one can see in Fig. 6.4, the majority of particles were created in a vacuum (which is the primary particles only as the point source of electrons are put inside
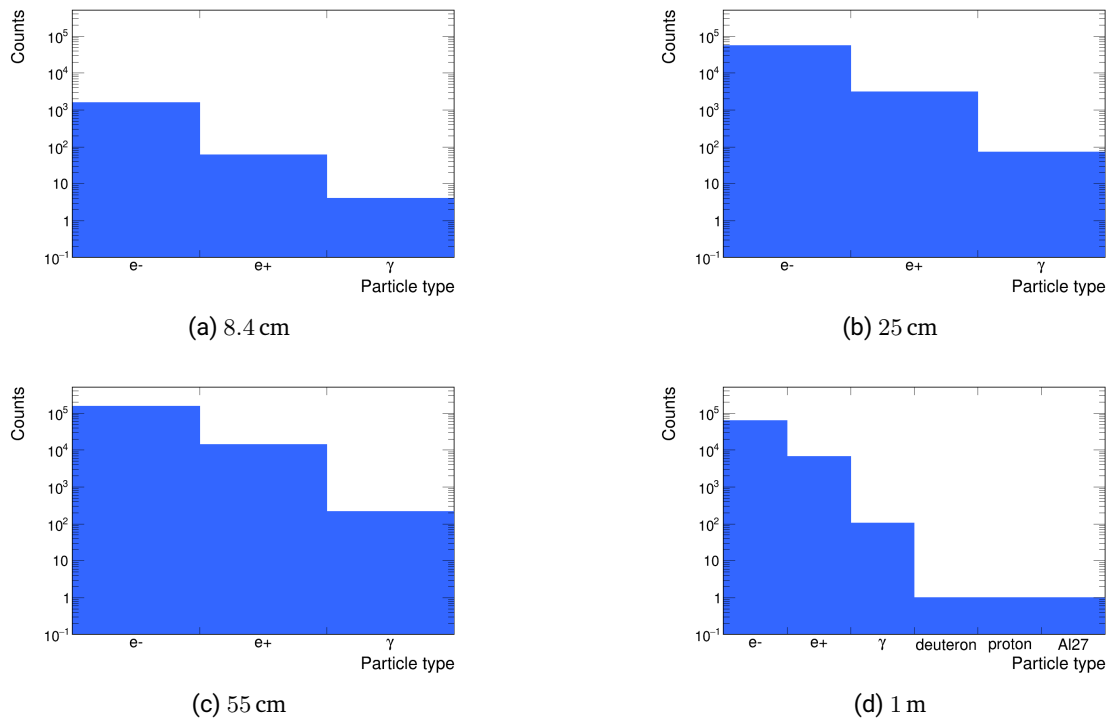
Figure 6.3: Type of particles that deposited energy in the detector. Data from hits that satisfy the *firstEdepIn-Volume* was used to create the plots.

the vacuum tube) or the beam pipe. The only exception is for the detector placed at $8.4\,\text{cm}$. In this case, the particles that were created in the wire or the air reach the detector. Additionally, the particles created in the detector itself should be excluded from the analysis. Electron-hole pairs, created in the detector by the incident particle, allow the detection of the incident particle (as discussed in Sec. 2.2.3). However, this study is focused on the ToA of the incident particles and does not include the detector response. The ToA of particles, created in different volumes except for the detector volume itself, are shown in Fig. 6.5. As shown in Fig. 6.5, the longest tail in the ToA spectrum has particles created in the air. However, these particles have a significantly smaller contribution to the total ToA, compared to the other particles, for all detector positions except the placement at $8.4\,\text{cm}$.

The primary particles (marked as "Vacuum" in Fig. 6.5) contribute the most to the detected hits at all positions except the closest one. The particles produced in the beam tube significantly contribute to the detector hits. On the other hand, for the position far enough from the wire scanner (which is true for the detector placement about $1\,\text{m}$ from the wire) no particles created in the wire reached the detector. This means that the secondary particles produced in the wire do not influence the detector.

6.2.2 Kinetic energy and momentum direction

An additional investigation was performed concerning the particles' kinetic energy and momentum direction, as it allows to better understand the interaction that particles experience and, consequently, the origin of the tail in the ToA spectra. Both of these parameters were taken from hits that satisfy the *firstEdepInVolume* condition. A momentum direction was used to calculate the hit angle of the particles with respect to the beam

(a) $8.4\,\mathrm{cm}$

(b) $25\,\mathrm{cm}$

(c) $55\,\mathrm{cm}$

(d) $1\,\mathrm{m}$
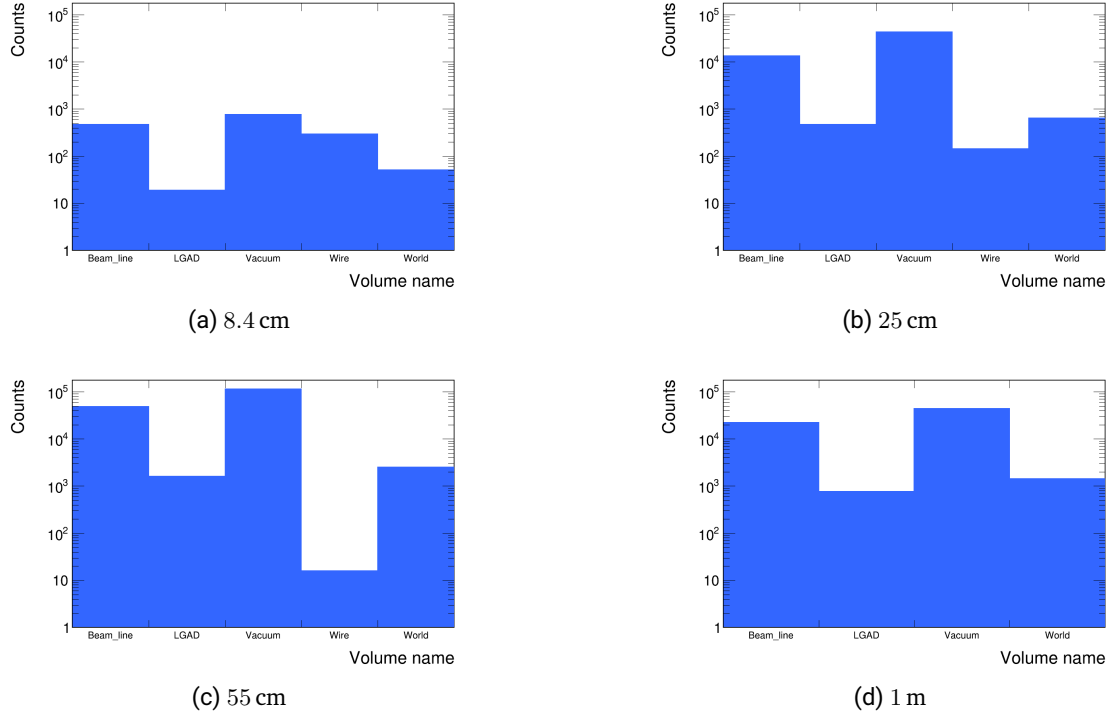
Figure 6.4: Creation volume name for particles that deposited energy in the detector.

axis as follows:

$$\text{Angle [degree]} = arccos\left(\frac{p_z}{\sqrt{p_x^2 + p_y^2 + p_z^2}}\right) \times 180/\pi, \tag{6.1}$$

where p_x, p_y and p_z are components of the particle momentum vector. Both the kinetic energy and momentum vector were taken from the first energy deposition step in the detector volume.

Figure 6.6 and Fig. 6.7 show the ToA distribution as a function of the particle's kinetic energy and hit angle, respectively. Both figures exhibit the particles that fulfill the *firstEdepInVolume* condition and are created in any medium except the detector itself (as defined and explained in Sec. 6.2.1). From Fig. 6.6, one can see that the ToA distribution is wider at lower particle energies than at higher energies. It comes from the fact that particles with lower kinetic energy undergo more interactions before being detected than those with higher energy. Figure 6.7 exhibits the particle's ToA as a function of the hit angle (Eq. 6.1). Comparing the number of entries below and above the $90°$, which represent hits from the front and back side of the detector, respectively, one can see that most particles hit the detector from the front side at all simulated detector positions. However, there is a larger number of higher ToA values that originate from the particles that hit the detector from the back side (a hit angle bigger than $90°$), which corresponds to the backscattering on the surrounding elements behind the detector, e.g. the iron vacuum tube. Introducing an additional cut on the entrance angle above $90°$ (for example, by placing the lead shielding behind the detector) allows rejection of backscattered particles and, consequently, reduction in the ToA tail as shown in Fig. 6.8

The number of particles depositing energy in the detector, peak-to-all entries ratio, and front hits ratio were used to estimate the detector performance. All of the mentioned parameters were calculated for the hits that satisfy the *firstEdepInVolume* condition. Additionally, the standard deviation was calculated for the ToA distribution in each detector position. Those parameters are summarised in Tab. 6.2.

(a) 8.4 cm

(b) 25 cm

(c) 55 cm

(d) 1 m
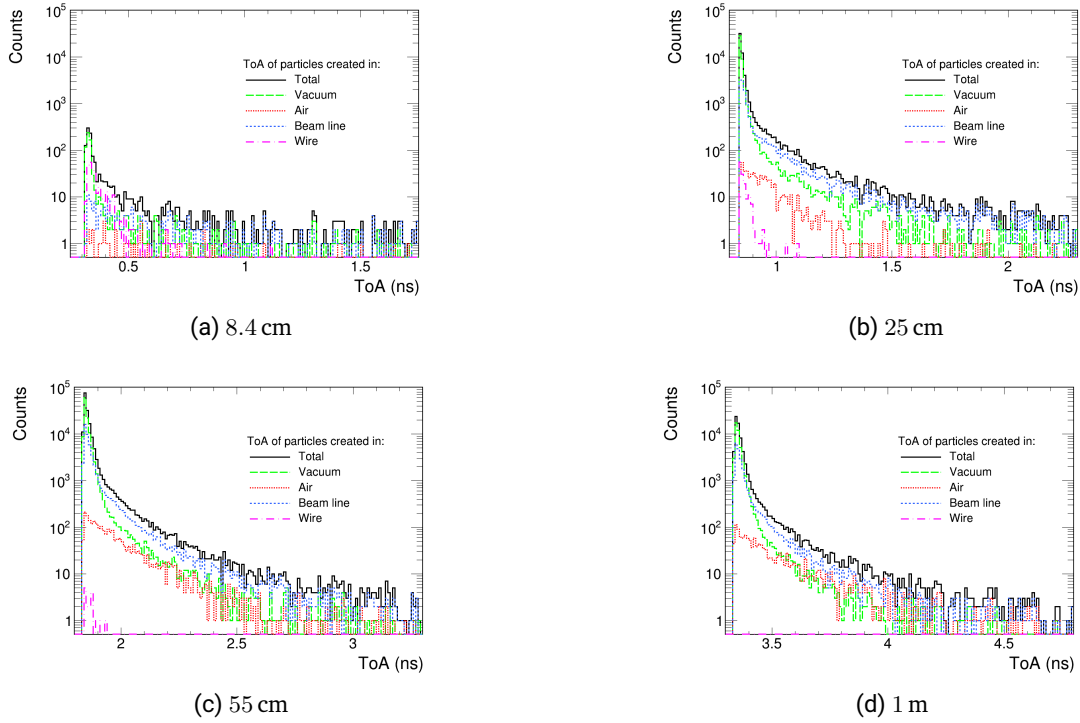
Figure 6.5: ToA of the particles, created in different volumes. The values normalized to the respective number of particles that deposited energy in the detector (Fig. 6.2).

Parameter	Detector position			
	8.4 cm	25 cm	55 cm	1 m
Number of particles that deposited energy in the detector	1 577	57 762	165 824	67 743
Front hits ratio	0.5	0.92	0.95	0.95
Peak ratio	0.19	0.55	0.46	0.35
Standard deviation of the ToA	1.1 ns	0.2 ns	0.1 ns	0.1 ns

Table 6.2: Summary of the Geant4 simulation results.

6.3 Discussion

The Geant4 simulation evaluated the possibility of an LGAD application at S-DALINAC in ERL mode and estimated the LGAD performance. It has to be mentioned that the simplified geometry of the recirculation beamline and the detector itself was implemented. Also, only different detector positions were simulated. Additional rotation or other adjustments may be needed to increase the detector performance during the experiment. The following criteria were used to judge the detector performance: number of particles depositing energy in the detector, peak-to-all entries ratio, and front hits ratio. Those criteria are summarised in Tab. 6.2.

Considering all the parameters in Tab. 6.2, the placement of the LGAD at 55 cm, which corresponds to 50 cm away from the wire, is the best in terms of all considered parameters. Placing the detector too close to the wire leads to a negligibly small amount of detected hits. Also, a too close placement of the detector leads to a long tail in the ToA spectrum and a considerable amount of backscattered particles hitting the detector.

(a) 8.4 cm

(b) 25 cm

(c) 55 cm

(d) 1 m
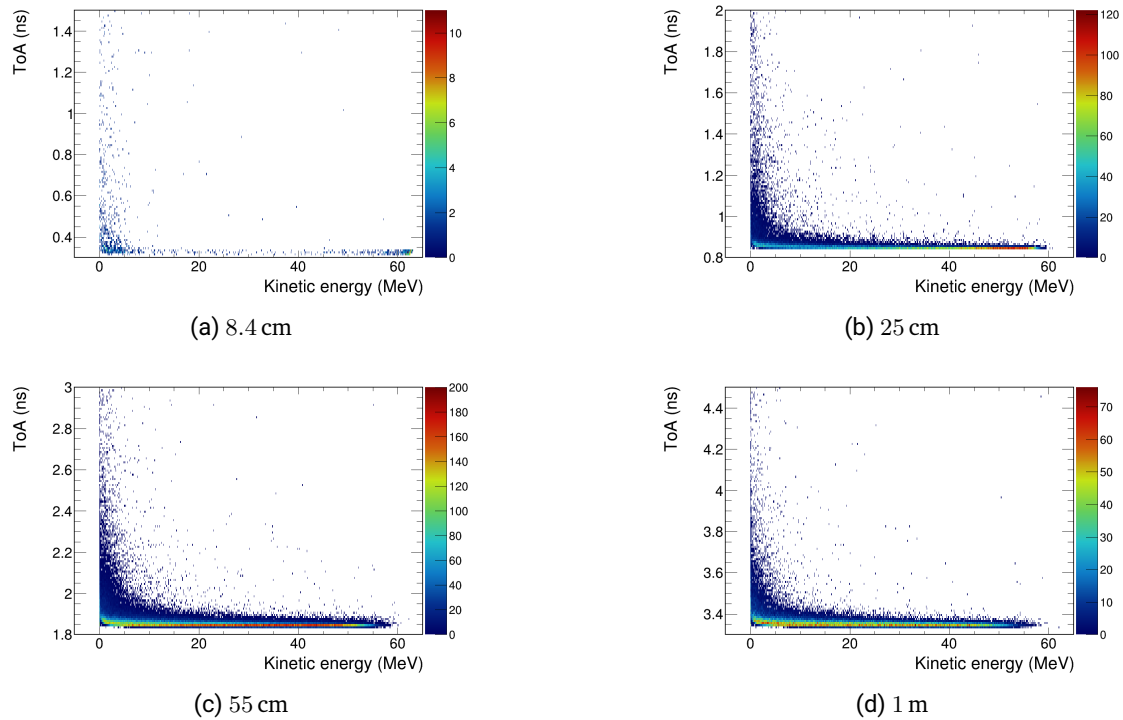
Figure 6.6: ToA of the particle as a function of its hit angle.

All other positions are almost identical in terms of the front hits ratio and peak ratio. However, the number of detected particles is different in these positions. Moving the detector away from the wire allows it to detect more particles. But at some point, the number of detected particles starts to decrease. As was mentioned before, placement of the detector 50 cm away from the wire seems to be the best from the simulation point of view. The surrounding infrastructure should be considered, and additional detector placement adjustments may be needed during the experiment.

Additionally, a high background is expected in the experimental hall which was not yet included in the simulation. In 2021, a wire scanner measurement was conducted with a scintillating detector placed outside of the beamline [24]. The conditions of this experiment are close to those that the LGAD will be placed in. The background rate from this experiment can be estimated at 1 MHz. The scintillating detector size was 4 cm×4 cm with the wire scanner velocity about 6.2 mm/s [65]. Assuming the constant background rates at 1 MHz and taking into consideration the LGAD size of 1 cm×1 cm with 86 strips, the expected background rate for the measurements with LGAD is 62.5 kHz per sensor and about 700 Hz per strip. Much higher rates were observed during the experiments, described in Chapter 4 and Chapter 5, which indicates that the background in the experimental hall should not disrupt the LGAD performance.

(a) $8.4\,\mathrm{cm}$

(b) $25\,\mathrm{cm}$

(c) $55\,\mathrm{cm}$

(d) $1\,\mathrm{m}$
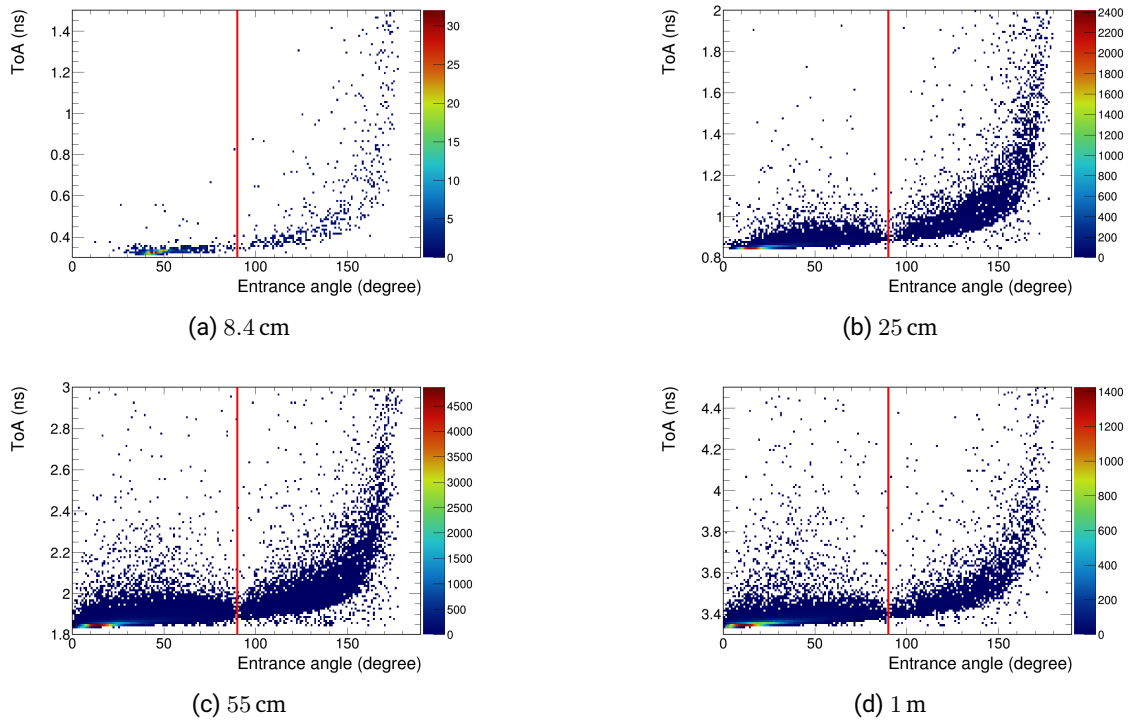
Figure 6.7: ToA of the particle as a function of its hit angle. The red line represents the $90°$ angle and separates front hits (to the left of the line) and back hits (to the right of the line).
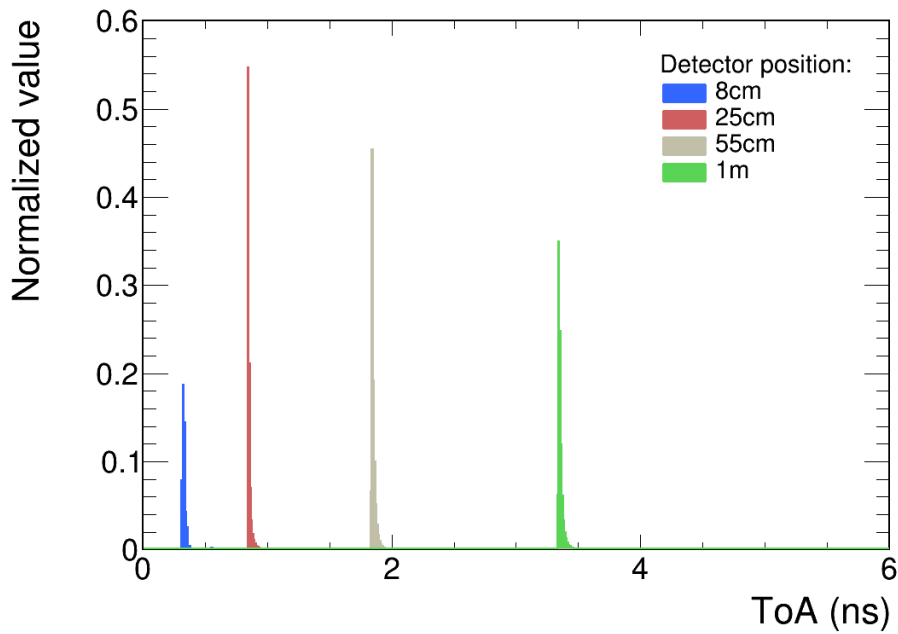
Figure 6.8: The ToA of particles deposited energy in the detector with a hit angle cut (back hits are rejected). Each histogram is normalized to a number of respective entries.

7 Machine learning application for LGAD corrections

In recent years, the field of machine learning (ML) in particular and the artificial intelligence (AI) in general have undergone rapid development and growth. They are widely used in different fields, including physics [66]. In this chapter, a feasibility study of an ML application for LGAD corrections will be presented.

ML algorithms provide the opportunity to describe a large data set utilizing a small subset of this data. These algorithms can find a correlation in the small data subset and apply it to the larger one. The idea behind the ML approach for the LGADs is to have an online calibration procedure. For this the following requirements should be fulfilled:

- Fast procedure to perform calibration online, i.e. during the data taking.

- Scalable algorithms that allow easy extension to a bigger system.

- Data instability detection and correction parameters recalculation if needed.

An artificial neural network (ANN or NN) was considered a suitable algorithm for this task. The goal was to evaluate the feasibility and performance of an NN (or any other suitable ML algorithm) for an LGAD correction. The ML approach was tested on the data, presented in [7] for an LGAD application in the HADES experiment at GSI [67].

7.1 Experimental setup

A detailed description of the setup and analysis is given in [7]. This section briefly summarizes the geometry of the setup, the calibration and analysis steps performed in [7]. The setup described in [7] consisted of two LGAD strip sensors arranged orthogonally to each other. Two read-out systems were employed. One was based on the NINO chip [68], and the other was based on the PaDiWa board (introduced in Chapter 4). The experiment was performed at the COSY facility in Juelich, Germany, utilizing a 1.92 GeV proton beam [7]. Data from the NINO-based boards were used in this analysis. The setup scheme is shown in Fig. 7.1a.

Using the previously described detector design, the ToA and ToT of protons passing through LGADs were recorded and the corresponding time difference between hits in two sensors was calculated. The resulting time difference spectrum is shown in Fig. 7.1b with respect to the ToT of the signal measured inside the first LGAD. Additionally, Fig. 7.1b exhibits a strong time walk effect, indicated by the red markers.

As discussed previously in Sec. 3.3.2 and Sec. 5.2.2, the time walk correction is crucial for achieving the best possible timing precision. A detailed description of all performed calibration and analysis steps is given in [7]. All of these steps were performed offline and required a significant amount of data.

7.2 Machine learning algorithm selection

The goal of any ML algorithm is to find a relation and establish a correlation pattern in a given dataset [66]. A dataset that contains a solution to the given problem is called a *labeled* dataset. The dataset is *unlabeled* if a solution is unknown. Based on the type of dataset used to train the model, four different types of algorithms for model training (or learning) are considered [69]:
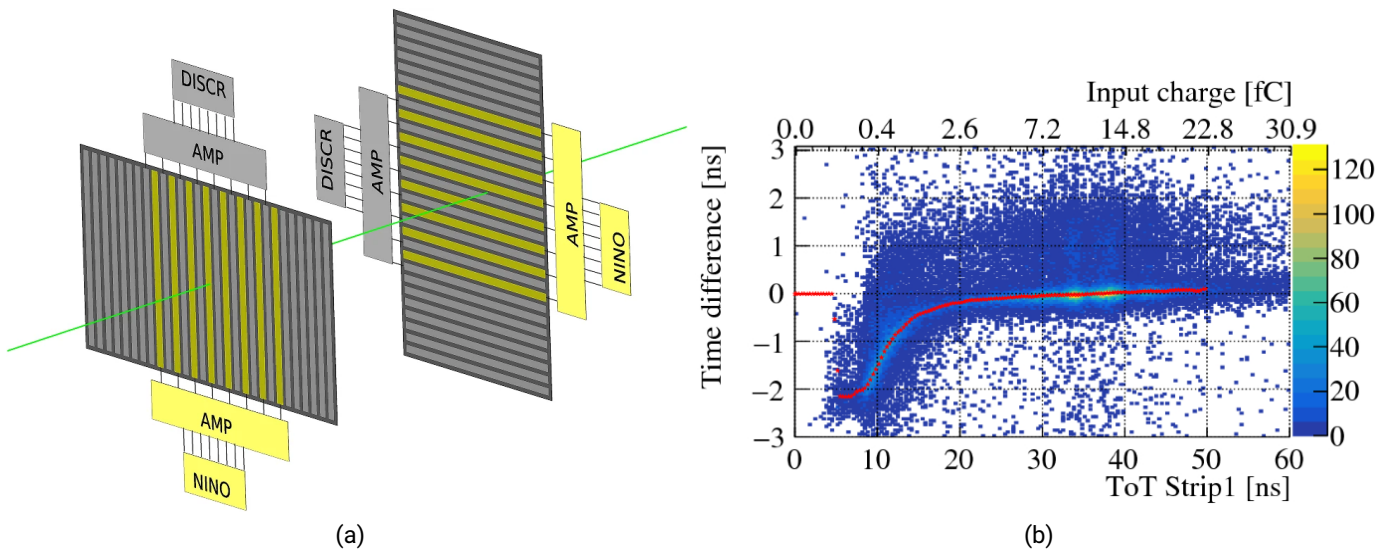
Figure 7.1: Overview of the analysis related to data in this chapter. (a) shows the experimental setup scheme. Data from the channels connected to the NINO-based (marked with yellow) boards were in the analysis presented in this chapter. (b) shows the time walk effect for a selected channel pair(red markers represent the time walk correction parameters produced during an offline analysis). Both plots taken from [7].

- Supervised learning: a labeled dataset is provided as an input for an ML algorithm and a relation between data points and their respective labels is established.

- Unsupervised learning: an unlabeled dataset is given to an ML algorithm, and the algorithm establishes any similarities in the dataset without providing answers.

- Semi-supervised learning: a mix of supervised and unsupervised learning when a part of the provided dataset is labeled.

- Reinforcement learning: these algorithms are helpful in situations when an external environment should be considered to achieve the desirable outcome.

Typical tasks for the ML include but are not limited to regression, clustering, and classification [70]. In the scope of this work, regression analysis with supervised learning was chosen as the main task.

7.2.1 Automated machine learning approach

The term "machine learning" includes a range of different algorithms. Selecting and optimizing a proper algorithm can be a complex task. In recent years, the so-called *automated machine learning* (AutoML) approach was developed to reduce the effort and complexity of applying ML algorithms and to make ML more accessible to a broader field of potential users [71]. Each ML algorithm has so-called *hyperparameters*, which are a set of parameters that define the learning process of the model and do not change during this training. The number of layers and their size in the NN are examples of hyperparameters. One of the main tasks of AutoML is a hyperparameter optimization (HPO), which allows the selection of the most suitable hyperparameters for a given ML algorithm and problem [71]. Another feature of the AutoML is a so-called *meta-learning*, which speeds up the development by using the meta-data about the performance of different ML algorithms for a given problem [72]. The workflow of the AutoML is shown in Fig. 7.2. The leftmost box in this figure
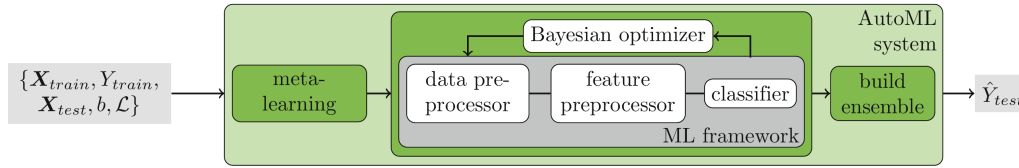
Figure 7.2: AutoML workflow. Taken from [73].

represents the data defined by the user, namely the training and validation datasets. These datasets are used by the AutoML system (represented by a light green box) to find the most suitable algorithm and its parameters utilizing the aforementioned meta-learning and HPO. As a result, an ML model optimized for the given problem is created.

The main goal of the training is to obtain a model that can make a prediction based on new data that it was not trained on. However, the quality of the training and, consequently, the ability to make a correct prediction depends on many parameters and is not guaranteed. It is crucial to control the training results as *underfitting* or *overfitting* can occur [74]. Underfitting means that the model is not able to describe the data. In the case of overfitting, a model can predict the training data very well; however, it is not working well on new data. To avoid overfitting and underfitting in this work, the AutoML approach was used as described above.

7.2.2 AutoML algorithm selection

Before selecting the ML algorithm, the structure of the model should be decided. A suitable model for the time walk correction should be able to predict the time difference based on the ToT of the signal to estimate the time walk trend. Two possible models can be created. One option is to create one model per sensor that will include parameters for all channels and can be described by the following function

$$\text{time difference} = f(ToT, \text{detector channel}). \tag{7.1}$$

The other option is to use a model that will describe only one channel in the system as a function of the signal amplitude

$$\text{time difference} = f(ToT). \tag{7.2}$$

Comparing Eq. 7.1 and Eq. 7.2 it is clear that the first model will require more input parameters compared to the other one, where the only input parameter is signal ToT. Consequently, the first model should have a more complicated architecture and contain more parameters to correctly describe all channels in the whole sensor compared to the second model which should describe only one channel. The large amount of parameters directly affects both the training time and the amount of data needed for the training. In case of changes in only one channel ToT (for example, due to radiation damage), the whole model has to be re-trained. In the case of the second model, one model has to be trained for each channel in the system. Having many small models compared to one model that describes a whole system comes with several advantages. Firstly, the training time and amount of training data are reduced compared to the bigger model defined by Eq. 7.1. Secondly, in the case of ToT changes in the given channel in the system, only one model that describes this channel has to be re-trained while the models for other channels are unaffected. Lastly, the models defined by Eq. 7.2 can be trained in parallel, speeding up the training process.

To find an optimal algorithm and to optimize its parameters, Auto-Sklean [75] and AutoKeras [76] systems were used to verify the ML algorithm selection. The AutoKeras system was chosen because the Tensorflow framework [77] was planned to be used for ML applications in this work, which also features Keras library

[78]. As a training data set, 10^4 data points from the experiment were used for a given channel. This data set was split into training and validation data with ratio $80\,\%{:}20\,\%$. The different data set for validation was used to ensure that the model predicted the pattern not only on the training dataset but also on completely new data. The mean absolute error (MAE) was used as a loss function, which calculates as follows

$$MAE = \frac{1}{N} \sum_{i=1}^{N} y_{training} - y_{predicted}, \tag{7.3}$$

where $y_{training}$ is a training value, $y_{predicted}$ is a value predicted by an ML model, and N is the dataset size. AutoKeras was optimizing the validation losses, meaning that the model that performed best on the validation dataset was selected. The total time for the search for a suitable algorithm was limited to one hour, with a maximum of 100 models tested. Those 100 models include different algorithms and hyperparameters. The best model, according to AutoKeras, is a neural network, which will be introduced next. The respective parameters are given in Tab. 7.1.

7.2.3 Neural network overview

The main idea behind NNs is to imitate the human brain [69]. There are many different types of NNs [79], but all of them consist of artificial neurons (by analogy to human neurons) organized into layers. The simplest form of NN is a perceptron with only two layers: input and output. A more complex NN is shown in Fig. 7.3. In this case, NN has three layers, namely an input layer, which consists of two input parameters (x_1 and x_2), a
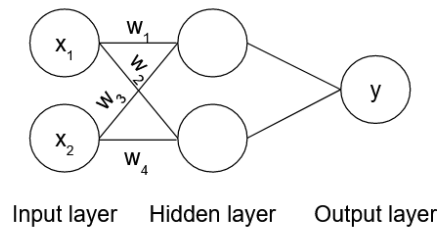
Figure 7.3: Scheme of a simple NN with one hidden layer. x_i represents an input data, w_i represents the weights, and y is the output.

hidden layer to process the inputs, and an output layer with one feature (y). If data is passed from the input to the output layer, the NN is called a *feed-forward NN*. Adding additional hidden layers will transform the NN into a deep NN (DNN). Those hidden layers allow to recognise not only linear relations in the data but also more complex ones. The given NN is a fully connected NN as all neurons in the previous layer are connected to all neurons in the next layer.

According to [74], the propagation is done in two steps, namely preactivation and activation. During the preactivation step, a weighted sum of a neuron's input data is calculated as follows [74]:

$$a = \sum_i x_i * w_i + b,$$

where a is the preactivation parameter, x_i is the input data, w_i is the weight and b represents the bias. The preactivation parameter is used to calculate the output of the respective neuron, which will be passed to the following layer using the activation function.

7.3 Neural network based corrections results

7.3.1 Created neural network

As described in Sec. 7.2.2, the most suitable algorithm was selected using the AutoML approach. An NN was built according to the parameters in Tab. 7.1. First, the AutoML system used data from one channel for

Parameter	Value
Algorithm	NN
Number of training steps	100
Optimizer algorithm	Adam
Learning rate	0.00015
Number of hidden layers	2
Number of neurons per layer	48
Activation function	ReLU (Eq. 7.4)
Loss function	MAE

Table 7.1: Parameters of the best model according to AutoML.

training, and the same NN architecture was subsequently used for all models created for each channel in the system. It is not guaranteed that the saved weights in the trained model will fit for other channels as it was trained for the particular one. Consequently, to obtain the best possible prediction each model has to be trained on the dataset from the particular channel. Because of this, the AutoML system output was used to obtain the NN hyperparameters only and each NN was trained separately. After that, a code that allows the training of different NNs with the same architecture was developed, and a separate NN was trained for each channel to describe the pattern in this particular channel. The NNs were built using Tensorflow version 2.3.1. Those NNs utilize an MAE defined by Eq. 7.3 as a loss function.

As an activation function, a rectified linear unit (ReLU) was used. This function is defined as follows:

$$\text{ReLU}(x) = \begin{cases} x \text{ if } x \geq 0, \\ 0 \text{ if } x < 0. \end{cases} \tag{7.4}$$

During the training, the weights of the NN are optimized to minimize the loss function. To achieve this, a special minimization algorithm is applied, which is called *optimizer*. A gradient descent algorithm or its variations are generally used [80]. An Adam algorithm was used as an optimizer. This method "uses the estimation of the first and second moment of the gradient by exponential moving averages and then apply some bias corrections" [80, p.103].

Additionally, a normalization layer was added to the network after the input node. This layer transforms the input data into a distribution centered at 0 with a standard deviation of 1 as follows [81]:

$$\text{input}_{\text{normalized}} = \frac{\text{input} - \text{mean}}{\sqrt{\text{standart deviation}}}.$$

In general, normalization of the input data increases the performance of a NN and allows faster learning. Additionally, it makes the model less sensitive to the outliers in the data.

7.3.2 Neural network training

As mentioned in Sec. 7.3.1, models that predict the time difference based on the signal ToT were created. For that purpose, the time difference was calculated between two hits in two detectors for the selected channel pair, which also means that the model is only valid for the given pair. In case the channel combination changes, the model needs to be re-trained. Additionally, to perform a time difference correction alongside a time walk, all channels in the same sensor were correlated with the same channel in the other sensor (as discussed in Sec. 5.2.6). In total, sixteen NNs were necessary to perform the time walk and time difference correction of the system described in Sec. 7.1. In the case of this analysis, these NNs were trained consecutively, which took about $640\,$s. Running all training processes in parallel on a dedicated high-performance CPU or GPU machine would further increase the speed of the training process. The training speed is important for the online application. However, for demonstration purposes, consecutive training of the models was chosen as it allows faster software development.

As mentioned in Sec. 7.2.2, all NNs were trained on a data set with 10^4 time difference and ToT pairs for each channel pair, which were split into training and validation data sets with ratio $80\,\%$:$20\,\%$ respectively. An additional cut on the ToT of the correlated hit was introduced to exclude signals that originate from noise or capacitive coupling. The result of the training procedure for two selected channel pairs is exhibited in Fig. 7.4. As one can see in Fig. 7.4, the NNs perform well in both cases with the obtained MAE ranging from
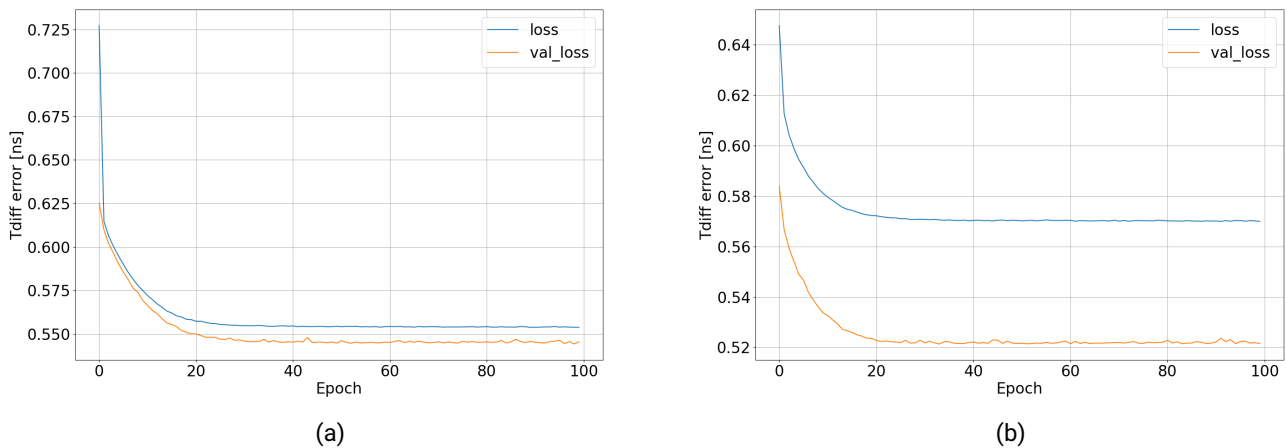
Figure 7.4: Illustration of the NN training process for two selected channel pairs. (a) shows the time difference between hits in channel 3 of the first sensor and in channel 3 of the second sensor as a function of the hit ToT in the first sensor, and (b) shows the same time difference as a function of ToT in the second sensor. The blue lines represent the training losses and the orange lines represent the validation losses. The MAE is used as a loss function. The X-axis represents the training step.

$0.5\,$ns to $0.6\,$ns. After the 20th epoch (or training step), the validation and training losses do not change significantly, which indicates that a reduced number of training steps could have been used to achieve a similar performance.

After the training procedure, for each channel, the time walk correction parameters were produced for a ToT range of $0\,$ns to $50\,$ns with a granularity of 10^4 points per $1\,$ns. Figure 7.5 shows the NN's prediction of the time walk trend in channel 3 of the first and second sensors. The time difference was calculated between hits in those channels. As shown in Fig. 7.5, for the given channel pair, the NN prediction is in good agreement with the training data. In the low ToT region, the NN prediction is unreliable due to an insufficient amount of
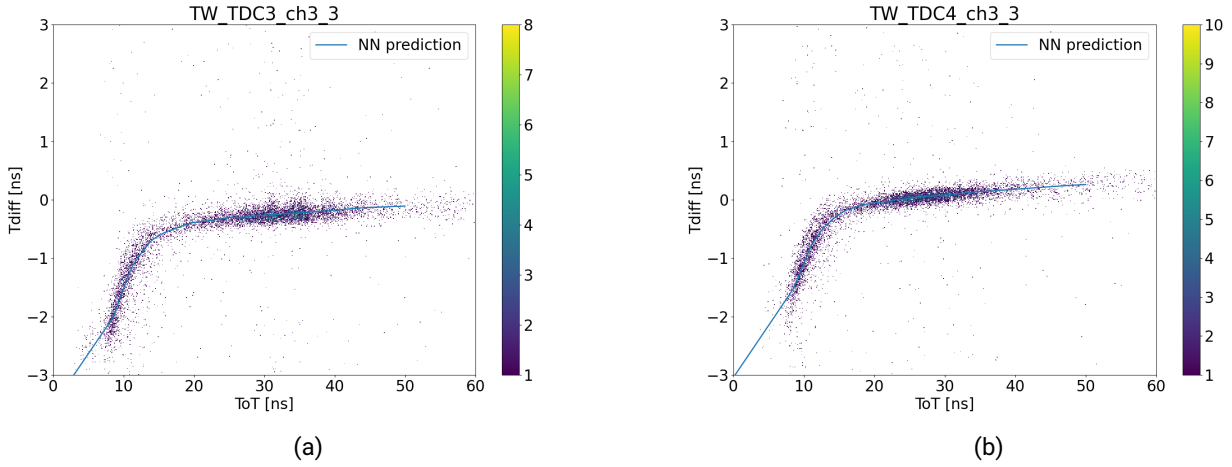
Figure 7.5: The NN time walk parameters compared to the training data for the given channel pair. (a) shows the time difference between hits in channel 3 of the first sensor and in channel 3 of the second sensor as a function of the hit ToT in the first sensor, and (b) shows the same time difference as a function of ToT in the second sensor. The blue lines represent the NN prediction, and the points represent the training data.

data in this region. However, this still didn't affect the time walk trend estimation as the absence of data in this ToT region was expected due to the electronics used in [7].

7.3.3 The time walk and time difference parameters calculation

As was mentioned in the previous section, after the NN training, the correction parameters were produced for each channel in the detector system. These sets of parameters were produced in a way that corrects for both time walk and time difference effects. For the time difference correction, one of the channels in each sensor was selected as a reference, and all channels in other sensors were correlated with this one. For the time walk correction, the NN prediction of the time difference based on ToT was used for each channel. The schematic of the correction parameters calculation is shown in Fig. 7.6.

As mentioned before, NNs were trained for each channel in the sensor correlated to the reference channel in another sensor to calculate correction parameters. First, the time walk correction parameters were calculated. A reference ToT value was selected for this, and the corresponding time difference NN prediction was used. For each ToT value, the corresponding time difference was shifted to the reference time difference value as follows:

$$\text{TW correction parameter} = \text{reference time difference value} - \text{time difference value}.$$

The time difference correction was done in two steps. In the first step, the reference time difference for each channel was shifted to zero value as follows:

$$\text{time difference correction parameter}_{\text{second sensor}} = 0 - \text{reference time difference value} =$$
$$= -\text{reference time difference value}. \tag{7.5}$$

However, as the NNs for the second sensors were trained on the raw data, the reference time difference values do not include the shift of the first sensor. Shifting the values to zero as in Eq. 7.5 will lead to an additional
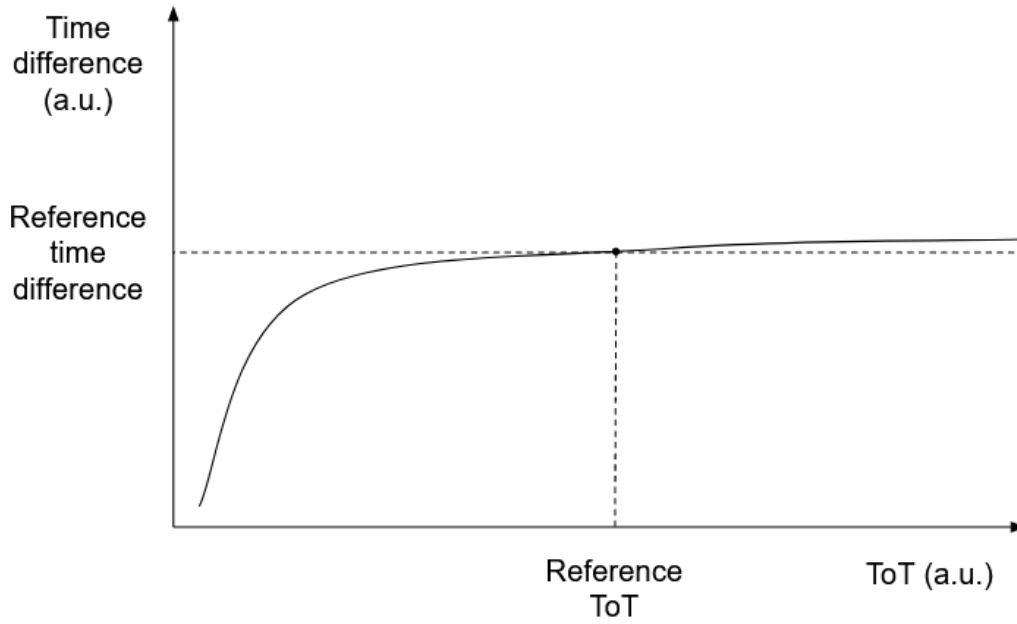
Figure 7.6: Scheme of correction parameters calculation. Reference ToT and time difference values are described in the text. The solid line represents the time difference prediction made by NN.

shift from zero time difference values for both sensors. To account for the time difference shift in the first sensor, the time difference correction parameters for the second sensor were calculated as follows:

$$\text{time difference correction parameter}_{\text{second sensor}} =$$
$$= \text{time difference correction}_{\text{first sensor}} - \text{reference time difference value}.$$

7.3.4 Neural network-based time walk correction result

The detailed conventional analysis discussion is given in [7] and [58]. In this section, a comparison of conventional and NN-based correction methods is given with a focus on NN-based correction.

The time difference effect is illustrated in Fig. 7.7a and the time walk is shown in Fig. 7.7b. As shown in Fig. 7.7a, each channel has an offset for the ToA that should be corrected. The strong dependence of the time difference based on hit ToT (especially in low ToT region) is exhibited in Fig. 7.7b. The time difference effect can be seen in Fig. 7.7b also, as the main signal in this plot (which is at $35\,\text{ns}$) is not at $0\,\text{ns}$ time difference value.

The results of both time difference and time walk corrections using the parameters produced by NNs as described in Sec. 7.3.3 are shown in Fig. 7.8 for the same data as in Fig. 7.7. As one can see from Fig. 7.8a, for all channels, the time difference value is at zero, which indicates that the time difference correction was done properly. Figure 7.8b illustrates the result of the time walk correction. No time difference dependence on the hit ToT is apparent, which indicates that the time walk correction was successful.

After the NN-based corrections, the final time resolution of the sensors was calculated. This was done by projection the data from Fig. 7.8a on the time difference axis on a channel-by-channel basis. In the next step, the obtained distribution was fit with a Gaussian function. The mean value of this fit was used as a MPV for the time resolution of a given channel. The time resolution of both sensors with the NN-based corrections is shown in Fig. 7.9. The obtained sensors' time resolution obtained using the NN-based correction approach is $67.31\,\text{ps}/\sqrt{2} = 49.7\,\text{ps}$. The time resolution, reported in [7], was $47.2\,\text{ps}$. The performance of the ML-based

(a)

(b)
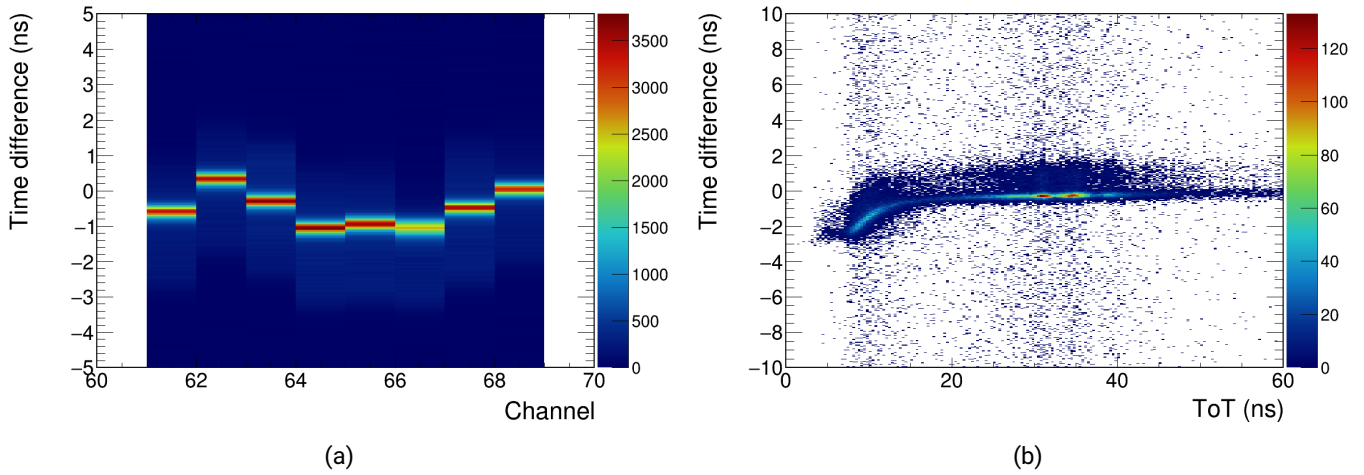
Figure 7.7: Time difference and time walk effects illustration. (a) exhibits the time difference between hits in the second sensor correlated with hits in channel 3 of the first sensor. (b) exhibits the time walk effect for channel 3 of the first sensor correlated with channel 3 of the second sensor.

(a)

(b)
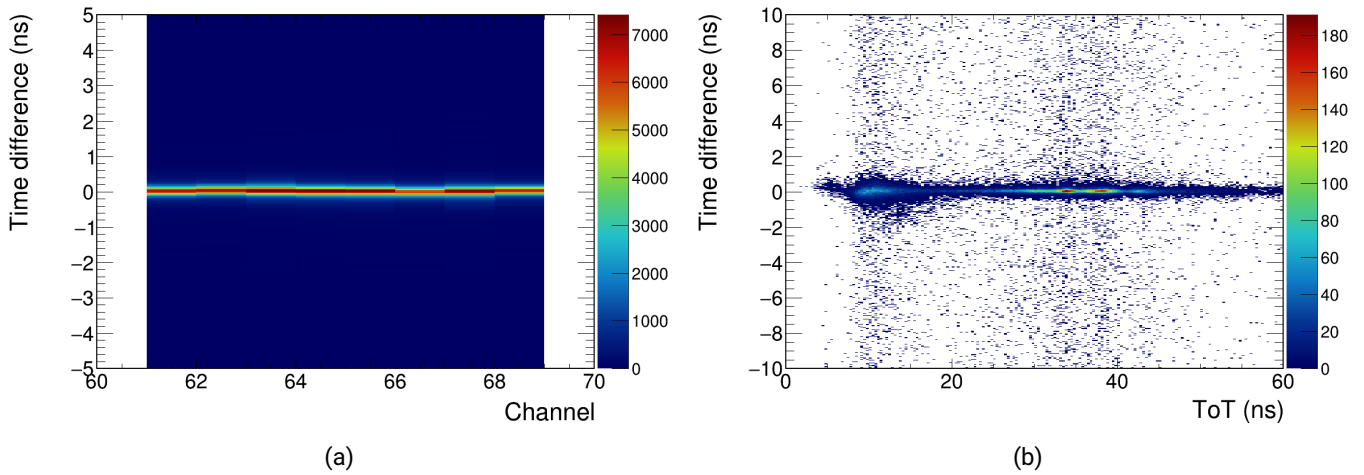
Figure 7.8: Result of the time difference and the time walk corrections. (a) exhibits the time difference between hits in the second sensor correlated with hits in channel 3 of the first sensor. (b) exhibits the time difference between hits in channel 3 of the first sensor and hits in channel 3 of the second sensor as a function of each hit's ToT in the first sensor.

and the conventional corrections are the same within uncertainties, with the conventional approach being marginally better. However, further investigation on possible NN architecture optimization to match the performance of the conventional correction approach is possible.

7.3.5 Neural network-based correction comparison to the conventional approach

To compare the NN-based and conventional approach, the time walk correction was performed using the conventional approach described in [7] with 10^4 data points used for the NNs training. The raw data are
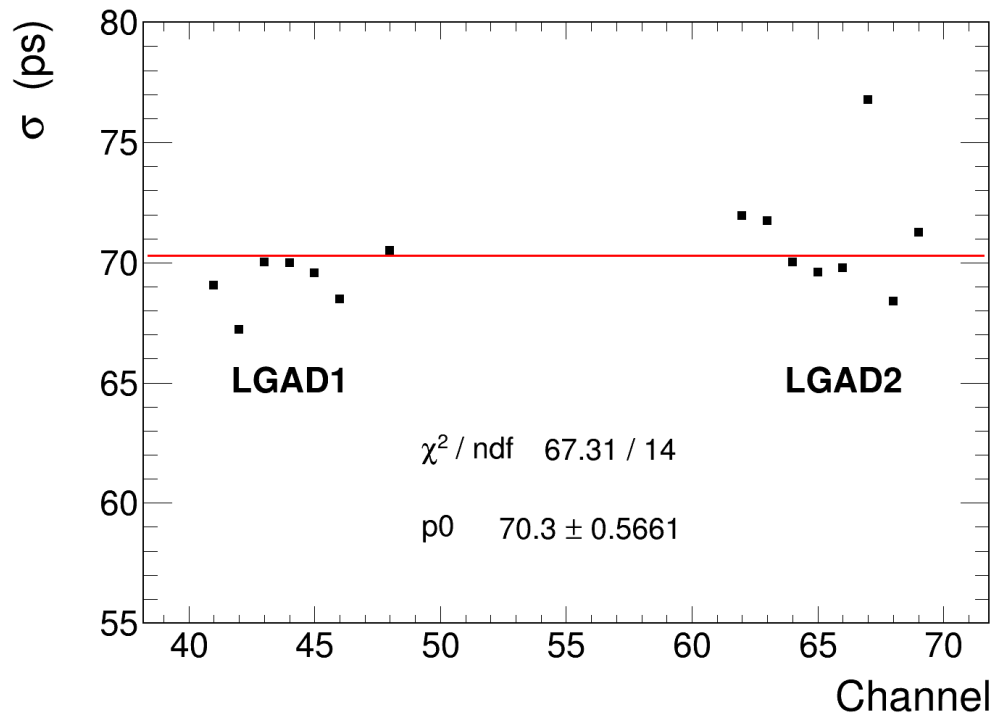
Figure 7.9: The time precision of both sensors obtained with the NN-based approaches to corrections.

shown in Fig. 7.10a. A projection on the time difference axis for each ToT bin in Fig. 7.10a was made to

(a)

(b)
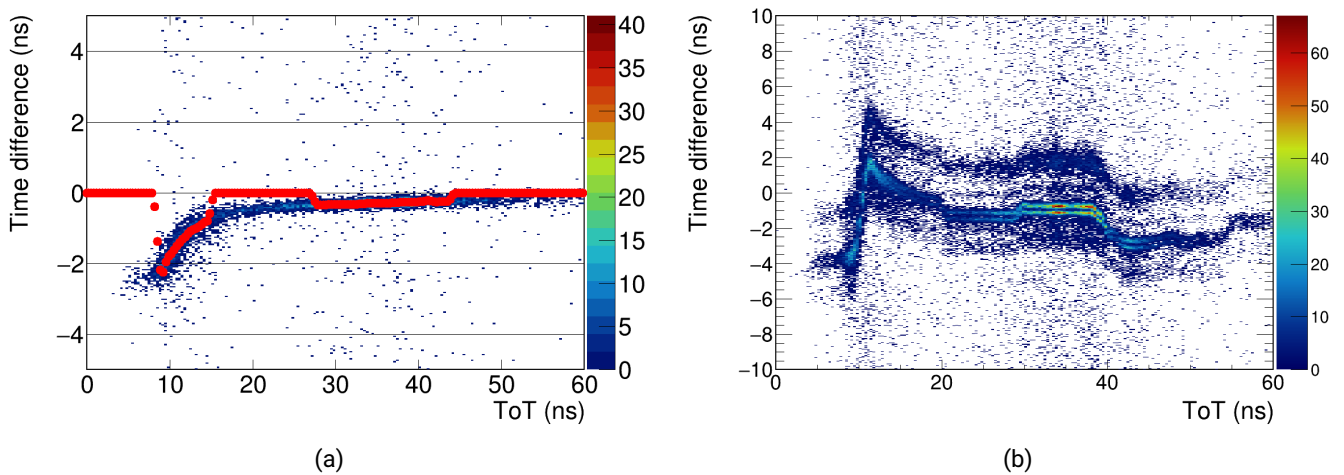
Figure 7.10: Results of the conventional time walk calibration with 10^4 data points. (a) exhibits the raw time difference between hits in channel 3 of the first sensor and hits in channel 3 of the second sensor as a function of each hit's ToT in the first sensor. Red dots mark time walk correction parameters obtained using the conventional approach. (b) exhibits the results of the time walk correction in both sensors.

produce the time walk calibration parameters. In the next step, the Gaussian fit was performed to obtain the

MPV of the time difference. The MPV is used as a correction parameter for the respective bin. The results of this procedure are shown in Fig. 7.10a with red markers. As one can see from this figure, the procedure works for the main signal region and low ToT region. However, two more regions are not calibrated due to the low amount of data in those bins.

The time walk calibrated data are shown in Fig. 7.10b. As one can see, the main signal ToT between $30\,\mathrm{ns}$ and $40\,\mathrm{ns}$ is appropriately corrected. The low ToT region is overcorrected, which indicates that the produced time walk calibration parameters are incorrect. However, compared to Fig. 7.8b, one can see that data is not corrected in the full range. The data presented in Fig. 7.10b cannot be used for further analysis due to failed time walk correction. Consequently, more data is required to perform the time walk correction using the conventional approach.

Comparing the results of NN-based and conventional time walk calibration, the main advantage of the ML approach is highlighted. The NN-based approach requires less data as it allows the prediction of the time difference based on a smaller dataset, subsequently allowing faster calibration.

7.4 Summary

This section demonstrated the feasibility of an ML algorithm application for a time difference and time walk correction procedure for an LGAD-based detector system. It was decided to train a separate model for each channel rather than one for the whole system due to speed efficiency and the possibility of independent and parallel training (or retraining when needed) of each model. An AutoML approach was used for algorithm selection and hyperparameter optimization. According to AutoML, the artificial neural network was the most suitable for the task.

The created NNs, their training performance, and prediction results were discussed. The NN prediction of the time difference for each channel in the system was used to calculate the correction parameters. The NN-based time difference correction was successful. The time walk correction based on NN prediction adequately corrects the data. It allows for reaching the marginally the same time performance of the system compared to the conventional approach to the time walk and the time difference corrections. Also, it was demonstrated that applying the ML algorithms allows the corrections mentioned above to be done faster due to a smaller amount of data required compared to the conventional approach, making it a suitable candidate for the online correction system.

The general feasibility of an ML application for an LGAD time walk and time difference correction was demonstrated. In case of any changes to the system, read-out electronics or the structure of the data, a new evaluation of the best suitable algorithm should be done. The ML-based LGAD calibration is planned to be implemented for future LGAD applications in the HADES experiment and to be performed during the data taking.

8 Summary and outlook

This work aimed to develop a non-destructive system for beam time structure monitoring purposes for the S-DALINAC. This system should be able to resolve the 6 GHz time structure of the S-DALINAC beam and allow bunch-to-bunch measurements. Pairing such a system with an already existing wire scanner for beam position monitoring would allow the simultaneous determination of the beam position and phase.

In the scope of this work, a test setup based on novel ultra-fast silicon sensors, so-called LGADs, was prepared. The LGADs were developed for simultaneous precise position and time measurement, which enables four-dimensional tracking. A timing resolution for an LGAD below 50 ps was demonstrated, which makes LGAD-based detectors excellent candidates for the beam time structure monitoring at the S-DALINAC. This setup employs a custom readout system based on leading-edge discriminators and FPGA-based TDCs to measure the ToT and ToA of the signals generated by the detected electrons. Each signal generated in the detector was compared to the constant threshold voltage. The time of crossing the threshold of rising and falling edges for each signal was recorded. The ToT was calculated as the difference between those values and the time of the rising edge was used as a ToA.

To demonstrate the feasibility of an LGAD application for beam time structure monitoring, the simplified setup was prepared. This setup consisted of a single LGAD sensor with several active channels. During the experiment, the 3 GHz beam time structure at the S-DALINAC was resolved, which makes it the first successful measurement of such a structure and demonstrates the feasibility of an LGAD application as a monitoring tool. However, due to a low number of active channels, this setup cannot be used as a permanent solution.

An upgraded setup was prepared to demonstrate the system's performance. The upgraded system employed two LGAD sensors, which were fully read-out. During the experiment in the conventional operation mode of the S-DALINAC, the 3 GHz beam time structure was successfully resolved with the best reached time precision of the system of 79 ps. The corresponding necessary corrections were developed and discussed in detail to reach the best possible time resolution and resolve the beam time structure. However, experimentally, the possibility of resolving the beam time in the ERL mode with 6 GHz was not demonstrated. It has to be mentioned that the demonstrated time resolution of 79 ps is not optimal and may not be sufficient for the operation in ERL mode. However, the time resolution below 50 ps was already demonstrated within the author's working group. Additionally, development of an ASIC/FPGA-based read-out system for an LGAD is ongoing, which will allow for reaching the ultimate LGAD time resolution and, subsequently, increase the performance in the ERL mode.

The feasibility study of the LGAD-based setup in the S-DALINAC ERL modes was performed utilizing a simulation based on Geant4 software. The simplified geometry of the S-DALINAC recirculation beamline was created. Additionally, only the physical response of the detector was simulated without the read-out electronics included. This simulation demonstrated the feasibility of using the LGAD-based setup to monitor the S-DALINAC beam with 6 GHz time structure. The simulation was used to determine the best position for the detector placement. However, no additional infrastructure present in the accelerator hall was simulated. Its influence on the detector performance will require further investigation. Since no infrastructure was simulated, the background was estimated from the wire scanner measurement. The present background in the accelerator is expected to be within the capabilities of the current LGAD system and should have no significant influence on the detector's performance.

Lastly, the possibility of the ML approach application for the LGADs correction was demonstrated. It was shown that using the ML, the necessary correction can be done with a smaller dataset compared to the conventional approach without degrading the time resolution of the detector. Additionally, the ML-based corrections can be implemented on FPGAs and be performed online during the data taking. However, additional development is needed for the upgraded read-out electronics due to changes in the signal structure. The proposed ML-based approach to the correction is planned to be employed for future LGAD applications in the HADES experiment.

Acknowledgement

I want to thank those who supported me over the last four years.

First of all, I want to express my sincere gratitude to my supervisor, Prof. Dr. Tetyana Galatyuk, who gave me an opportunity to work in her group on such an interesting research topic. Her guidance, feedback, and support on both professional and personal levels were invaluable.

I want to thank Prof. Dr. Florian Hug for taking over the second supervision of my research.

I am deeply grateful to Dr. Jerzy Pietraszko. Our discussions on various aspects of my work were constructive and always brought new ideas. I learned a lot from him.

I would like to thank our LGAD team: Wilhelm Krüger, Dr. Adrian Rost, and Dr. Felix Ulrich-Pur. We spent a lot of time together preparing and testing setups in the laboratory as well as during the various beamtimes and it always was fun. Our discussions regarding the latest results were always productive and inspiring. Also, I want to acknowledge them for proofreading my dissertation.

I am thankful for our fun and productive weekly Friday meeting with members of the ViP-QM group: Dr. Szymon Harabash, Florian Seck, Maximilian Wiest, Dr. Adrian Rost, Wilhelm Krüger, Niklas Schild, and Iuliana-Carina Udrea. Thanks to Max, who always keeps us up to date regarding the Nobel laureates as well as the latest news about University life.

I want to thank members of the HADES collaboration. In particular, Dr. Michael Traxler for his support with many aspects of the DAQ system and our lunch group for all the discussions during the lunch and coffee breaks.

I want to mention Willy again. He was unlucky to help me navigate many bureaucratic procedures during my first days. Since then, he supported me in many different ways and I deeply appreciate it.

Last but not least, I thank my parents and my brother for their support.

List of Figures

List of Tables

Bibliography

[1] E. Wilson and B. J. Holzer. "Particle Physics Reference Library : Volume 3: Accelerators and Colliders". In: ed. by Stephen Myers and Herwig Schopper. Cham: Springer International Publishing, 2020. ISBN: 978-3-030-34245-6. DOI: `10.1007/978-3-030-34245-6_1`.

[2] "LHC Design Report Vol.1: The LHC Main Ring". In: (June 2004). Ed. by Oliver S. Bruning et al. DOI: `10.5170/CERN-2004-003-V-1`.

[3] "High-Luminosity Large Hadron Collider (HL-LHC) : Preliminary Design Report". In: (Dec. 2015). Ed. by G Apollinari et al. DOI: `10.5170/CERN-2015-005`.

[4] P Agostini et al. "The Large Hadron–Electron Collider at the HL-LHC". In: *Journal of Physics G: Nuclear and Particle Physics* 48.11 (Nov. 2021), p. 110501. ISSN: 1361-6471. DOI: `10.1088/1361-6471/abf3ba`.

[5] M. Tigner. "A possible apparatus for electron clashing-beam experiments". In: *Nuovo Cim* 37 (1965), pp. 1228–1231. DOI: `10.1007/BF02773204`.

[6] Lia Merminga. "Energy Recovery Linacs". In: *Synchrotron Light Sources and Free-Electron Lasers: Accelerator Physics, Instrumentation and Science Applications*. Ed. by Eberhard J. Jaeschke et al. Cham: Springer International Publishing, 2016, pp. 419–457. ISBN: 978-3-319-14394-1. DOI: `10.1007/978-3-319-14394-1_11`.

[7] J. Pietraszko et al. "Low Gain Avalanche Detectors for the HADES reaction time (T_0) detector upgrade". In: *Eur. Phys. J. A* 56.7 (2020). This work is licensed under the Creative Commons Attribution 4.0 International License. To view a copy of this license, visit `http://creativecommons.org/licenses/by/4.0/.`, p. 183. DOI: `10.1140/epja/s10050-020-00186-w`.

[8] Norbert Pietralla. "The Institute of Nuclear Physics at the TU Darmstadt". In: *Nuclear Physics News* 28.2 (2018), pp. 4–11. DOI: `10.1080/10619127.2018.1463013`.

[9] A. Richter. "Operational experience at the S-DALINAC". In: *Proc. EPAC'96*. 1996.

[10] Yuliya Fritzsche. "Aufbau und Inbetriebnahme einer Quelle polarisierter Elektronen am supraleitenden Darmstädter Elektronenlinearbeschleuniger S-DALINAC". PhD thesis. Darmstadt: Technische Universität Darmstadt, 2011. URL: `http://tuprints.ulb.tu-darmstadt.de/2801/`.

[11] Michaela Arnold et al. "First operation of the superconducting Darmstadt linear electron accelerator as an energy recovery linac". In: *Phys. Rev. Accel. Beams* 23 (2 Feb. 2020), p. 020101. DOI: `10.1103/PhysRevAccelBeams.23.020101`.

[12] Felix Schliessmann et al. "Realization of a multi-turn energy recovery accelerator". In: *Nature Physics* 19 (2023), pp. 597–602. DOI: `10.1038/s41567-022-01856-w`.

[13] Adrian Rost. *S-DALINAC floor plan*. private communication. 2023.

[14] K. Sonnabend et al. "The Darmstadt High-Intensity Photon Setup (DHIPS) at the S-DALINAC". In: *Nuclear Instruments and Methods in Physics Research Section A: Accelerators, Spectrometers, Detectors and Associated Equipment* 640.1 (2011), pp. 6–12. ISSN: 0168-9002. DOI: `https://doi.org/10.1016/j.nima.2011.02.107`.

[15] D. Savran et al. "The low-energy photon tagger NEPTUN". In: *Nuclear Instruments and Methods in Physics Research Section A: Accelerators, Spectrometers, Detectors and Associated Equipment* 613.2 (2010), pp. 232–239. ISSN: 0168-9002. DOI: https://doi.org/10.1016/j.nima.2009.11.038.

[16] D. Schüll et al. "High resolution electron scattering facility at the Darmstadt linear accelerator (DALINAC): III. Detector system and performance of the electron scattering apparatus". In: *Nuclear Instruments and Methods* 153.1 (1978), pp. 29–41. ISSN: 0029-554X. DOI: https://doi.org/10.1016/0029-554X(78)90613-4.

[17] Antonio D'Alessio et al. "The QClam-Spectrometer at the S-DALINAC". In: *Basic Concepts in Nuclear Physics: Theory, Experiments and Applications*. Ed. by José-Enrique García-Ramos et al. Springer International Publishing, 2019, pp. 189–190. ISBN: 978-3-030-22204-8.

[18] Adrian Rost. "Design, installation and commissioning of new read-out electronics for HADES ECAL and diamond detectors for T0-reconstruction and beam diagnostics". PhD thesis. Darmstadt: Technische Universität Darmstadt, 2020. DOI: https://doi.org/10.25534/tuprints-00012235.

[19] Michaela Arnold et al. "Construction of a Third Recirculation for the S-DALINAC*". In: *28th International Linear Accelerator Conference*. 2017, MOPLR014. DOI: 10.18429/JACoW-LINAC2016-MOPLR014.

[20] Michaela Arnold. "Auslegung, Planung und Aufbau einer dritten Rezirkulation mit ERL-Modus für den S-DALINAC". PhD thesis. Darmstadt: Technische Universität, 2017. URL: http://tuprints.ulb.tu-darmstadt.de/6194/.

[21] Michaela Arnold et al. "First ERL Operation of S-DALINAC and Commissioning of a Path Length Adjustment System". In: *9th International Particle Accelerator Conference*. June 2018. DOI: 10.18429/JACoW-IPAC2018-THPML087.

[22] *The Superconducting Darmstadt Electron Accelerator*. 2023. URL: https://www.ikp.tu-darmstadt.de/forschung_kernphysik/experimentelle_geraete/s_dalinac_details/index.en.jsp (visited on 10/24/2023).

[23] Felix Schließmann et al. "Beam Dynamics Simulations for the Twofold ERL Mode at the S-DALINAC*". In: *63rd ICFA Advanced Beam Dynamics Workshop on Energy Recovery Linacs*. 2020, FRCOXBS03. DOI: 10.18429/JACoW-ERL2019-FRCOXBS03.

[24] Manuel Dutine et al. "Concept of a Beam Diagnostics System for the Multi-Turn ERL Operation at the S-DALINAC". In: *JACoW* IPAC2022 (2022), MOPOPT012. DOI: 10.18429/JACoW-IPAC2022-MOPOPT012.

[25] Hermann Kolanoski and Norbert Wermes. *Particle Detectors: Fundamentals and Applications*. Oxford University Press, June 2020. ISBN: 9780198858362. DOI: 10.1093/oso/9780198858362.001.0001.

[26] Karl W. Böer and Udo W. Pohl. *Semiconductor Physics (2nd edition)*. Springer International Publishing, Feb. 2023. ISBN: 978-3-031-18286-0. DOI: 10.1007/978-3-031-18286-0.

[27] Alan Owens. *Semiconductor Radiation Detectors*. New York: CRC Press, 2019. ISBN: 9781315114934. DOI: 10.1201/b22251.

[28] Frank Hartmann. "Basic Principles of a Silicon Detector". In: *Evolution of Silicon Sensor Technology in Particle Physics*. Cham: Springer International Publishing, 2017, pp. 1–133. ISBN: 978-3-319-64436-3. DOI: 10.1007/978-3-319-64436-3_1.

[29] M.J. Berger et al. "Stopping-power and range tables for electrons, protons, and helium ions," in: *NIST Standard Reference Database 124* (2017). DOI: 10.18434/T4NC7P.

[30]   Rene Brun and Fons Rademakers. "ROOT — An object oriented data analysis framework". In: *Nuclear Instruments and Methods in Physics Research Section A: Accelerators, Spectrometers, Detectors and Associated Equipment* 389.1 (1997). New Computing Techniques in Physics Research V, pp. 81–86. ISSN: 0168-9002. DOI: https://doi.org/10.1016/S0168-9002(97)00048-X.

[31]   Hartmut F. -W. Sadrozinski, Abraham Seiden, and Nicolò Cartiglia. *4-Dimensional Tracking with Ultra-Fast Silicon Detectors*. 2017. arXiv: 1704.08666 [physics.ins-det].

[32]   H. F.-W. Sadrozinski et al. "Ultra-fast silicon detectors". In: *Nuclear Instruments and Methods in Physics Research Section A: Accelerators, Spectrometers, Detectors and Associated Equipment* 730 (2013). Proceedings of the 9th International Conference on Radiation Effects on Semiconductor Materials Detectors and Devices, pp. 226–231. ISSN: 0168-9002. DOI: https://doi.org/10.1016/j.nima.2013.06.033.

[33]   M. Ferrero et al. *An Introduction to Ultra-Fast Silicon Detectors (1st ed.)*. This work is licensed under the Creative Commons Attribution-NonCommercial-NoDerivatives 4.0 International License. To view a copy of this license, visit https://creativecommons.org/licenses/by-nc-nd/4.0/. CRC Press, 2021. ISBN: 9781003131946. DOI: 10.1201/9781003131946.

[34]   Claudio Piemonte. "A new Silicon Photomultiplier structure for blue light detection". In: *Nuclear Instruments and Methods in Physics Research Section A: Accelerators, Spectrometers, Detectors and Associated Equipment* 568.1 (2006). New Developments in Radiation Detectors, pp. 224–232. ISSN: 0168-9002. DOI: https://doi.org/10.1016/j.nima.2006.07.018.

[35]   Gabriele Giacomini. "LGAD-Based Silicon Sensors for 4D Detectors". In: *Sensors* 23.4 (2023). ISSN: 1424-8220. DOI: 10.3390/s23042132.

[36]   Stefan Gundacker and Arjan Heering. "The silicon photomultiplier: fundamentals and applications of a modern solid-state photon detector". In: *Physics in Medicine & Biology* 65.17 (Aug. 2020), 17TR01. DOI: 10.1088/1361-6560/ab7b2d.

[37]   V. Sola et al. "Ultra-Fast Silicon Detectors for 4D tracking". In: *Journal of Instrumentation* 12.02 (2017), p. C02072. DOI: 10.1088/1748-0221/12/02/C02072.

[38]   N. Cartiglia et al. "Design optimization of ultra-fast silicon detectors". In: *Nuclear Instruments and Methods in Physics Research Section A: Accelerators, Spectrometers, Detectors and Associated Equipment* 796 (2015). Proceedings of the 10th International Conference on Radiation Effects on Semiconductor Materials Detectors and Devices, pp. 141–148. ISSN: 0168-9002. DOI: https://doi.org/10.1016/j.nima.2015.04.025.

[39]   V. Sola et al. "First FBK production of 50 μm ultra-fast silicon detectors". In: *Nuclear Instruments and Methods in Physics Research Section A: Accelerators, Spectrometers, Detectors and Associated Equipment* 924 (2019). 11th International Hiroshima Symposium on Development and Application of Semiconductor Tracking Detectors, pp. 360–368. ISSN: 0168-9002. DOI: https://doi.org/10.1016/j.nima.2018.07.060.

[40]   Francesca Cenna et al. "Weightfield2: A fast simulator for silicon and diamond solid state detector". In: *Nuclear Instruments and Methods in Physics Research Section A: Accelerators, Spectrometers, Detectors and Associated Equipment* 796 (2015). Proceedings of the 10th International Conference on Radiation Effects on Semiconductor Materials Detectors and Devices, pp. 149–153. ISSN: 0168-9002. DOI: https://doi.org/10.1016/j.nima.2015.04.015.

[41]   M. Mandurrino et al. "Analysis and numerical design of Resistive AC-Coupled Silicon Detectors (RSD) for 4D particle tracking". In: *Nuclear Instruments and Methods in Physics Research Section A: Accelerators, Spectrometers, Detectors and Associated Equipment* 959 (2020), p. 163479. ISSN: 0168-9002. DOI: https://doi.org/10.1016/j.nima.2020.163479.

[42] G. Paternoster et al. "Novel strategies for fine-segmented Low Gain Avalanche Diodes". In: *Nuclear Instruments and Methods in Physics Research Section A: Accelerators, Spectrometers, Detectors and Associated Equipment* 987 (2021), p. 164840. ISSN: 0168-9002. DOI: `https://doi.org/10.1016/j.nima.2020.164840`.

[43] N. Cartiglia et al. "Tracking in 4 dimensions". In: *Nuclear Instruments and Methods in Physics Research Section A: Accelerators, Spectrometers, Detectors and Associated Equipment* 845 (2017). This work is licensed under the Creative Commons Attribution-NonCommercial-NoDerivatives 4.0 International License. To view a copy of this license, visit `https://creativecommons.org/licenses/by-nc-nd/4.0/`, pp. 47–51. ISSN: 0168-9002. DOI: `https://doi.org/10.1016/j.nima.2016.05.078`.

[44] N. Cartiglia et al. "The 4D pixel challenge". In: *Journal of Instrumentation* 11.12 (2016), p. C12016. DOI: `10.1088/1748-0221/11/12/C12016`.

[45] M. Ferrero et al. "Radiation resistant LGAD design". In: *Nuclear Instruments and Methods in Physics Research Section A: Accelerators, Spectrometers, Detectors and Associated Equipment* 919 (2019), pp. 16–26. ISSN: 0168-9002. DOI: `https://doi.org/10.1016/j.nima.2018.11.121`.

[46] Z. Galloway et al. "Properties of HPK UFSD after neutron irradiation up to 6e15 n/cm2". In: *Nuclear Instruments and Methods in Physics Research Section A: Accelerators, Spectrometers, Detectors and Associated Equipment* 940 (2019), pp. 19–29. ISSN: 0168-9002. DOI: `https://doi.org/10.1016/j.nima.2019.05.017`.

[47] S.M. Mazza et al. "Properties of FBK UFSDs after neutron and proton irradiation up to 6☐ 1015 neq/cm2". In: *Journal of Instrumentation* 15.04 (2020), T04008. DOI: `10.1088/1748-0221/15/04/T04008`.

[48] N. Cartiglia et al. "Beam test results of a 16ps timing system based on ultra-fast silicon detectors". In: *Nuclear Instruments and Methods in Physics Research Section A: Accelerators, Spectrometers, Detectors and Associated Equipment* 850 (2017), pp. 83–88. ISSN: 0168-9002. DOI: `https://doi.org/10.1016/j.nima.2017.01.021`.

[49] J. Adamczewski-Musch, H. G. Essel, and S. Linev. "Online Object Monitoring With Go4 V4.4". In: *IEEE Transactions on Nuclear Science* 58.4 (2011), pp. 1477–1481. DOI: `10.1109/TNS.2011.2149541`.

[50] V. Kedych et al. "Low Gain Avalanche Detector Application for Beam Monitoring". In: *Proc. 11th Int. Beam Instrum. Conf. (IBIC'22)*. International Beam Instrumentation Conference. This work is licensed under the Creative Commons Attribution 4.0 International License. To view a copy of this license, visit `http://creativecommons.org/licenses/by/4.0/`. JACoW Publishing, Geneva, Switzerland, Dec. 2022, MOP29. ISBN: 978-3-95450-241-7. DOI: `10.18429/JACoW-IBIC2022-MOP29`.

[51] GSI Helmholtzzentrum für Schwerionenforschung GmbH. *TRB3 web page*. 2023. URL: `https://http://trb.gsi.de/` (visited on 10/30/2023).

[52] A Neiser et al. "TRB3: a 264 channel high precision TDC platform and its applications". In: *Journal of Instrumentation* 8.12 (Dec. 2013), p. C12043. DOI: `10.1088/1748-0221/8/12/C12043`.

[53] Miroslav Morhac. *TSpectrum Class Reference*. URL: `https://root.cern.ch/doc/master/classTSpectrum.html`.

[54] Miroslav Morhac. *Processing and Visualization Functions*. URL: `https://root.cern/root/htmldoc/guides/spectrum/Spectrum.html`.

[55] Felix Ulrich-Pur et al. *First experimental time-of-flight-based proton radiography using low gain avalanche diodes*. 2023. arXiv: `2312.15027` `[physics.med-ph]`.

[56] Felix Ulrich-Pur. *LGAD test setup*. private communication. Mar. 2023.

[57] Yevhen Kozymka. "LGAD performance optimization for the time measurements". In preparation. Master's thesis. Technische Universität Darmstadt, 2024.

[58] Wilhelm Krüger. "Low Gain Avalanche Detectors for Timing Applications in HADES". Master's thesis. Technische Universität Darmstadt, Dec. 2020.

[59] J. Allison et al. "Geant4 developments and applications". In: *IEEE Transactions on Nuclear Science* 53.1 (2006), pp. 270–278. DOI: 10.1109/TNS.2006.869826.

[60] J. Allison et al. "Recent developments in Geant4". In: *Nuclear Instruments and Methods in Physics Research Section A: Accelerators, Spectrometers, Detectors and Associated Equipment* 835 (2016), pp. 186–225. ISSN: 0168-9002. DOI: https://doi.org/10.1016/j.nima.2016.06.125.

[61] S. Agostinelli et al. "Geant4—a simulation toolkit". In: *Nuclear Instruments and Methods in Physics Research Section A: Accelerators, Spectrometers, Detectors and Associated Equipment* 506.3 (2003), pp. 250–303. ISSN: 0168-9002. DOI: https://doi.org/10.1016/S0168-9002(03)01368-8.

[62] Adrian Barbu and Song-Chun Zhu. *Monte Carlo Methods*. Singapore: Springer Singapore, 2020. ISBN: 978-981-13-2971-5. DOI: 10.1007/978-981-13-2971-5.

[63] Adrian Rost and Manuel Dutine. *The S-DALINAC recirculation line*. private communication. June 2023.

[64] Geant4 Collaboration. *Guide For Physics Lists*. https://geant4-userdoc.web.cern.ch/UsersGuides/PhysicsListGuide/html/index.html. 2023.

[65] Manuel Dutine. *The wire scanner measurements at the S-DALINAC in ERL mode*. private communication. Nov. 2023.

[66] Francisco A. Rodrigues. "Machine learning in physics: A short guide". In: *Europhysics Letters* 144.2 (Nov. 2023), p. 22001. DOI: 10.1209/0295-5075/ad0575.

[67] G. Agakichiev et al. "The high-acceptance dielectron spectrometer HADES". In: *The European Physical Journal A* 41 (2009), pp. 243–277. DOI: 10.1140/epja/i2009-10807-5.

[68] F. Anghinolfi et al. "NINO: an ultra-fast and low-power front-end amplifier/discriminator ASIC designed for the multigap resistive plate chamber". In: *Nuclear Instruments and Methods in Physics Research Section A: Accelerators, Spectrometers, Detectors and Associated Equipment* 533.1 (2004). Proceedings of the Seventh International Workshop on Resistive Plate Chambers and Related Detectors, pp. 183–187. ISSN: 0168-9002. DOI: https://doi.org/10.1016/j.nima.2004.07.024. URL: https://www.sciencedirect.com/science/article/pii/S0168900204014299.

[69] Gopinath Rebala, Ajay Ravi, and Sanjay Churiwala. *An Introduction to Machine Learning*. Cham: Springer International Publishing, 2019. ISBN: 978-3-030-15729-6. DOI: 10.1007/978-3-030-15729-6.

[70] Abdulhamit Subasi. "Chapter 3 - Machine learning techniques". In: *Practical Machine Learning for Data Analysis Using Python*. Ed. by Abdulhamit Subasi. Academic Press, 2020, pp. 91–202. ISBN: 978-0-12-821379-7. DOI: https://doi.org/10.1016/B978-0-12-821379-7.00003-5.

[71] Matthias Feurer and Frank Hutter. "Hyperparameter Optimization". In: *Automated Machine Learning: Methods, Systems, Challenges*. Ed. by Frank Hutter, Lars Kotthoff, and Joaquin Vanschoren. Cham: Springer International Publishing, 2019, pp. 3–33. ISBN: 978-3-030-05318-5. DOI: 10.1007/978-3-030-05318-5_1.

[72] Joaquin Vanschoren. "Meta-Learning". In: *Automated Machine Learning: Methods, Systems, Challenges*. Ed. by Frank Hutter, Lars Kotthoff, and Joaquin Vanschoren. Cham: Springer International Publishing, 2019, pp. 35–61. ISBN: 978-3-030-05318-5. DOI: 10.1007/978-3-030-05318-5_2.

[73] Matthias Feurer et al. "Auto-sklearn: Efficient and Robust Automated Machine Learning". In: *Automated Machine Learning: Methods, Systems, Challenges*. Ed. by Frank Hutter, Lars Kotthoff, and Joaquin Vanschoren. This work is licensed under the Creative Commons Attribution 4.0 International License. To view a copy of this license, visit `http://creativecommons.org/licenses/by/4.0/`. Cham: Springer International Publishing, 2019, pp. 113–134. ISBN: 978-3-030-05318-5. DOI: `10.1007/978-3-030-05318-5_6`.

[74] H. Osipyan, B.I. Edwards, and A.D. Cheok. *Deep Neural Network Applications*. CRC Press, 2022. DOI: `10.1201/9780429265686`.

[75] Matthias Feurer et al. "Auto-Sklearn 2.0: Hands-free AutoML via Meta-Learning". In: *arXiv:2007.04074 [cs.LG]* (2020).

[76] Haifeng Jin et al. "AutoKeras: An AutoML Library for Deep Learning". In: *Journal of Machine Learning Research* 24.6 (2023), pp. 1–6. URL: `http://jmlr.org/papers/v24/20-1355.html`.

[77] Martín Abadi et al. *TensorFlow: Large-Scale Machine Learning on Heterogeneous Systems*. Software available from tensorflow.org. 2015. URL: `https://www.tensorflow.org/`.

[78] François Chollet et al. *Keras*. `https://keras.io`. 2015.

[79] Fjodor van Veen. *The Neural Network Zoo*. Dec. 2023. URL: `https://www.asimovinstitute.org/neural-network-zoo/`.

[80] Ovidiu Calin. *Deep Learning Architectures: A Mathematical Approach*. Cham: Springer International Publishing, 2020. ISBN: 978-3-030-36721-3. DOI: `10.1007/978-3-030-36721-3`.

[81] *TensorFlow documentation: Normalization*. URL: `https://www.tensorflow.org/api_docs/python/tf/keras/layers/Normalization`.

Curriculum Vitae

Personal information

Name	Vadym Kedych
Date of birth	26 June 1995
Place of birth	Kuznetsovsk, Ukraine

Education

Since 02/2020	PhD in Physics, Technische Universität Darmstadt
09/2016 - 06/2018	Master of Science in Physics, Taras Shevchenko National University of Kyiv, Ukraine
09/2012 - 06/2016	Bachelor of Science in Physics, Taras Shevchenko National University of Kyiv, Ukraine

Other experience

08/2018 - 12/2019	Front-end developer

List of publications

V. Kedych et al., "Low Gain Avalanche Detector Application for Beam Monitoring", in Proc. IBIC'22, Kraków, Poland, Sep. 2022, pp. 109-112.doi:10.18429/JACoW-IBIC2022-MOP29.

J. Pietraszko, T. Galatyuk, **V. Kedych** et al. "Low Gain Avalanche Detectors for the HADES reaction time (T0) detector upgrade". Eur. Phys. J. A 56, 183 (2020). https://doi.org/10.1140/epja/s10050-020-00186-w.

F. Ulrich-Pur, **V. Kedych** et al. "First Experimental Time-of-flight-based Proton Radiography Using Low Gain Avalanche Diodes." ArXiv, 2023, /abs/2312.15027.

W. Krüger, **V. Kedych** et al. "LGAD Technology for HADES, Accelerator and Medical Applications." Nuclear Instruments and Methods in Physics Research Section A: Accelerators, Spectrometers, Detectors and Associated Equipment, vol. 1039, 2022, p. 167046, https://doi.org/10.1016/j.nima.2022.167046.

A. Rost, **V. Kedych** et al., "Status of Diamond and LGAD Based Beam-Detectors for the mCBM and CBM Experiments at GSI and FAIR", in Proc. IPAC'22, Bangkok, Thailand, Jun. 2022, pp. 247-250. doi:10.18429/JACoW-IPAC2022-MOPOPT010.